EXTRACELLULAR MATRIX SECRETED BY OSTEOGENICALLY ENHANCED MESENCHYMAL STEM CELLS RECAPITULATES THE OSTEOGENIC MICROENVIRONMENT

A Dissertation

by

EOIN MC NEILL

Submitted to the Office of Graduate and Professional Studies of
Texas A&M University
in partial fulfillment of the requirements for the degree of

DOCTOR OF PHILOSOPHY

Chair of Committee,	Carl Gregory
Committee Members,	Fei Liu
	Roland Kaunas
	Brian Saunders
Head of Program,	Carol Vargas

December 2019

Major Subject: Medical Sciences

ABSTRACT

Extracellular matrix (ECM) is a primary component of the osteogenic microenvironment, providing support for attachment, proliferation, and differentiation to facilitate bone growth and maintenance. Previously we have shown that ECM secreted by osteogenically enhanced mesenchymal stem cells (OEhMSCs) resembles an anabolic bone microenvironment and promotes bone healing by OEhMSCs *in vivo*.

OEhMSCs are usually obtained from bone marrow, a finite source, and are subject to reduced efficacy with extensive expansion in culture. This limits their widespread clinical use. This issue can be overcome by using induced pluripotent stem cells (iPSCs) as a source of MSCs (ihMSCs). The ihMSCs are highly osteogenic and can be osteogenically enhanced (OEihMSCs) by upregulating canonical Wnt signaling. OEihMSCs secrete a dense ECM rich in collagens VI and XII. When implanted into a murine calvarial defect this ECM promotes significant levels of bone healing, with 4-6 times more bone generated than bone morphogenetic protein 2 (BMP-2). Furthermore, unlike ECM from OEhMSCs, OEihMSC-derived ECM possesses intrinsic osteogenic activity, not requiring co-administration with exogenous osteoprogenitors to promote bone healing.

Malignant bone disease (MBD) is characterized by the formation of osteolytic lesions, which promote tumor relapse and resistance to chemotherapy. Standard tissue culture techniques to study MBD do not accurately represent the bone microenvironment and the complex bone-tumor interactions therein. These interactions can be studied more

accurately by co-culturing osteoprogenitors with osteosarcoma (OS) cells on OEhMSC-derived ECM-coated microcarriers in a 3D culture system that better recapitulates the topological and biochemical characteristics of bone tissue. This platform captured biochemical markers indicative of osteoinhibition via Dkk-1 secretion from the OS cells and unlike monolayer culture, migration of osteoprogenitors and OS cells was readily visualized. On OEhMSC-derived ECM, OS cells proliferated rapidly, displacing the osteoprogenitors, ultimately leading to their death, providing an experimentally accessible system to simultaneously examine how the osteogenic microenvironment can drive OS cell migration, engraftment, proliferation, bone destruction and ultimately disease progression.

Recapitulation of the osteogenic microenvironment is appealing both as a therapeutic to promote bone healing, and as a substrate to study interactions within bone. This study presents a novel osteoinductive scaffold with profound ability to promote bone healing, that is obtained from a theoretically infinite pluripotent cell source. Furthermore, a system involving co-culture of osteoprogenitors and OS cells on ECM-coated microcarriers in a 3D culture system has the capacity to provide new and quantifiable insights in the multiple pathological mechanisms of MBD, that are not readily measurable with current techniques.

ACKNOWLEDGEMENTS

I would like to thank Dr. Carl Gregory for his continued support and guidance during my time in his lab. I would also like to thank my committee members Dr. Fei Liu, Dr. Roland Kaunas, and Dr. Brian Saunders for their time and guidance. I would also like to thank Dr. Christopher Chaput for his guidance during my graduate studies.

I would like to thank all of the current and past members of the Texas A&M Health Science Center Institute for Regenerative Medicine, in particular Suzanne Zeitouni, Bret Clough, Ulf Krause, Simin Pan, and Andrew Haskell.

Finally, I would like to thank my parents and girlfriend Kaitlynn for supporting me throughout this journey.

CONTRIBUTORS AND FUNDING SOURCES

Contributors

This work was supervised by a dissertation committee chaired by Associate Professor Carl Gregory of the Department of Molecular and Cellular Medicine, consisting of Associate Professor Fei Liu of the Department of Molecular and Cellular Medicine, Associate Professor Roland Kaunas of the Department of Biomedical Engineering and Associate Professor Brian Saunders of the Department of Small Animal Clinical Sciences.

The mass spectrometry in Chapter II was performed by Dr. Doyong Kim at the Texas A&M University Center for Mass Spectrometry. The SEM from Chapter II was performed by Tom Stephens at the Texas A&M University Microscopy and Imaging Center. The proteomic analysis in Chapter II and the heatmaps of qRT-PCR data in Chapters II and III were processed by Simin Pan in the Department of Molecular and Cellular Medicine. The generation of ECM-coated microcarriers for Chapter III was performed by Abishek Tondon and Robert Reese in the Department of Biomedical Engineering.

Funding Sources

This work was made possible in part by grants from the National Institutes of Health (R01AR066033-01) and the Center for the Advancement of Science in Space (CASIS, RFP2013-2) awarded to CAG and RK, and three intramural grants awarded by

Texas A&M University. Its contents are solely the responsibility of the authors and do not necessarily represent the official views of the awarding entities.

NOMENCLATURE

ADM	Adipogenic differentiation medium
ALP	Alkaline phosphatase
ARS	Alizarin Red S
BM	Bone marrow
BMP-2	Bone morphogenetic protein 2
CCM	Complete culture medium
CDM	Chondrogenic differentiation medium
cWnt	Canonical wingless/Int
Dkk-1	Dickkopf-1
DMSO	Dimethyl sulfoxide
ECM	Extracellular matrix
EDTA	Ethylenediaminetetraacetic acid
ihMSC	Human induced pluripotent stem cell-derived mesenchymal stem cell
GFP	Green fluorescent protein
iPSC	Induced pluripotent stem cell
MBD	Malignant bone disease
MSC	Mesenchymal stem cell
OBM	Osteogenic base medium
OE	Osteogenically enhanced

OL	Osteolytic lesion
OPG	Osteoprotegerin
OS	Osteosarcoma
RANK	Receptor activator of nuclear kappa-B
RFP	Red fluorescent protein
RWV	Rotating wall vessel
PPARγ	Peroxisome proliferator-activated receptor gamma
TNFα	Tumor necrosis factor alpha

TABLE OF CONTENTS

Page

LIST OF FIGURES

Page

LIST OF TABLES

Page

CHAPTER I

INTRODUCTION

The extracellular matrix (ECM) is a dynamic and complex network of proteins and polysaccharides secreted by cells to provide a supportive microenvironment. By providing biochemical and mechanical cues, the ECM regulates a number of essential cellular processes such as adhesion, proliferation, and differentiation [1,2]. ECM composition is unique to each tissue to provide appropriate support for cellular function [3]. ECM assembly is a highly organized process with even minor variations resulting in altered cell-matrix interactions [1].

The importance of the ECM is highlighted by the role dysfunctional ECM plays in a wide variety of diseases, such as osteogenesis imperfect (OI) and osteoporosis. Dysfunctional ECM can be hereditary or caused by environmental factors. In OI, mutations resulting in impaired collagen I synthesis have been identified [4]. Point mutations that affect glycine residues in COL1A1 or COL1A2 prevent correct assembly of the triple-helical structure, resulting in abnormal collagen I production [5]. Osteoblasts with collagen I mutations produce an ECM with altered expression of fibronectin, thrombospondin and hyaluronan [6]. Precise collagen I arrangement in the ECM is required to provide toughness to bone and regulate the formation of calcium apatite crystals, with abnormally large crystals observed in OI patients [7]. As such, abnormal ECM is responsible for the brittleness and susceptibility to fracture characteristic of OI bone [4].

Collagen I is the main component of ECM and is therefore implicated in multiple diseases. In glucocorticoid-induced osteoporosis, reduced collagen I production has been reported [8,9]. In the presence of glucocorticoids, mesenchymal stem cells (MSCs), the precursors for osteoblasts, are directed toward an adipogenic lineage, resulting in reduced and impaired osteoblast differentiation and secretion of a collagen I deficient ECM [10]. Canonical Wnt (cWnt) signaling is essential for osteogenesis by MSCs. Dickkopf-1 (Dkk-1), a potent inhibitor of cWnt signaling, is induced by glucocorticoids. Inhibition of cWnt signaling results in increased peroxisome proliferator-activated receptor gamma (PPARγ) signaling which promotes adipogenesis [11]. This reduction in osteoblast activity results in reduced and abnormal ECM production, and a loss of bone mass leading to increased susceptibility of fracture [12].

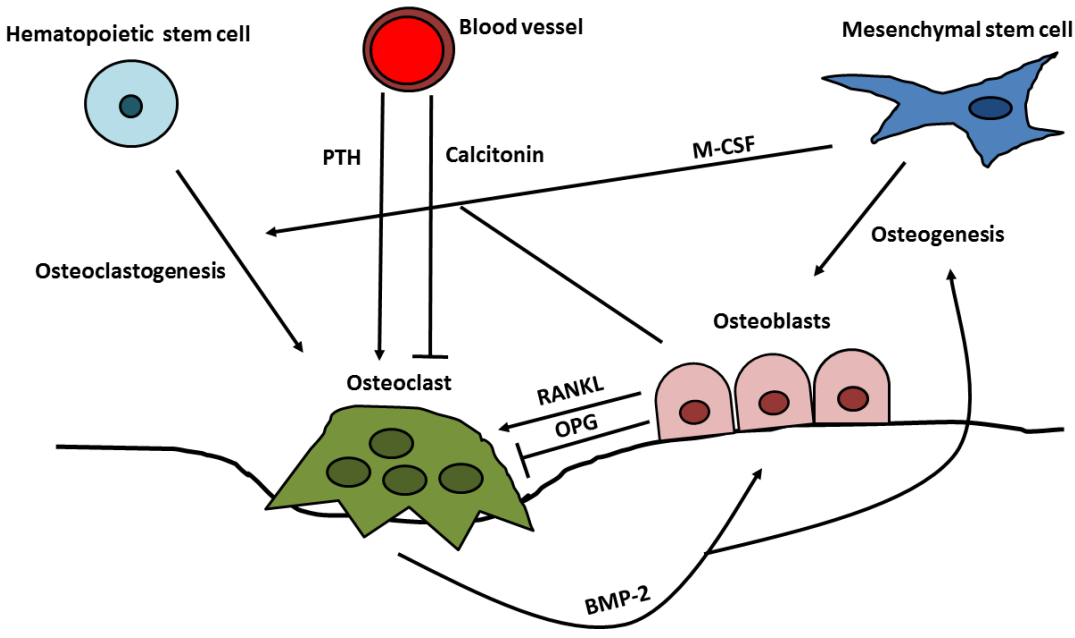

Figure 1: Schematic depicting bone remodeling and the maintenance of bone homeostasis.

Bone remodeling (**Fig1**) occurs constantly throughout life to maintain healthy, functional bone tissue [13]. It is a highly regulated process that requires homeostasis between bone production, by osteoblasts, and bone resorption, by osteoclasts. Remodeling can be divided into three distinct stages. It begins with the recruitment of osteoclast progenitors and differentiation into mature osteoclasts, followed by bone resorption [13]. Osteoclasts are derived from hematopoietic stem cells (HSCs). Osteoblasts and MSCs secrete macrophage colony-stimulating factor (M-CSF) which induces macrophage differentiation and proliferation at the site of remodeling [14]. Osteoblasts also express receptor activator of nuclear factor kappa-B ligand (RANKL), which binds to receptor activator of nuclear factor kappa-B (RANK) on the surface of these M-CSF induced macrophages to promote osteoclast differentiation [15]. Sustained RANK activation causes the osteoclasts to fuse into larger multinucleated cells that sit on the surface of bone and release enzymes such as tartrate-resistant acid phosphatase (TRAP) [15,16] and Cathepsin K that digest the bone matrix [17]. The digestion of the bone matrix causes the release of proteins such as bone morphogenetic protein-2 (BMP-2) which provides an osteogenic stimulus to the osteoblasts [18]. This marks the beginning of the next stage in bone remodeling, the reversal of osteoclast activation and recruitment of osteoblasts [13]. This osteogenic stimulus increases secretion of osteoprotegerin (OPG) by osteoblasts and their precursors. OPG binds to RANKL, preventing it from binding to RANK and therefore antagonizing RANKL-mediated induction of osteoclast activity [15]. Resorption of the bone also causes calcium to be released resulting in a spike in serum calcium concentration. This stimulates the release of calcitonin from the thyroid gland

which binds to a calcitonin receptor on the surface of osteoclasts, further inhibiting their activity [17]. The process of bone remodeling can in turn by induced by low serum calcium concentration and the release of parathyroid hormone (PTH) from the parathyroid gland. PTH increases RANKL expression on osteoblasts and decreases OPG secretion, beginning the process of osteoclast activation in the first stage of remodeling [19,20]. The final stage involves bone formation by osteoblasts [13]. The release of osteogenic factors from the resorbed bone stimulates osteogenesis by MSCs and the maturation of osteoblasts. BMP-2 can positively regulate the cWnt signaling pathway (**Fig3**) resulting in the activation of Runt-related transcription factor 2 (Runx2), the master regulator of osteogenesis, and its' downstream targets [18]. This causes osteoblasts recruited to the surface of the resorption pit to deposit ECM followed by mineralization [17].

As ECM is essential for bone formation and maintenance [21], many musculoskeletal engineering approaches aim to mimic its' activity to develop novel osteoinductive materials. Synthetic materials aim to recreate the mechanical stimuli provided by ECM [22,23] while collagen-coated scaffolds aim to mimic biochemical cues [24]. However, these approaches do not accurately recapitulate the complex osteogenic microenvironment provided by ECM. As osteoblasts are responsible for ECM deposition and mineralization in bone, their progenitors, MSCs have emerged at the forefront of the field of musculoskeletal engineering. MSCs possess multipotent differentiation potential (**Fig2**), capable of differentiation into osteoblasts, chondrocytes, and adipocytes [25], and potent immunomodulatory abilities [26,27]. MSCs exert their immunomodulatory effects via the secretion of soluble factors and exosomes that can inhibit both the innate and

adaptive immune response. This has led to the use of MSCs in numerous clinical trials for inflammatory and autoimmune disorders [26,28]. MSCs were first identified as a subpopulation of osteogenic bone marrow cells distinguishable from hematopoietic cells by their adherence to tissue culture surfaces and their fibroblast-like morphology by Friedenstein *et al* [29,30]. Originally known as colony forming unit-fibroblasts (CFU-Fs), MSCs displayed the ability to replicate *in vitro*, support hematopoietic stroma and differentiate into osteogenic, chondrogenic, and adipogenic tissue *in vivo* [30-32].

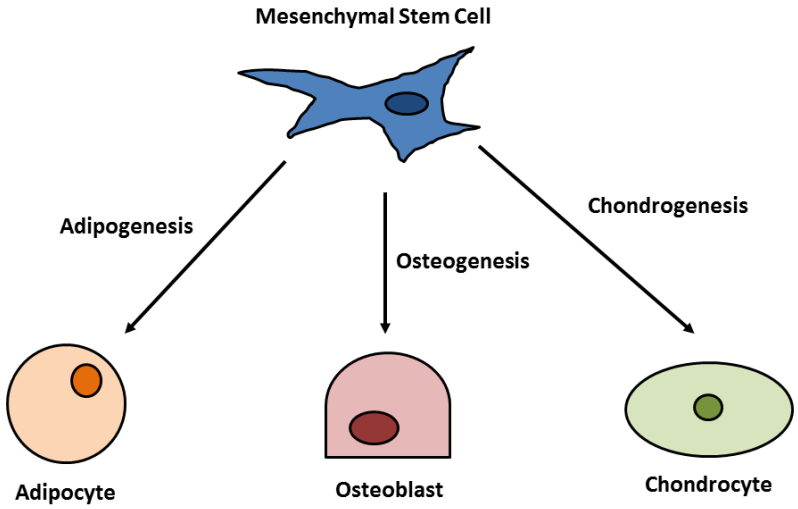

Figure 2: Multipotent potential of mesenchymal stem cells.

The term "Mesenchymal Stem Cell" was not used until 1991 when it was coined by Arnold Caplan [33]. At this time the ability of MSCs to differentiate into osteoblasts and chondrocytes had been well established and their potential use as a cell-based therapy to regenerate bone was proposed [33]. At the time, direct differentiation and contribution of transplanted MSCs to repaired tissue was believed to be responsible for their therapeutic effects, however, advances in the field have identified the role of trophic mediators [34].

ECM secreted by MSCs could be considered a trophic mediator as it is a secretory product and not a direct product of terminally differentiated MSCs.

Previously we have shown that human bone marrow-derived MSCs (hMSCs) can be osteogenically enhanced to increase their efficacy for bone repair [35]. Osteogenic enhancement is achieved by attenuating the inhibitory crosstalk from the PPARγ pathway on the cWnt pathway (**Fig3**) with PPARγ antagonist, 2-chloro-5-nitrobenzanilide, GW9962. The cWnt pathway drives osteogenesis in hMSCs [35].

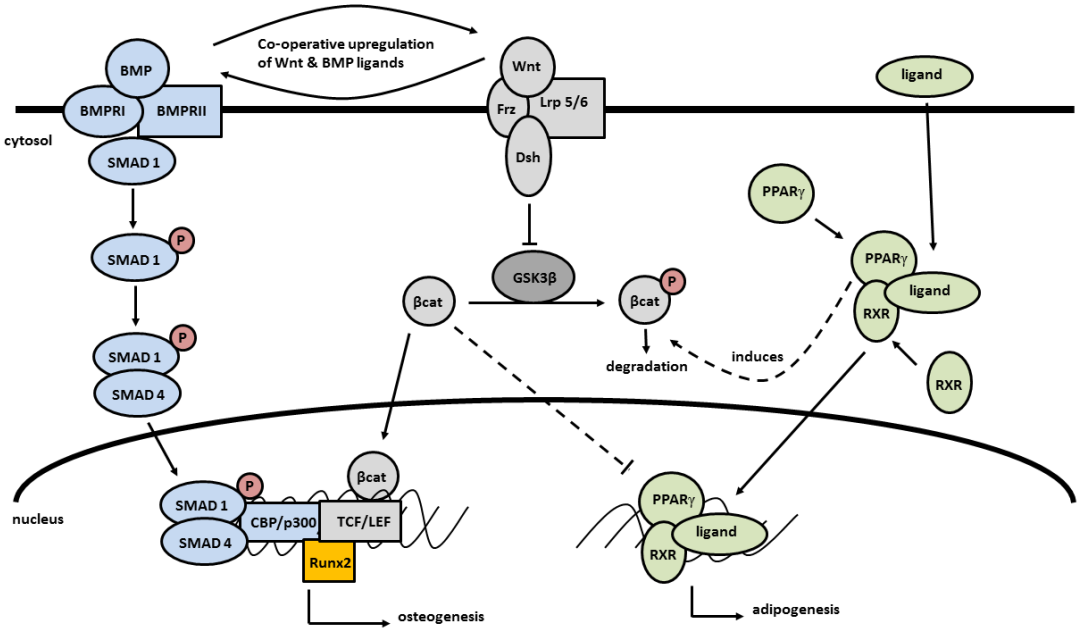

Figure 3: Schematic showing the interactions between SMAD, cWnt, and PPARγ signaling pathways.

In the absence of Wnt signaling, cytosolic β-catenin (β-cat) is degraded by a destruction complex consisting of glycogen synthase 3 beta (GSK3β), Axin, adenomatosis polyposis coli (APC), protein phosphatase 2A (PP2A), and casein kinase 1α (CK1α) [36]. CK1α phosphorylates β-cat and GSK3β marks it for ubiquitination, resulting in proteolytic

destruction [37]. Activated PPARγ signaling promotes β-cat degradation in this manner by upregulating GSK3β activity [38]. When Wnt is present it binds to a complex of frizzled (FZD) and low-density lipoprotein receptor-related protein 5/6 (LRP5/6) [39]. This complex activates disheveled (Dsh) and causes the destruction complex to translocate to the membrane where axin binds to LRP5/6 and Dsh. Dsh inhibits the activity of GSK3β by recruiting a GSK3β-binding protein (GBP) to the complex [40]. Inhibition of the destruction complex allows cytosolic β-cat to stabilize and translocate to the nucleus where it activates genes such as Runx2 by activating T cell factor (TCF)/lymphoid enhancing factor (LEF)-mediated transcription [41].

Osteogenically enhanced hMSCs (OEhMSCs) were found to secrete an ECM enriched with factors present in anabolic bone. This ECM significantly enhanced the capacity of both OEhMSCs and human bone marrow (hBM) to promote bone repair *in vivo* [42-44]. The ECM provided retention signals to the cells, prolonging their detection at the defect site, along with inducing the secretion of angiogenic and osteogenic factors, such as bone morphogenetic protein 2 (BMP-2) [42,44]. Collagens VI and XII were identified as partially responsible for this mechanism [42].

Recapitulating the osteogenic microenvironment is a desirable prospect for musculoskeletal engineering. An autologous bone graft remains the most efficacious therapy for bone repair despite the emergence of numerous alternatives [45]. This suggests that mimicry of anabolic bone is vital to developing future bone repair therapies. OEhMSC-ECM has demonstrated comparable efficacy to bone grafts as an osteoinductive scaffold *in vivo* [43]. However, hMSC preparations are heterogeneous,

obtained from a finite source, and exhibit reduced efficacy as they are expanded to clinically relevant numbers *in vitro* [46]. These features present obstacles to developing a hMSC-based therapy, as efficacy and reproducibility are difficult to define among multiple preparations.

OEhMSC- ECM could also provide a substrate to study the complex cell-cell and cell-matrix interactions within the osteogenic microenvironment. While adherent cells will readily propagate on tissue culture plastic, it does not offer the biochemical and mechanical support provided by ECM. Altered morphology, proliferation and function have been observed in response to tissue culture plastic [47,48]. The study of malignant bone disease (MBD) is an area that could benefit from OEhMSC-ECM. MBD causes significant damage to bone, by disrupting homeostasis to favor bone destruction [49]. It is characterized by the presence of osteolytic lesions (OLs), which cause pain, susceptibility to fracture, and resistance of the tumor cells to chemotherapy[50]. Mimicking the osteogenic microenvironment with OEhMSC-derived ECM could provide greater understanding of OL formation and MBD progression which is vital to create therapeutic strategies to address MBD.

CHAPTER II

A PLURIPOTENT STEM CELL-DERIVED MATRIX WITH PROFOUND OSTEOREGENERATIVE CAPABILITIES

Introduction

Approximately 6 million fractures occur in the United States each year with about 10% experiencing delayed or incomplete healing [51]. The cost of treating these fractures is estimated to be around $200 billion which places a significant burden on both patients and the healthcare system. This figure rises to over $450 billion annually when the costs of spinal fusion surgeries are included [52]. Of the 650,000 spinal fusion surgeries performed in the United States annually, 15%-40% will fail [43,53,54]. These figures are steadily increasing due to an aging population, low quality diets, and increased tobacco, alcohol and drug use resulting in an increased prevalence of diseases such as cancer, obesity, and diabetes. All of which have been implicated in reduced capacity to repair bone [52,55,56].

There are a number of therapies to promote bone repair available however each comes with significant caveats. An autologous bone graft is the current gold standard. This procedure requires bone to be explanted from a distal site, commonly the iliac crest, and implanted into the site of injury. While efficacious, this approach comes with significant disadvantages, such as limited source material, high cost, the need for two surgical procedures which increases the risk of infection, and donor site morbidity which can include pain, hematoma, and a susceptibility to further fractures [57]. The possibility of

these complications arising increases with age, which affects many autologous bone graft patients [45]. Alternative approaches aim to avoid donor site morbidity by using growth factors, cadaveric bone or synthetic materials. BMP-2 is highly efficacious but has significant safety concerns. Seroma formation, ectopic bone growth, and a potentially life threatening inflammatory response have been reported [58,59]. Cadaveric bone grafts have low osteoinductive properties and carry a high risk of infection [60,61]. Recently cadaveric bone grafts with preserved donor MSCs have become available. However, this option is poorly defined and has not undergone clinical trials for efficacy or safety. With no evidence to suggest that the MSCs are viable in a clinical setting, these cellularized bone grafts may present no advantage over traditional cadaveric bone grafts [62]. Synthetic bone graft materials are abundantly available but have poor osteoinductive properties [63]. Any therapeutic approach would need to demonstrate safety, efficacy and manufacturability to replace autologous bone graft as a gold standard for bone repair.

Bone marrow-derived human mesenchymal stem cells (BM-hMSCs) have been identified as a promising source for this alternative therapy due to their potent osteoinductive and immunomodulatory properties [64,65]. BM-hMSCs have undergone clinical trials for a wide variety of conditions which have repeatedly demonstrated that they are well tolerated with no serious adverse effects reported [66]. However, donor variability and limited availability present roadblocks to developing a new therapy [46]. While hMSCs are commonly harvested from finite sources such as bone marrow or adipose tissue, the development of induced pluripotent stem cells (iPSCs) provides a

promising alternative source [67]. Generating hMSCs from iPSCs (ihMSCs) has the potential to overcome both donor variability and the limited large scale availability of conventional hMSCs by providing a theoretically infinite supply of genetically identical source material [68].

It has previously been demonstrated that BM-hMSCs can be osteogenically enhanced by inhibiting PPARγ signaling with GW9662, a PPARγ antagonist. Removing the inhibitory crosstalk from the PPARγ axis causes increased cWnt signaling resulting in a more osteogenic hMSC capable of enhanced bone healing [35]. Furthermore, ECM secreted by these OEhMSCs promoted superior bone healing by providing an osteogenic microenvironment to support cell attachment, proliferation, and the release of trophic factors [42-44]. The ECM is comprised of factors present in the anabolic bone such as collagens VI and XII, which promote the release of osteogenic and angiogenic factors by osteoprogenitors [42,44]. Both collagens VI and XII are located at bone forming sites and are essential for normal osteoblast function. Collagen VI deficiency results in altered osteoblast morphology [69] while collagen XII deficiency altered osteoblast organization, polarization, and cell-cell interactions [70]. These alterations resulted in reduced bone formation. Recently it was shown that collagens VI and XII form a complex during osteogenesis that mediates cell-cell interactions between osteoblasts suggesting that both are required for optimal osteoblast activity and bone formation [71].

It was hypothesized that ihMSCs could also be osteogenically enhanced and generate an osteogenic ECM to provide a safe, efficacious alternative therapy for bone repair. A therapy consisting of osteogenically enhanced ihMSCs (OEihMSCs) and their

secreted ECM would have reproducible characteristics, without donor variability that limits scalability of OEhMSCs and their secreted ECM. The results demonstrate that ihMSCs are inherently more osteogenic than BM-hMSCs. OEihMSCs generated by exposure to GW9662 secreted significant amounts of ECM, rich in collagens VI and XII, with profound osteoinductive capabilities. When implanted into a murine calvarial defect, OEihMSC-ECM promoted remarkable levels of bone healing independent of the co-administration of osteoprogenitor cells.

Materials and Methods

Tissue culture

BM-hMSCs were obtained from the Texas A&M Health Science Center Institute for Regenerative Medicine Mesenchymal Stem Cell distribution facility in accordance with institutionally approved protocols. The ihMSCs were obtained from Dr. Fei Liu at the Texas A&M Health Science Center Institute for Regenerative Medicine and were generated using a modified protocol as previously described [72]. Frozen vials of $1x10^6$ passage 1 hMSCs were thawed, seeded at 100 cells per cm^2 (BM-hMSCs) or 500 cells per cm^2 (ihMSCs) on $148cm^2$ tissue culture dishes (Corning, Corning, NY) in complete culture medium (CCM). For functional assays, BM-hMSCs and ihMSCs were both seeded at 100 cells per cm^2. CCM is comprised of 10% (For ihMSCs) or 20% (For BM-hMSCs) (v/v) fetal bovine serum (FBS, Atlanta Biologicals, Norcross, GA), 2mM L-glutamine (Life Technologies, Carlsbad, CA) and 100 U/mL penicillin and 100µg/mL streptomycin (Life Technologies, Carlsbad, CA) in minimal essential medium-alpha modified (αMEM, Life Technologies, Carlsbad, CA). The cells were incubated for 2 days at 37ºC with 5% CO_2, washed with phosphate buffered saline (PBS, Life Technologies, Carlsbad, CA) then lifted with 0.25% (w/v) trypsin-ethylenediaminetetraacetic acid (EDTA, 380 mg/l, Life Technologies, Carlsbad, CA) at 37ºC for 4-5 minutes. Microscopy was used to confirm the dissociation of the cells from the tissue culture plastic. Gentle agitation was used if the cells had not dissociated. The trypsin was deactivated with an equal volume of CCM. The cells were centrifuged at 500 x g for 5 minutes and resuspended in CCM. The cells were then counted using a

hemocytometer and seeded at 100 cells per cm^2 in CCM with the media replaced every 2 days. Once the cells reached ~70-80% confluence or about 13,000 cells per cm^2 they were cryopreserved at $1x10^6$ per vial to generate a bank of passage 2 cells to be used in future experiments. The cells were cryopreserved in αMEM containing 50% (v/v) FBS and 5% (v/v) dimethyl sulfoxide (DMSO, Sigma, St. Louis, MO). Assays were performed with cells up to passage 4 unless otherwise stated with passage defined as 6-8 population doublings at sub-confluence. BM-hMSC1 was chosen to represent a highly osteogenic donor and BM-hMSC2 was chosen to represent a modest osteogenic donor based on previous performance in osteogenic assays such as mineralization assays, alkaline phosphatase (ALP) kinetic assay, and OPG secretion. Microscopy was performed with an inverted microscope (Nikon, Eclipse TE200) fitted with a digital camera (Nikon DXM1200F).

Flow cytometry

The ihMSCs were seeded in $148cm^2$ plates (Corning) and cultured in CCM until reaching 70-80% confluence. The cells were recovered with trypsin-EDTA and resuspended in 2% (v/v) FBS in PBS. The ihMSCs were then incubated with specific fluorophore-tagged antibodies or isotype controls (Becton Dickinson, Franklin Lakes, NJ or Beckman Coulter) for 30 minutes on ice in the dark. Antibodies against CD11b (clone BEAR1), CD14 (RMO52), CD19 (J3-119), CD34 (581), CD45 (J.33), CD73 (AD2), CD79a (HM47), CD90 (Thy-1/310), CD105 (IG2), and HLA-DP, DQ, DR (Tu39) were used. The cells were analyzed using a Cytomics FC500 flow cytometer (Beckman Coulter). The data was processed using the manufacturer's software (CXP).

Macrophage co-culture

Green fluorescent protein (GFP)-labeled RAW 264.7 murine macrophage-like cells (American Type Tissue Culture Collection) were cultured in CCM until reaching ~60% confluence. Zero, 50,000 or 500,000 ihMSCs were added to the RAW cells and incubated together in CCM at 37ºC and 5% CO_2 for 18 hours. The RAW cells were stimulated with 0.5µg/mL lipopolysaccharide (LPS, Sigma, St.Louis, MO) and the co-cultures were incubated for a further 18 hours. The media was recovered and stored at -20ºC for enzyme-linked immunosorbent assays (ELISA). The ihMSCs and RAW cells were recovered with trypsin-EDTA and transferred to a black opaque 96 well plate (Corning, Corning, NY). Fluorescence was read at 485/520nm excitation/emission using a FluoStar plate reader (BMG Biotech, Ortenberg, Germany). A standard curve with known concentrations of cells was generated to determine RAW cell number in test cultures. A mouse tumor necrosis factor α (TNFα) antibody kit (Duo kit, R&D systems, Minneapolis, MN) was used according to the manufacturer's instructions to measure TNFα secreted by the RAW cells. The result was normalized to RAW cell number.

Lymphocyte activation assay

Twenty five thousand human allogeneic peripheral blood mononuclear cells (PBMCs) from 2 immunologically mismatched donors were labelled with 2.5µM carboxyfluorescein diacetate succinimidyl ester (CFSE; Invitrogen Carlsbad, CA) and co-cultured with 250 ihMSCs. The co-cultures were carried out in RPMI 1640 medium (Thermo Fisher) supplemented with 10% (v/v) human AB serum (CellGro, Corning, NY)) and 100 U/mL penicillin and 100µg/mL streptomycin for 7 days. The cells were

analyzed on a Cytomics FC500 flow cytometer (Beckman Coulter) and the data was processed using the accompanying CXP software.

Osteogenic differentiation

All reagents were obtained from Sigma unless stated otherwise. BM-hMSCs or ihMSCs were seeded in 6-well plates (9.6 cm^2, Corning, Corning, NY) in CCM until reaching 70-80% confluence. Two mL of osteogenic base medium (OBM) supplemented with 100nM dexamethasone was then added. OBM consists of CCM with 5mM β-glycerophosphate and 50µg/mL ascorbate-2-phosphate. Control wells only received CCM. The hMSCs were cultured for a further 21 days with fresh media added every 2 days. On day 21, the monolayers were washed twice with PBS and fixed with 4% paraformaldehyde (PFA, VWR International, Radnor, PA) for 15 minutes. The monolayers were then washed twice with PBS and once with distilled water. 40mM alizarin red S (ARS) at pH 4 was used to stain the monolayers for 30 minutes. The stain was removed and the monolayers were washed with distilled water until the unincorporated dye was removed. The mineral deposits were identified by bright red staining that occurs when ARS chelates calcium. Micrographs were taken with an inverted microscope (Nikon Eclipse, TE200) fitted with a DXM1200F digital camera (Nikon).

For semi-quantification of ARS, the water was aspirated from the wells and the monolayers were dried at 4ºC. 10% (v/v) acetic acid (Fisher Scientific, Hampton, NH) warmed to 50ºC was added to the monolayers and gently agitated for 30 minutes to extract the dye. The solution was then transferred to a 96-well plate (Corning, Corning,

NY) and the absorbance was read at 405nm on a FluoStar plate reader (BMG Biotech) [73].

Adipogenic differentiation

All reagents were obtained from Sigma unless stated otherwise. BM-hMSCs or ihMSCs were cultured in 6-well plates in CCM until 70-80% confluence was reached. Two mL of adipogenic differentiation medium (ADM) consisting of CCM supplemented with 500nM dexamethasone, 50nM isobutylmethylxanthine, and 500nM indomethacin, was added. Fresh ADM was added every 2 days for 21 days. Control wells received CCM. The monolayers were washed twice with PBS and fixed with 4% PFA on day 21. Fixed monolayers were washed twice in PBS and stained with 0.5% (w/v) Oil Red O solution for 20 minutes. Lipid vacuoles were observed by bright orange/red staining. An inverted microscope (Nikon Eclipse, TE200) fitted with a digital camera (Nikon DXM1200F) was used to obtain micrographs. ADM was supplemented with 10mM CTT0032374 (β-catenin antagonist), 10mM troglitazone (PPARγ agonist), or 10μM CTT00132374/troglitazone mixture to provide an additional adipogenic stimulus to ihMSCs.

Chondrogenic differentiation

All reagents were obtained from Sigma unless stated otherwise. 5 x 10^5 BM-hMSCs or ihMSCs were centrifuged at 500 x g for 10 minutes in a low adhesion 15mL polypropylene tube (Corning, Corning, NY) to aggregate the cells. Chondrogenic differentiation medium (CDM), which consisted of 1μM dexamethasone, 50μg/mL ascorbate-2-phosphate, 40μg/mL proline, 100μg/mL pyruvate, and 2X insulin transferrin

selenium-plus premix in high glucose Dulbecco's minimal-essential media (DMEM, Life Technologies, Carlsbad, CA) supplemented with 500ng/mL BMP-2 and 10ng/mL TGF-β3, was then added to cover the pelleted cells (300-500µl). The cells were incubated at 37ºC and 5% CO_2 for ~4-5 days until a spherical pellet was visible. Fresh media was added every 3 days following observation of the pellet. On day 21 the pellets were washed twice with PBS and fixed with 4% PFA for 15 minutes. The pellets were washed in PBS twice more, then dehydrated in an ascending series of alcohol gradients (50% (v/v)-100% (v/v)) and cleared with two washes of Sub-X clearing medium (Leica Biosystems, Richmond, IL). The pellets were then embedded in paraffin wax (Histoplast, Richard-Allen Scientific, San Diego, CA) and sectioned at 9µm using a rotary microtome (Thermo Scientific, Waltham, MA). The sections were then floated onto Superfrost Plus microscope slides (Fisher Scientific, Hampton, NH) in a water bath and dried on a slide warmer. Once dry, the slides were heated at 60ºC for one hour followed by clearing in Sub-X clearing medium, and rehydrated in a descending series of alcohol gradients (100% (v/v)-50% (v/v)). Toluidine blue borate was used to stain the slides for 10 minutes. The sulfated proteoglycans are identified by purple coloring. Images were taken with an upright microscope (Nikon Eclipse 80i) fitted with a Retiga 2000 digital camera.

Quantitative real time polymerase chain reaction (qRT-PCR)

BM-hMSCs and ihMSCs were cultured for 21 days in the appropriate differentiation conditions for the qRT-PCR on osteogenic, adipogenic, and chondrogenic markers. The ihMSCs were cultured for 8 days in OBM supplemented with 10µM

GW9662 for the assay on collagen transcripts. The cells were recovered by trypsin-EDTA if necessary, washed twice in PBS, and stored in liquid nitrogen until RNA extraction. Total RNA was extracted from the cells using a High Pure RNA isolation kit (Roche Diagnostics, Basel, Switzerland). Copy DNA (cDNA) was synthesized with a Superscript III kit (Life Technologies, Carlsbad, CA). The manufacturer's protocol was followed except for the use of a random hexamer/oligo-dT combination. SYBR Green (Life Technologies, Carlsbad, CA) or TaqMan gene expression assays (Thermo Fisher Scientific, Waltham, MA) were used to carry out qRT-PCR on a thermocycler fitted with a real time module (CFX96, BioRad Laboratories, Hercules, CA). Fold changes were calculated using the $2^{-\Delta\Delta CT}$ method [74]. Primer sequences are provided in **Table 1**. The data were log transformed, z-normalized to the same scale, and plotted with Rstudio (v1.1.435), ggplot (3.0.0), dplyr (0.7.6) and reshape (1.4.3) programs to generate heat maps by Simin Pan, a graduate student in the Department of Molecular and Cellular Medicine.

Table 1: Primer sequences and PCR conditions used in Chapter II. RTPrimerDB refers to the http://www.rtprimerdb.org/ database.

Target	Sequence	Reference / notes
GAPDH	FOR CTCTCTGCTCCTCCTGTTCGAC REV TGAGCGATGTGGCTCGGCT	75
collagen I	FOR GAACGCGTGTCATCCCTTGT REV GAACGAGGTAGTCTTTCAGCAACA	RTPrimerDB ID_1089
collagen III	FOR GGGAACAACTTGATGGTGCTACT REV TCAGACATGAGAGTGTTTGTGCAA	RTPrimerDB ID_4463
collagen V	FOR CACAACTTGCCTGATGGAATAACA REV GCAGGGTACAGCTGCTTGGT	RTPrimerDB ID_1091
collagen VI	FOR CCATCGTGCGCAGCC REV TGCGCCGACTCGTGC	44
collagen X	FOR AATGCCTGTGTCTGCTTTTAC REV ACAAGTAAAGATTCCAGTCCT	76
collagen XI	FOR GACTATCCCCTCTTCAGAACTGTTAAC REV CTTCTATCAAGTGGTTTCGTGGTTT	RTPrimerDB ID_1736
collagen XII	FOR CTTCCATTGAGGCAGAAGTT REV AGACACAAGAGCAGCAATGA	77
collagen XV	FOR CGTGTTAGAGATGGCTGGA REV GTTTGGTGGAGGCAGAAG	78
collagen XIV	FOR TCCGAGGAATGGTATAACCGG REV TGGACCAGGAACACTGACAGG	79
collagen XXI	FOR GCGCAGGTCTTGCTCGGGTT REV CTGGTGCTCCGGGGCAGGAT	44
runx2	FOR GCAAGGTTCAACGATCTGAGA REV TCCCCGAGGTCCATCTACTG	80
alkaline phosphatase	FOR GACCCTTGACCCCCACAAT REV GCTCGTACTGCATGTCCCCT	81
osteocalcin	FOR TGAGAGCCCTCACACTCC REV CGCCTGGGTCTCTTCACTAC	82
PPAR gamma	FOR CACAAGAACAGATCCAGTGGTTGCAG REV AATAATAAGGTGGAGATGCAGGCTCC	RTPrimerDB ID_2420
RXR alpha	REV TTCGCTAAGCTCTTGCTC FOR ATAAGGAAGGTGTCAATGGG	RTPrimerDB ID_2520
FABP4	FOR TCAGTGTGAATGGGGATGTGA REV TCAACGTCCCTTGGCTTATGC	RTPrimerDB ID_1965
lipoprotein lipase	FOR GGAATGTATGAGAGTTGGGT REV GGGCTTCTGCATACTCAAAG	83
collagen II	FOR CAACACTGCCAACG TCCAGAT REV GTGGTAGGTGATGTTCT	81
COMP	FOR GACAGTGATGGCGATGGTAT REV GTCATTGTCGTCGTCGTCGT	84
SOX5	FOR GTGGCTGTTGTGAATAGTCT REV CCATCATGGCATGGCTAAAT	RTPrimerDB ID_8554

Immunoblotting

BM-hMSCs or ihMSCs were cultured in CCM (standard), OBM (osteogenic), OBM supplemented with 10µM GW9662 (osteogenically enhanced) or DMSO (vehicle control) for 10 days. The cells were recovered with trypsin-EDTA, washed in ice cold PBS, and stored in liquid nitrogen until protein extraction. The cells were thawed and lysed in ice cold extraction buffer consisting of 0.1% (v/v) Triton X-100 (Bio-Rad laboratories, Hercules, CA) and protease inhibitors (Roche Diagnostics, Basel, Switzerland) for 15 minutes. The cells were then centrifuged at 14,000 x g for 15 minutes and the supernatant (soluble fraction) was recovered and stored at -20º C. The remaining cell pellet was washed twice with extraction buffer before resuspension in extraction buffer with 1% (w/v) sodium dodecyl sulphate (SDS, Invitrogen, Carlsbad, CA) added. The pellet was heated at 60º C in a water bath for until it had solubilized (~ 1 hour). The resultant solution (insoluble fraction) was then stored at -20º C. Immunoblotting for collagens VI and XII were performed on whole cell lysates. The samples were heated at 95 ºC for 5 minutes and centrifuged for 5 seconds at 8,000 x g to collect condensate. The proteins were separated by electrophoresis using NuPage 4-12% bis-Tris gels (Invitrogen, Carlsbad, CA) in 1X Novex 2-(N-morpholino)ethanesulfonic acid (MES) buffer (Invitrogen, Carlsbad, CA). The gels were then transferred to a 0.2 µm Protran nitrocellulose membrane (GE Healthcare Life Sciences, Chicago, IL). Blots were blocked for 1 hour in 5% (w/v) bovine serum albumin (BSA, Sigma, St. Louis, MO) or instant dry milk (For β-Actin only, Walmart, Bentonville, AR) in PBST (PBS supplemented with 0.1% (v/v) Tween 20 (Sigma, St Louis, MO)). Blots were then

incubated with the primary antibody diluted in blocking buffer overnight at 4º C. The following day the blots were washed 3 times in PBST and incubated with a peroxidase-conjugated secondary antibody for 2 hours at room temperature. Signal was developed by chemiluminescence with a developing solution consisting of 450µM luminol sodium salt (Sigma, St. Louis, MO), 450µM paracoumaric acid (Sigma, St. Louis, MO), and 0.018% (v/v) hydrogen peroxide in 0.1M Tris at pH 8.0 [85]. Images were taken immediately after addition of the developing solution with a Versadoc gel imager (Bio-Rad Laboratories, Hercules, CA) and densitometry was performed with the accompanying Quantity One software (Bio-Rad Laboratories, Hercules, CA). The antibodies used were mouse anti-human GAPDH (clone 6C5, Chemicon International, Temecula, CA), mouse anti-human β-catenin (clone 5H10, Chemicon International, Temecula, CA), mouse anti-human GSK3β (clone M131, Abcam, Cambridge, United Kingdom), mouse anti-human PPARγ (clone 1E6A1, Abcam, Cambridge, United Kingdom), goat anti-mouse IgG-peroxidase conjugate (Thermo Fisher Scientific, Waltham, MA), rabbit-anti human type VI collagen (NBP159126, Novus Biologicals, Littleton, CO), rabbit-anti human type XII collagen (NBP1-88062, Novus) and goat anti-rabbit IgG-peroxidase conjugate (Biomeda, Foster, CA).

Alkaline phosphatase (ALP) kinetic assay

The ihMSCs were seeded in a 12 well plate (3.8cm^2, Corning, Corning, NY) in CCM until reaching 70-80% confluence with fresh media added every 2 days. The cells were then cultured in OBM supplemented with DMSO, 1, 5, or 10µM GW9662 (Sigma, St. Louis, MO) for 8 days. On day 8, the monolayers were washed twice with PBS

followed by a single wash in ALP reaction buffer (100mM Tris-HCl, pH 9, 100mM KCl, and 1mM $MgCl_2$). An equal volume of ALP buffer and p-nitrophenol phosphate (PNPP, Life Technologies, Carlsbad, CA) was added to each well. The absorbance was recorded at 405nm every 30 seconds for 10 minutes using a FluoStar plate reader (BMG Biotech). The data was normalized to cell number using a CyQuant cell proliferation assay (Thermo Fisher, Waltham, MA) based on fluorescent DNA intercalation. The plates were frozen at – 20ºC for 24 hours before the addition of lysis buffer consisting of PBS with 1mM $MgCl_2$, 0.1% (v/v) Triton X 100 (Bio-Rad laboratories, Hercules, CA), 1U/mL *ECO*RI (Life Technologies, Carlsbad, CA) and 1U/mL *Hind*III (Life Technologies, Carlsbad, CA) to release DNA from particulate matter. The plates were incubated for 16 hours in a humidified incubator at 37ºC with gentle rocking to allow DNA to be released from the dense mineralized monolayers. Standards were quantified from 1 x 10^6 cell pellets incubated with the lysis buffer for 4 hours. An equal volume of CyQuant buffer, consisting of lysis buffer with 2X CyQuant GR dye (Life Technologies, Carlsbad, CA) was added to the samples and standards. The samples and standards were transferred to a black flat-bottomed 96 well plate (Corning, Corning, NY) and the fluorescence was read at 485/520 excitation/emission with a FluoStar plate reader (BMG Biotech). A standard curve was generated to determine cell number.

Extracellular matrix production (ECM) and analysis

BM-hMSCs or ihMSCs were cultured in CCM at an initial density of 100 cells per cm^2 on a 148cm^2 plate (Corning, Corning, NY) until reaching 70-80% confluence. The CCM was then replaced with OBM supplemented with either 10µM GW9662 or an equal volume of DMSO. Media was replaced every second day for 10 days. On day 10, the monolayers were washed twice with PBS and frozen at -80ºC overnight to disrupt the ECM and cell membranes. Monolayers were thawed in room temperature PBS and scraped from the plate with a cell scraper (Corning, Corning, NY) and transferred to a 15mL tube. The ECM/cell slurry was then centrifuged at 1000 x g for 10 minutes and resuspended in extraction buffer consisting of PBS with 1mM $MgCl_2$, 0.1% (v/v) Triton X 100 supplemented with 10µg/mL DNAse I (Sigma, St. Louis, MO). The ECM was incubated at 37ºC with orbital mixing at 60 rpm for 2 hours before the addition of 0.1% (v/v) trypsin(MP Biomedicals, Santa Ana, CA) and incubated for a further 16 hours. ECM was then washed twice in excess dH_2O, once in chloroform, twice again in dH_2O, and finally once in acetone before being allowed to air dry. Dried ECM was stored at -80ºC.

Air-dried ECM was sputter coated with iridium using a Cressington 208HR high resolution sputter coater (Cressington Scientific Instruments, Hertfordshire, United Kingdom). Samples were visualized and energy dispersive X-ray spectroscopy (EDS) was performed using a FEI Quanta 600 FE-SEM (Thermo Fisher Scientific, Waltham, MA). Scanning electron microscopy was performed by Tom Stephens at the Texas A&M Microscopy and Imaging Center.

A Pierce BCA protein assay kit (Thermo Fisher Scientific, Waltham, MA) was used to quantify the protein content of the matrices. Matrices were solubilized in 2M Urea in Tris-HCl pH 8 at 60ºC. The kit was used with no deviations from the manufacturer's instructions.

An Arsenazo III (TCI American, Portland, OR) calcium quantification assay was performed to determine the calcium content of the matrices. Matrices were solubilized in 6M HCl at 80ºC. The resultant solution was cooled to room temperature and neutralized to pH 5 with 2.5M Trizma base (Sigma, St. Louis, MO). 100µM Arsenazo III was added to the samples or calcium chloride standards in a clear flat-bottomed 96-well plate (Corning, Corning, NY). The plate was incubated at room temperature for 5 minutes. Aresenazo III changes from pink/purple to blue in the presence of calcium. The absorbance was measured at 595nm on a FluoStar plate reader (BMG Biotech) [86].

Mass spectrometry and proteomic analysis

All reagents were acquired Fluka Honeywell Research Chemicals (Charlotte, NC) or Sigma (St. Louis, MO) unless otherwise stated. Matrices were solubilized in 1X NuPage LDS sample buffer (Invitrogen, Carlsbad, CA) at 60ºC. The solubilized matrices were separated on a 4-20% Mini-Protean TGX precast gel (Bio-Rad Laboratories, Hercules, CA) and stained with SimplyBlue SafeStain (Invitrogen, Carlsbad, CA) for 1 hour at room temperature. Excess stain was washed off with dH_2O. The resultant bands were excised and de-stained by 2 cycles of 2:1 acetonitrile in 50mM ammonium bicarbonate for 30 minutes, followed by 25mM ammonium bicarbonate for 30 minutes. The proteins were reduced with 5mM dithiothrietol for 1 hour, followed by alkylation in

5.5 mM iodoacetamide. The proteins were then digested with 25µg/mL trypsin for 16 hours at 36ºC. Peptides were desalted, and purified for mass spectrometry using Ziptip C18 column (EMD Millipore, Burlington MA). Digested samples were suspended in 0.1% formic acid (FA) before separation analysis by LC-MS with a Dionex UltiMate 3000 ultra-high performance liquid chromatography (UHPLC) system-Orbitrap Fusion Tribrid Mass Spectrometer (Thermo Fisher Scientific, Waltham, MA). The LC gradient was set up at 4µl/min using a 2-90% gradient of 0.1% (v/v) FA in acetonitrile (buffer B) against 0.1% (v/v) FA in dH_2O (buffer A). The detection settings were; spray voltage of 2.3 KV, orbitrap resolution of 120 K, scan range of 400-1600, and higher-energy C-trap dissociation energy (HCD) of 28%. Data was analyzed with Proteome Discoverer 2 software (Thermo Fisher Scientific, Waltham, MA). Mass spectrometry was performed by Dr. Doyong Kim at the Texas A&M University Center for Mass Spectrometry. The data was analyzed and the resultant figures were generated by Simin Pan, a graduate student in the Department of Molecular and Cellular Medicine.

Murine calvarial defect model

Vertebrate animal studies were approved by the Texas A&M University Institutional Animal Care and Use Committee. Eight week old immune compromised Nu/Nu mice (Charles Rivers Laboratories, Wilmington, MA) received a 3mm circular lesion in the parietal calvarial bone using a 2.33mm osteotomy burr (Roboz Surgical, Gaithersburg, MA), located approximately 2mm from the sagittal and coronal sutures. OEihMSCs for *in vivo* assays were seeded in 148cm^2 plates in CCM. Fresh media was added every second day. Upon reaching 70-80% confluence, OBM supplemented with

10μM GW9662 was added to the plates to induce the OEihMSC phenotype. Media was replaced every second day. On day 10, the monolayers were washed with PBS and recovered with trypsin-EDTA at 37ºC for 5 minutes. Trypsin-EDTA was blocked with fresh CCM, and the cells were washed with PBS. OEihMSCs were passed through a 70μm filter (Corning, Corning, NY) to remove residual ECM and counted with a hemocytometer. $2x10^6$ OEihMSCs were prepared per animal and stored on ice (≤ 2 hours) until implantation in a defect. For groups receiving hBM, $5x10^6$ hBM cells were recovered prior to surgeries and stored on ice (≤ 2 hours) until use.

$2x10^6$ OEihMSCs or $5x10^5$ hBM cells were suspended in 30μl of reconstituted human plasma (Sigma, St. Louis, MO). 30μl of thromboplastin (Pasinex, Horsham, PA) was added to the cell suspensions immediately prior to implantation. Gelfoam (Baxter International, Deerfield, IL) or OEihMSC-ECM was administered into the defect prior to the cells for groups containing the scaffolds. Gelfoam saturated with 0.1 mg/mL BMP-2 (Infuse, Medtronic, Minneapolis, MN) served as a positive control [87] while human plasma/thromboplastin without cells or scaffolds served as the negative control. The incision was sutured closed and postoperative analgesia was administered subcutaneously for 2 days following the surgery. Sutures were removed after 7 days.

The mice were euthanized 4 weeks after the surgery. The calvaria were excised from the skull with a 5mm diameter fine rotary blade (Strauss Diamond Palm Coast, FL) immediately after euthanasia. Calvaria were washed in PBS and fixed in 10% neutral buffered formalin (NBF, VWR International, Radnor, PA) for 24 hours. The calvaria were then washed in PBS and transferred to Carson's fixative consisting of 1.86%

sodium phosphate monobasic, 0.42% (w/v) sodium hydroxide, and 10% (v/v) formaldehyde. Calvaria were stored at 4ºC.

Micro-computed tomography (µCT) analysis

Prior to µCT analysis, the calvaria were removed from Carson's fixative, washed in PBS and carefully wrapped in Parafilm (VWR International, Radnor, PA). The µCT scans were performed with a Skyscan 1275 system (Bruker, Billerica, MA). The calvaria were scanned over 360º with a 30kV beam and 18µM camera resolution. Flat field correction and frame averaging were enabled. Images were captured every 0.5º. NRecon (Micro Photonics Inc., Allentown, PA) was used to generate axial reconstructions. Smoothing and beam hardening were kept at 1(smooth kernel Gaussian) and 5% respectively. Misalignment compensation, ring artefact reduction, and cross sectional rotation were manually adjusted as required. The dynamic range was set with a lower limit of 0 and an upper limit of 0.111204. Fresh ECM placed into a mock calvarial defect was scanned and reconstructed using the above parameters to determine a threshold that would distinguish between ECM and newly formed bone. The threshold was applied during quantification and visualization of bone healing to ensure ECM remaining in the defect would not interfere with the result. 3D models were generated from the reconstructions using CTvox (Micro Photonics Inc., Allentown, PA). The quantity and quality of new bone was measured with CTan (Micro Photonics Inc., Allentown, PA). The system was calibrated with calcium hydroxyapatite phantoms (Bruker, Billerica, MA) to measure bone mineral density using the attenuation coefficient method.

Histology

Following completion of µCT analysis, calvaria were washed in PBS and decalcified in 1M dibasic EDTA, pH 8.0 (Sigma, St. Louis, MO). Decalcification took approximately 2 weeks with the decalcification solution replaced every second day. Decalcification was confirmed by radiolucency on µCT scans. The calvaria were trimmed to a size encompassing the defect and ~2mm of surrounding tissue. The calvaria were washed in PBS before dehydration in a series of alcohol gradients (50% (v/v)-100% (v/v)) followed by Sub-X clearing medium. The calvaria were then embedded in paraffin wax (Histoplast, Richard-Allan Scientific). 9µm sections were cut using a microtome (Leica Biosystems) and floated onto Superfrost Plus microscope slides (Fisher Scientific, Hampton, NH) in a warm (45º C) water bath to prevent wrinkles in the sections. The slides were dried on a slide warmer overnight. Sections were baked onto the slides at 60ºC for one hour, deparaffinized with Sub-X clearing medium, and rehydrated in a series of alcohol washes (100% (v/v)-50% (v/v)).

For hematoxylin and & eosin staining (H&E), the slides were stained with hematoxylin solution Gill number 3 (Sigma, St. Louis, MO) and counterstained with 1% (w/v) eosin Y (Thermo Fisher Scientic, Waltham, MA). Masson's trichrome staining was performed using a kit (American Master Tech Scientific, McKinney, TX) according to the manufacturer's protocol. Slides were stained overnight in Bouin's Fluid, followed by Weigert's working hematoxylin, Biebrich scarlet acid fushsin, phosphotungstic/phosphomolybdic acid, aniline blue, and finally washed in 1% acetic acid. Tartrate-resistant acid phosphatase (TRAP) staining was performed with an acid

phosphatase/leukocyte kit (Sigma, St. Louis, MO). Slides were incubated for one hour at 37ºC in pre-warmed dH_2O containing diazotized Fast Garnet GBC, Naphthol AS-BI phosphate solution, acetate solution and tartrate solution. The slides were counterstained with Fast Green Stain which was the only deviation from the manufacturer's procedure. Image J (National Institute of Health, Bethesda, MD) was used to quantify positive TRAP staining. Following all stains, slides were dehydrated in a series of alcohol washes (50% (v/v)-100% (v/v)), followed by 2 washes in Sub-X clearing medium. Cover slips were applied with Permount mounting medium (Fisher Scientific, Hampton, NH).

Results

Characterization of ihMSCs

A series of comparative experiments were performed to establish whether the iPSCs had differentiated into MSC-like cells that met the required criteria to define an MSC [25,72]. Phase contract microscopy confirmed that the ihMSCs exhibited the fibroblast-like morphology typical of hMSCs (**Fig4a**).

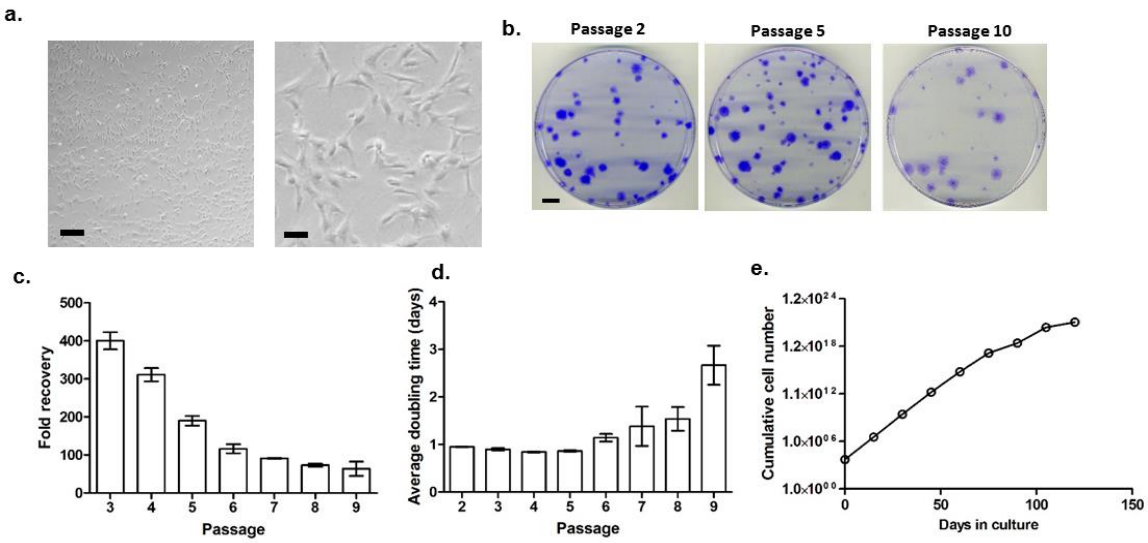

Figure 4: Morphology and proliferative capacity of ihMSCs. **Panel a:** Phase contrast micrographs of ihMSC monolayer (*bar*, left = 250µm, *bar*, *right* = 25µm). **Panel b:** Micrographs of colonies generated from by ihMSCs. (*bar* = 10mm). **Panel c:** Fold recovery in 7 days after plating at 500 cells per cm^2 after 3-9 passages. **Panel d:** average doubling time for cultures from **panel c**. **Panel e:** cumulative cell yield over 120 days.

Unlike iPSCs, MSCs possess proliferative senescence. A number of growth assays were carried out to determine if ihMSCs possessed a proliferative capacity resembling iPSCs or BM-hMSCs [72]. Colony forming potential of ihMSCs was comparable to BM-hMSCs with a reduction in CFU potential observed after passage 5 (**Fig4b**). The ihMSCs also exhibited a proliferation rate with seed-to-harvest doubling time similar to that of BM-

hMSCs (**Fig4c-e**) [88]. These data suggest that ihMSCs possess proliferative senescence, like tissue-derived hMSCs, and do not possess the proliferative immortality of iPSCs [81]. Flow cytometry confirmed the expression (≥98%) of CD73, CD90 and CD105 and a lack of expression (≤2%) of HLA-DR, CD14, CD19, CD34 and CD45 (**Fig5a**).

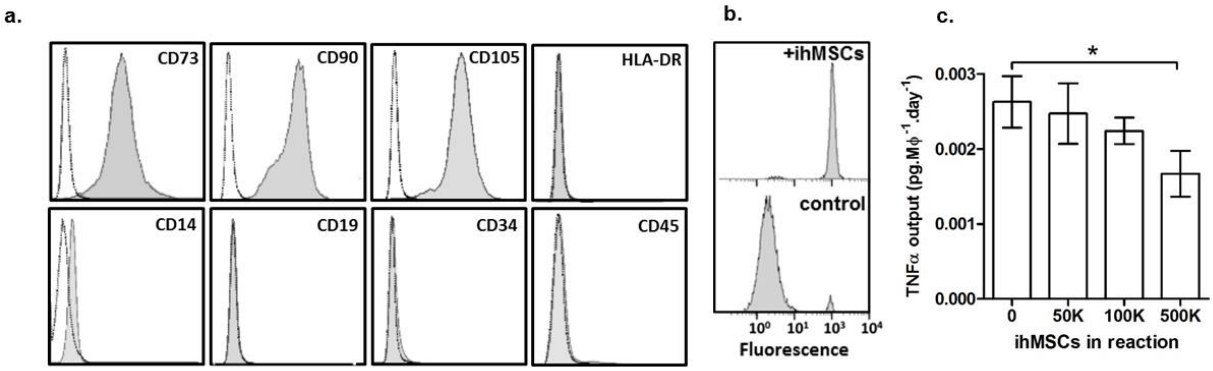

Figure 5: Immunophenotype and immunomodulatory capacity of ihMSCs. **Panel a:** Flow cytometry confirms ihMSCs possess expected immunophentotype. **Panel b:** Lymphocyte stimulation assay shows that ihMSCs inhibit lymphocyte proliferation as measured by CFSE dilution that occurs on proliferation of CFSE-loadaed lymphocytes. **Panel c:** TNFα secretion by LPS-stimulated macrophages is inhibited by ihMSCs. Statistics: The data are presented as means with standard deviations. Comparisons were carried out with ANOVA with Tukey's post test. * = $P<0.05$. n = 6.

This established that ihMSCs possess the necessary immunophenotype indicative of a hMSC. The immunomodulatory properties of hMSCs are well established [89] with the ability to inhibit both innate and adaptive immune responses. The ihMSCs were co-cultured with murine macrophages and human T-cells to determine if ihMSCs possessed a similar immunomodulatory capacity to tissue-derived hMSCs. Tumor necrosis factor α (TNFα) is produced by macrophages to promote an inflammatory response [19]. When co-cultured with LPS-stimulated macrophages, ihMSCs were capable of suppressing TNAα secretion (**Fig5c**) demonstrating that like tissue-derived hMSCs, they possessed anti-

inflammatory properties. Co-culture of ihMSCs in a mixed lymphocyte assay, with two genetically distinct populations of human lymphocytes, resulted in an inhibitions of lymphocyte proliferation (**Fig5b**) demonstrating that ihMSCs have similar immunomodulatory properties to tissue-derived hMSCs [90]. ARS staining for mineralization confirmed that the ihMSCs readily undergo osteogenesis (**Fig6a**). Extraction and quantification of the dye suggested that ihMSCs have superior capacity for mineralization as compared to both BM-hMSC preparations tested (**Fig6b**). This was surprising as the BM-hMSC1 preparation is highly osteogenic based on previous studies [42,43]. Toluidine blue staining of chondrocyte micromasses confirmed that ihMSCs can differentiate into chondrocytes by confirming the presence of sulfated proteoglycans (**Fig6a**) [91], but volumetric measurements showed that there was no difference in micromass volume between ihMSCs and both BM-hMSC preparations (**Fig6e**). The ihMSCs did not generate adipocytes as readily as either BM-hMSC preparations (**Fig6a**). Differentiation of adipocyte progenitors is accompanied by stimulation of PPARγ and concomitant reduction in canonical Wnt signaling. By enhancing the adipogenic stimulus with PPARγ agonist Troglitazone, β-catenin inhibitor CCT032374, or a combination of both, a modest adipogenic response was observed (**Fig6d**). Together, the data confirm that ihMSCs exhibit the minimum criteria required to define hMSCs [25] and also indicates that they have superior osteogenic properties.

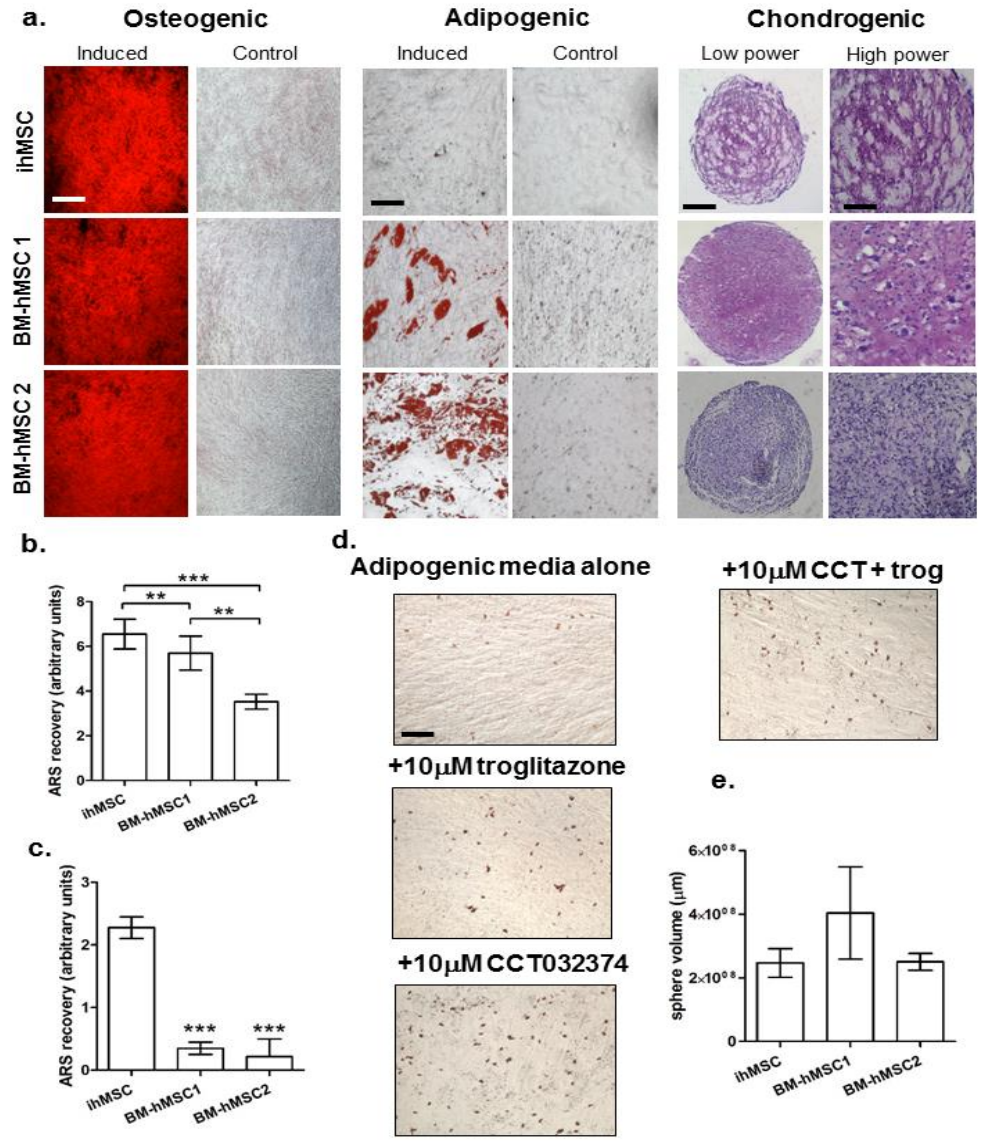

Figure 6: Differentiation potential of ihMSCs compared to two bone marrow-derived hMSC preparations. **Panel a:** Standard osteogenic (*left*), adipogenic (*center*) and chondrogenic (*right*) assays on ihMSCs and two bone marrow-derived hMSC preparations. For osteogenic and adipogenic assays *bar* = 200μm. For chondrogenic assays *bar* = 250μm (low power, *left*) and 50μm (high power, *right*). **Panel b:** ARS quantification demonstrates ihMSCs mineralize more readily than either BM-hMSC preparations. **Panel c:** ARS quantification in the absence of dexamethasone. **Panel d:** Enhanced adipogenic stimulation of ihMSCs with PPARγ agonist troglitazone (trog) and β-catenin inhibitor (CCT032374). **Panel e.** Volumes of chondrogenic micromasses generated from ihMSCs and BM-hMSCs. Statstics: The data (n=3) are presented as means with standard deviations and were compared using ANOVA with Tukey's post test. * = $P<0.05$, ** = $P<0.01$, *** = $P<0.005$.

Quantitative RT-PCR for lineage specific transcripts was employed to further characterize the potential variations in differentiation potential. The qRT-PCR data supported the observations from the differentiation assays that ihMSCs have superior osteogenic capacity (**Fig7b, Fig8**) and inferior adipogenic properties (**Fig7d, Fig8**) compared to either BM-hMSC preparation. Each hMSC preparation had comparable chondrogenic gene expression (**Fig7c, Fig8**), supporting the observations from the micromass assay. The data also confirm that BM-hMSC1 has a greater osteogenic potential than BM-hMSC2. Dexamethasone is required to promote mineralizaton in hMSCs by activating Runx2 [92], yet the ihMSCs were capable of mineralizing in the absence of dexamethasone (**Fig6c**). Ascorbic acid, a component of OBM, increases collagen I secretion to the ECM. The secreted collagen I provides an osteogenic signal to the cells via $\alpha_2\beta_1$ integrin signaling and subsequent activation of the mitogen-activated protein kinase (MAPK) signaling pathway and downstream activation of osteogenic genes [93]. While this increase in collagen I secretion does not typically provide a sufficient stimulus to induce osteogenesis in BM-hMSCs in the absence of dexamethasone, it has been reported that collagen I-coated surfaces can induce osteogenesis in the absence of dexamethasone [94]. This may be due to increased collagen I present on the coated surface than secreted by the cells. Osteogenesis in the absence of dexamethasone by ihMSCs could therefore be explained by a significantly increased amount of collagen I and therefore ECM secreted as compared to BM-hMSCs.

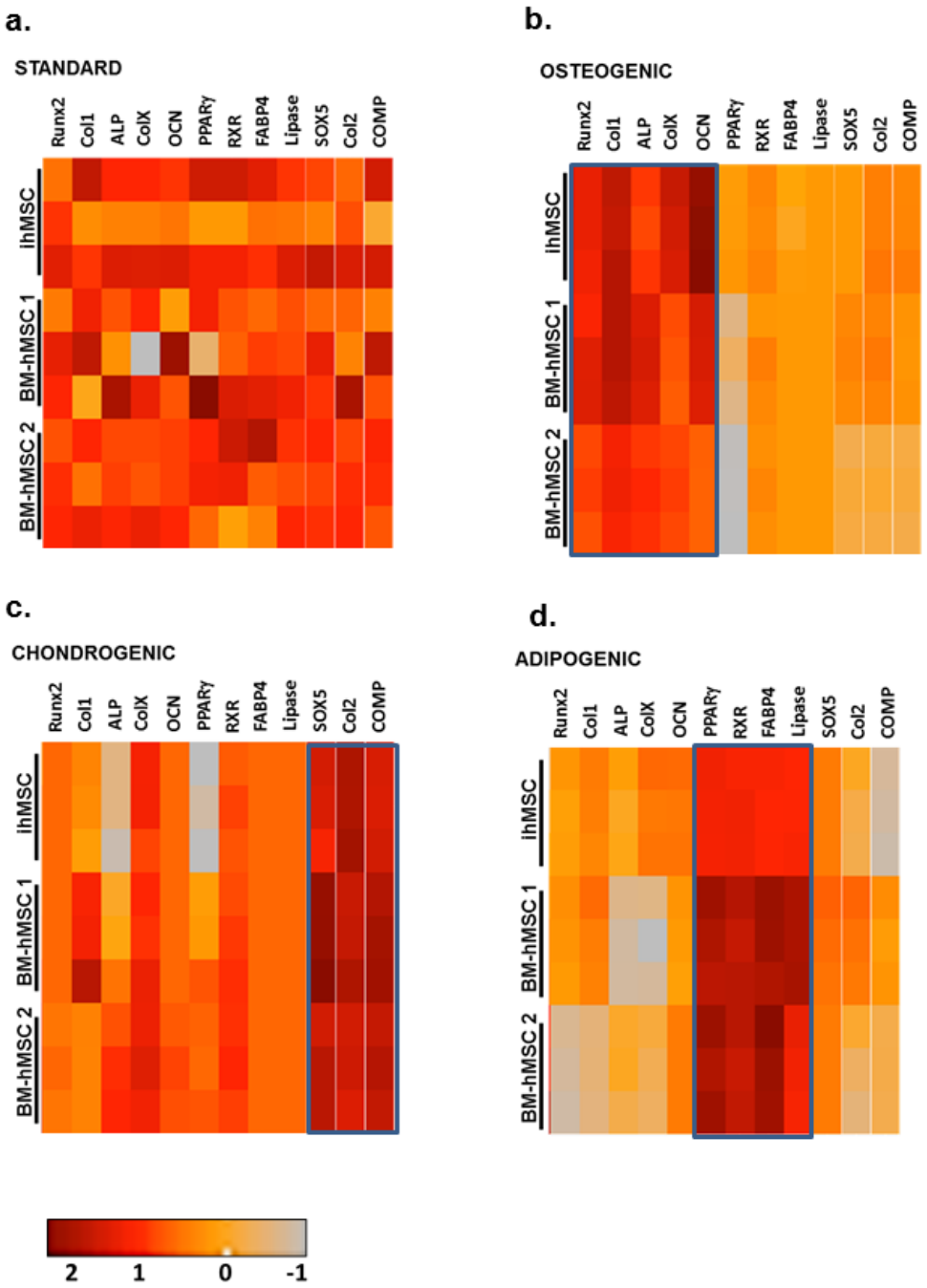

Figure 7: ihMSCs exhibit a greater upregulation of osteogenic transcripts and a lower upregulation of adipogenic transcripts than BM-hMSCs in response to appropriate stimuli. Heat maps summarizing fold-change transcription of differentiation biomarkers. The scale represents z-score. Raw data is presented in **Fig 13**. Transcription of each biomarker was measured in response to control (**Panel a**), **Panel b**: osteogenic (**Panel b**), chondrogenic (**Panel c**), and adipogenic stimuli (**Panel d**).

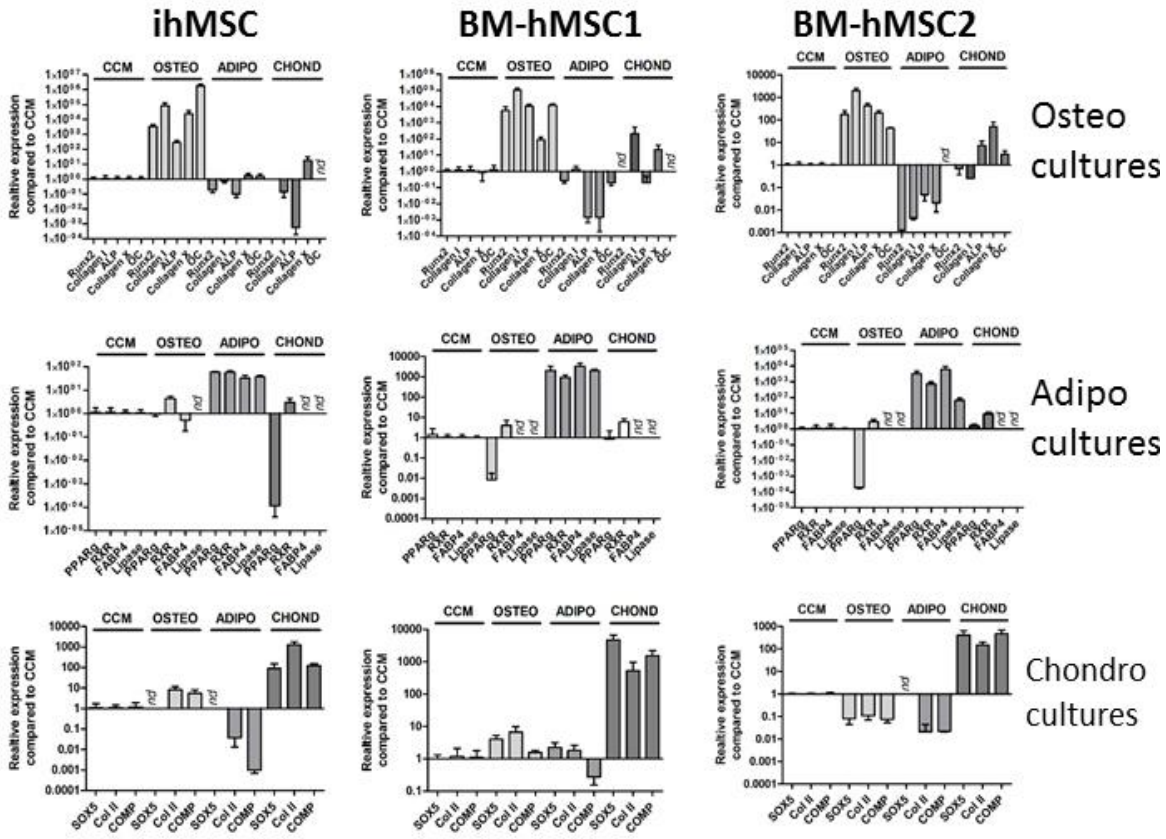

Figure 8: Quantitative RT-PCR data used to generate heatmaps in Fig7. Cultures were exposed to standard differentiation assays and subjected to panels of biomarkers corresponding to osteogenesis, adipogenesis and chondrogenesis (*x-axis*). All fold changes are compared to complete culture media (CCM) containing no differentiation supplements. Assays generating signal below detectable limits are annotated with *nd*.

Generation of OEihMSCs

It is well established that cWnt signaling and PPARγ signaling are upregulated in hMSCs receiving an osteogenic or adipogenic stimulus respectively [36-38]. In the absence of an osteogenic stimulus, cytosolic β-catenin is degraded by GSK3β-mediated proteolysis [36]. This prevents β-catenin from translocating to the nucleus and transcriptionally upregulating osteogenic genes such as Runx2 [37]. Degradation of β-catenin is promoted by PPARγ signaling [38]. Inhibition of PPARγ signaling with GW9662 removes the negative crosstalk from the PPARγ signaling pathway and shifts

the balance in favor of cWnt signaling, resulting in the generation of OEhMSCs [35]. Due to the superior osteogenic properties and reduced adipogenic capacity of the ihMSCs it was hypothesized that the competitive relationship between the cWnt signaling and PPARγ pathways may favor cWnt signaling. Immunoblotting was employed to determine the role of cWnt signaling in osteogenesis by ihMSCs.

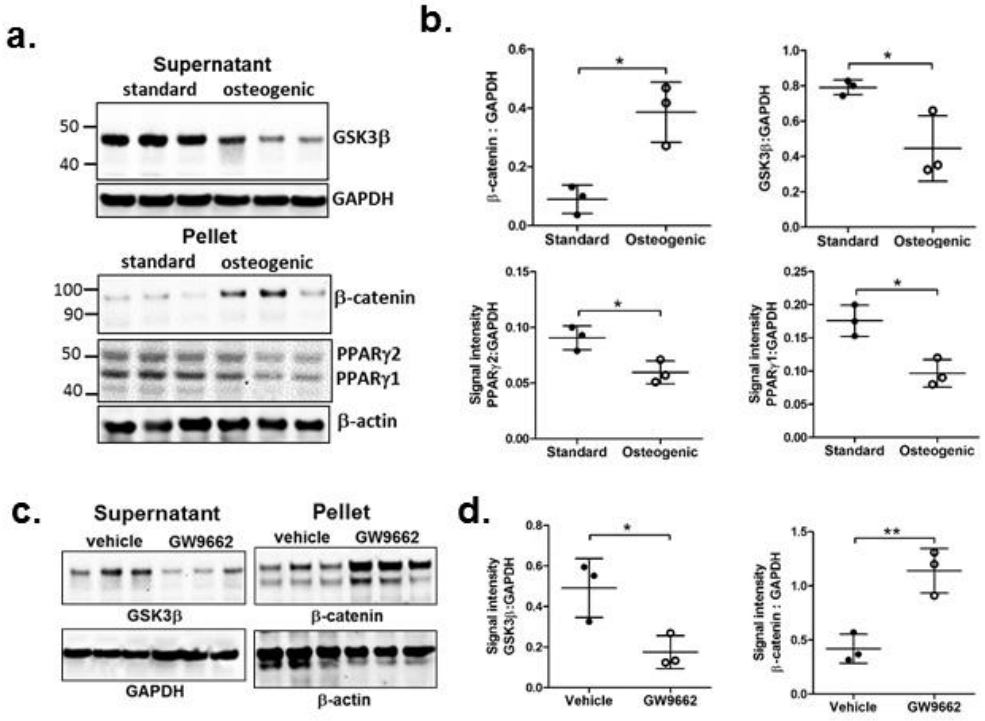

Figure 9: Osteogenesis by ihMSCs is regulated by the cWnt/PPARγ axis and inhibition of PPARγ crosstalk with GW9662 increases cWnt signaling. **Panel a:** Immunoblotting of ihMSCs extracts for GSK3β, β-catenin and PPARγ in response to an osteogenic stimulus. "*Supernatant*" and "*Pellet*" represent the cytosolic and insoluble organellar extracts respectively. **Panel b:** Semi-quantification of images from **panel a** by densitometry. **Panel c:** Exposure to GW9662 under osteogenic conditions. **Panel d:** Semi quantification of images from **panel c** by densitometry. **Statistics:** The data (n=3) are presented as means with standard deviations and were compared using ANOVA with Tukey's post test. * = P<0.05, ** = P<0.01, *** = P<0.005.

Cytosolic GSK3β was downregulated and β-catenin was upregulated in the nuclear fraction in response to osteogenic conditions (**Fig9a,b**) which is indicative of increased cWnt signaling [35]. Along with upregulation of osteogenic transcripts, β-catenin downregulates the transcription of PPARγ. PPARγ1 and PPARγ2 were both downregulated in response to osteogenic conditions (**Fig9a,b**). This suggests that like BM-hMSCs, ihMSCs exhibit balanced cWnt and PPARγ signaling with the expected shift towards increased cWnt signaling in response to an osteogenic stimulus. Furthermore, this data indicate that ihMSCs should be responsive to osteogenic enhancement by GW9662.

Cytosolic GSk3β was further downregulated when ihMSCs were treated with OBM supplemented with 10μM GW9662 when compared to the DMSO vehicle control (**Fig9c,d**). Upregulated nuclear β-catenin was also observed following GW9662 treatment (**Fig9c,d**). This suggested that ihMSCs could be osteogenically enhanced in the same manner as BM-hMSCs, despite their already superior osteogenic qualities. In support of this prediction, ALP activity, a robust marker for osteogenesis, was increased in OEihMSCs in response to GW9662 exposure (**Fig10a**). Furthermore, phase contrast microscopy highlighted that induction of mineralized nodules by GW9662 occurred in a dose-dependent manner (**Fig10b**) and subsequent ARS staining revealed that GW9662 exposure promoted superior mineralization by ihMSCs both in the presence and absence of dexamethasone (**Fig10c,d**). These data confirm that like BM-hMSCs [35,42,44], an osteogenically enhanced phenotype can be induced in ihMSCs by GW9662 exposure.

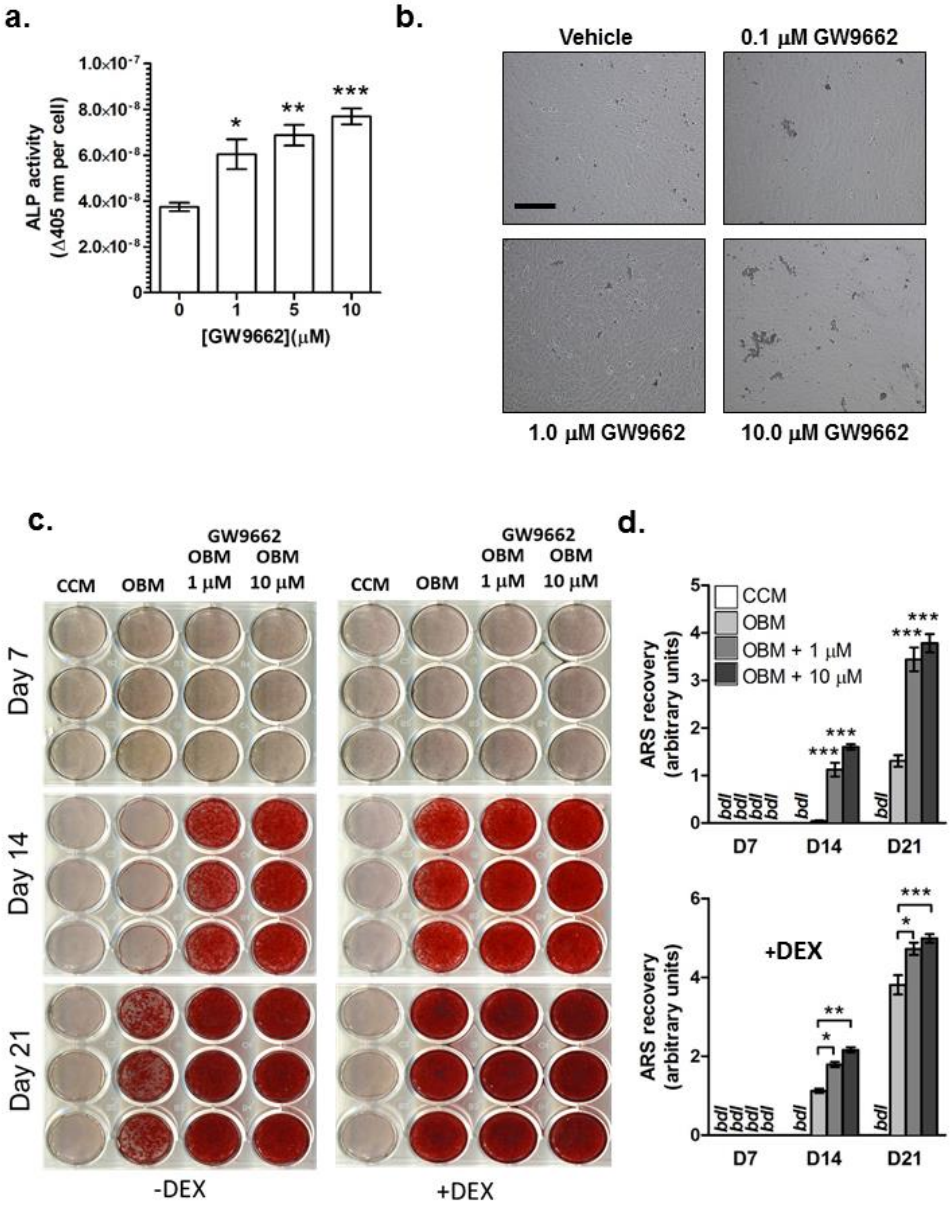

Figure 10: Osteogenic enhancement of ihMSCs (OEihMSCs) by exposure to GW9962.Panel a: Upregulation of osteogenic biomarker ALP in OEihMSCs on day 8 with GW9662 exposure. **Panel b:** GW9662 induces matrix deposition by ihMSCs in a dose – dependent manner. (*bar* = 150μm**) Panel c:** Mineralization of ihMSCs in osteogenic conditions in the presence and absence of dexamethasone with doses of GW9662. **Panel d:** Extraction and quantification of ARS dye from panel c (*bdl* = below detection limit) **Statistics:** The data (n=3) are presented as means with standard deviations and were compared using ANOVA with Tukey's post test. * = P<0.05, ** = P<0.01, *** = P<0.005.

Characterization of OEihMSC-ECM

Secretion of a dense osteogenic ECM is a characteristic of the osteogenically enhanced hMSC phenotype [42-44]. It was previously established that OEhMSC-secreted ECM is comprised of factors enriched in anabolic bone, and promotes bone healing by OEhMSCs *in vivo* [42-44]. Based on the data described above it was expected that OEihMSCs would secrete a highly osteogenic ECM. ECM was generated from OEihMSCS and OEhMSCs following 10 days in osteogenic media supplemented with 10 μM GW9662 or DMSO vehicle control. OEhMSC1 and OEhMSC2 represent the osteogenically enhanced BM-hMSC1 and BM-hMSC2 respectively. As expected based on previous data [44], GW9662 exposure increased ECM secretion by each hMSC preparation (**Fig11a**). OEihMSCs secreted 2-3 fold more ECM than both OEhMSCs (**Fig11a**). The protein content of the matrices was quantified and normalized to total yield (**Fig11b**). Protein content remained unchanged (~70%) in response to GW9662 which indicates that total ECM secretion is increased by GW9662. Due to the important role calcium plays in bone formation, the calcium content of the ECM was measured with the highly sensitive Arsenazo III assay which allows for the detection of trace amounts of calcium. Both OEihMSC-ECM and OEhMSC1-ECM had higher calcium levels than OEhMSC2-ECM (**Fig11c**) and phase microscopy highlighted the presence of mineralized nodules on the monolayers immediately prior to ECM extraction (**Fig11d**).

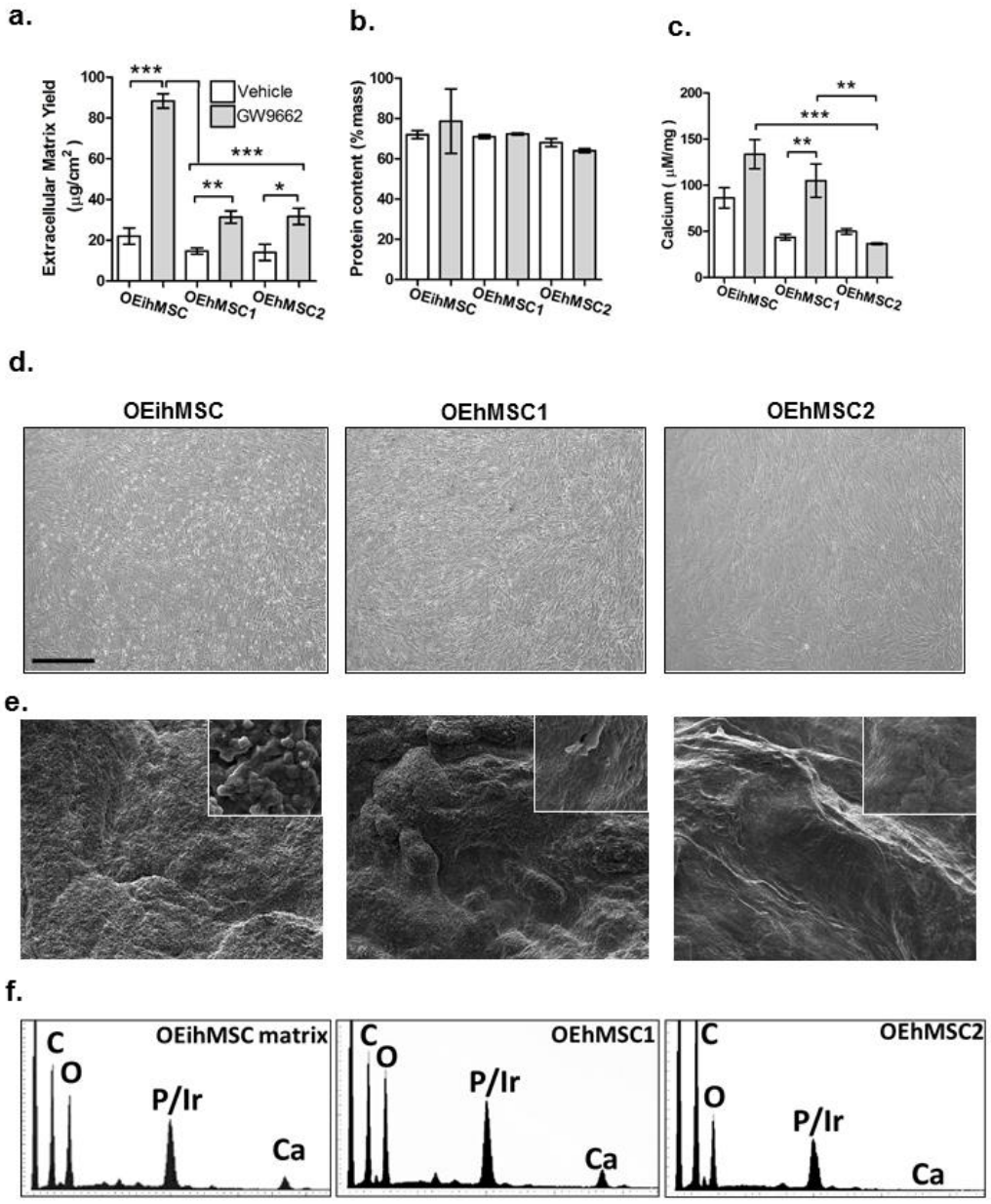

Figure 11: Partial characterization of ECM-derived from OEihMSCs and OEhMSCs.
Panel a: Total ECM yield by mass from OEihMSCs and OEhMSCs. **Panel b:** Protein content in ECM from OEihMSCs and OEhMSCs**. Panel c:** Calcium content in ECM from OEihMSCs and OEhMSCs. **Panel d:** Monolayers of OEihMSCs and OEhMSCs prior to ECM purification, *Bar* = 150μm. **Panel e:** SEM of matrices generated by OEihMSCs and OEhMSCs. **Panel f:** EDS measurements on matrices from **panel e.** Raw data provided in **Fig 12**. Iridium coating masked phosphate identification. **Statistics:** The data (n=3) are presented as means with standard deviations and were compared using ANOVA with Tukey's post test. * = P<0.05, ** = P<0.01, *** = P<0.005.

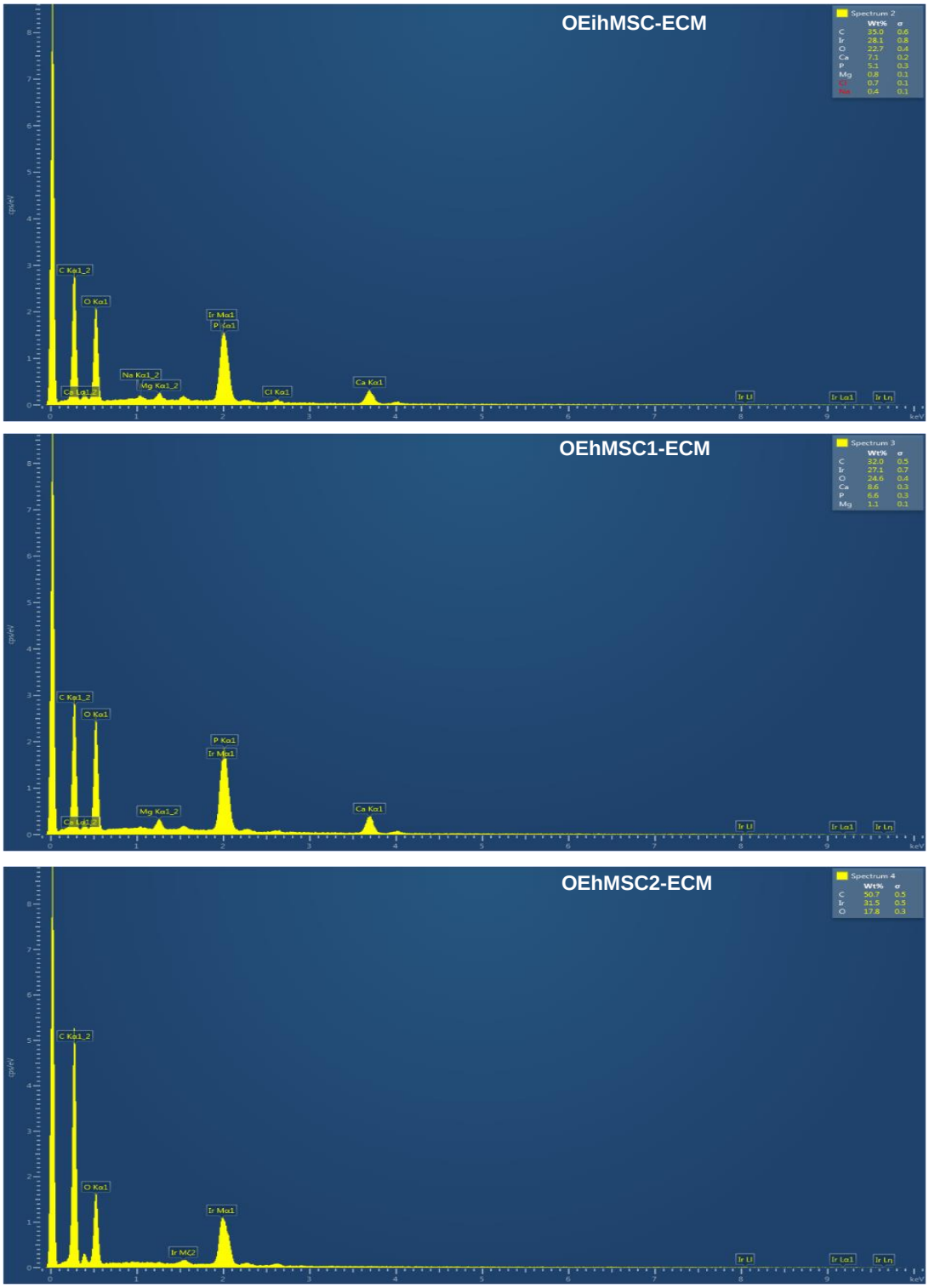

Figure 12: Raw EDS data from Figure 11.

As expected, based on their relative osteogenic properties, the OEihMSC monolayers exhibited the greatest amount of mineralized nodules, OEhMSC1 exhibited slightly fewer, while OEhMSC2 displayed very few. SEM also revealed the presence of the nodules on the processed ECM. (**Fig11e**). EDS analysis confirmed the presence of calcium in the nodules (**Fig11f, Fig12**). Calcium was not detected in OEhMSC2-ECM providing a potential explanation for the reduced osteogenic activity of the BM-hMSC2 cells. GW9662 exposure produced a modest increase in calcium in OEihMSC-ECM and a significant increase in calcium in OEhMSC1-ECM compared to their respective vehicle control-derived ECM. This tracks with previous observations that ihMSCs can mineralize in the absence of dexamethasone or GW9662 (**Fig6c**) while BM-hMSC1 requires dexamethasone (**Fig6b,c**) or GW9662 (**Fig11d**) to induce mineralization. Together, these data **s**uggest that GW9662 can induce mineralization in the absence of dexamethasone if the cells possess a baseline osteogenic capability. BM-hMSC2 exhibited the lowest capacity for osteogenesis in previous assays (**Fig6b, Fig7, Fig8**) and did not mineralize with GW9662 exposure in the absence of dexamethasone (**Fig11d**).

Proteomic analysis was carried out on ECM generated with GW9662 or vehicle-treated ihMSCs, BM-hMSC1, and BM-hMSC2. Importantly, GW9662 increased the number of shared proteins between the matrices from all three donors (**Fig13a**). This supports previous findings that osteogenic enhancement with GW9662 could be used to reduce the effects of donor variability in hMSC preparations [35].

Figure 13: ECM purified from OEihMSCs and OEhMSCs contains enriched levels of collagen VI and XII and can accelerate expression of osteogenic biomarkers by attached OEihMSCs.Panel a: Venn diagram highlighting the distributions of protein signatures detected from ECM generated by OEihMSCs and OEhMSCs with (*after arrow*) and without (*before arrow*) GW9662. Full list of proteins provided in **Tables 2&3**. **Panel b:** Hierarchical comparison of proteomic data suggests that OEihMSC-ECM clusters with OEhMSC1-ECM. **Panel c:** Immunoblotting confirms that collagens VI and XII are expressed at higher levels in ihMSCs as compared to BM-hMSC1&2. **Panel d:** Semi quantification of signal intensity from western blots presented in panel c. **Panel e:** A more sensitive proteomic analysis of OEihMCS-ECM confirms an abundance of collagen VI and collagen XII. **Panel f:** Exposure of ihMSCs to GW9662 under osteogenic conditions causes transcriptional upregulation of various collagens found in anabolic osteoid tissue, including collagens VI and XII. **Panel g:** GW9662-induced OEihMSC-ECM upregulates ALP activity in ihMSCs and promotes increased OPG secretion in ihMSCs under osteogenic conditions. **Statistics:** The data (n=3) are presented as means with standard deviations and were compared using ANOVA with Tukey's post test. * = $P<0.05$, ** = $P<0.01$, *** = $P<0.005$.

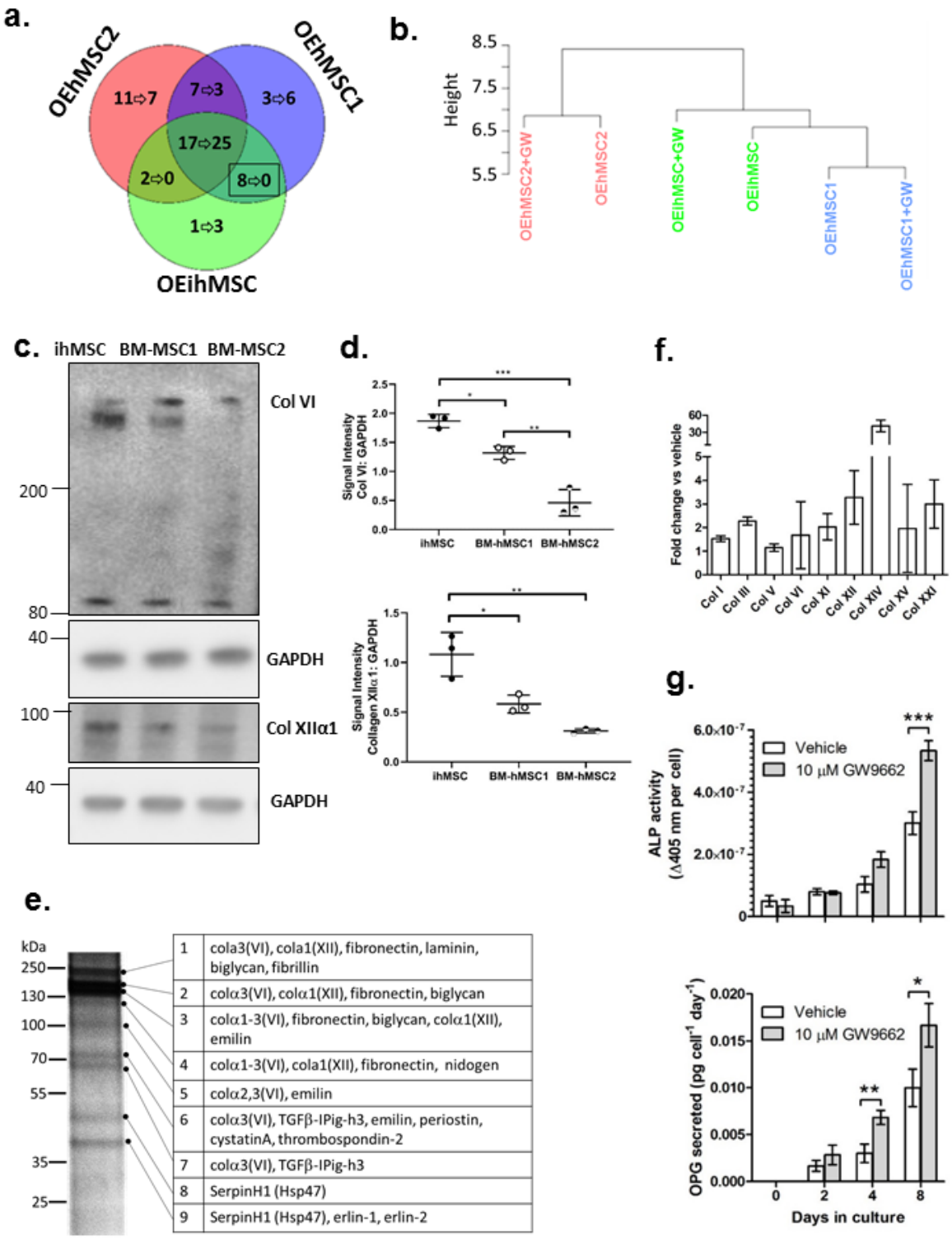
a.
OEhMSC2
OEhMSC1
OEihMSC
11⇨7
7⇨3
3⇨6
17⇨25
2⇨0
8⇨0
1⇨3
b.
Height
8.5
7.5
6.5
5.5
OEhMSC2+GW
OEhMSC2
OEihMSC+GW
OEihMSC
OEhMSC1
OEhMSC1+GW
c.
ihMSC
BM-MSC1
BM-MSC2
Col VI
200
80
40
GAPDH
100
Col XIIα1
40
GAPDH
d.
Signal Intensity Col VI: GAPDH
ihMSC
BM-hMSC1
BM-hMSC2
Signal Intensity Collagen XIIα1 : GAPDH
f.
Fold change vs vehicle
Col I
Col III
Col V
Col VI
Col XI
Col XII
Col XIV
Col XV
Col XXI
g.
ALP activity (Δ405 nm per cell)
Vehicle
10 μM GW9662
OPG secreted (pg cell-1 day-1)
Days in culture
e.
kDa
250
130
100
70
55
35
25
1 cola3(VI), cola1(XII), fibronectin, laminin, biglycan, fibrillin
2 colα3(VI), colα1(XII), fibronectin, biglycan
3 colα1-3(VI), fibronectin, biglycan, colα1(XII), emilin
4 colα1-3(VI), cola1(XII), fibronectin, nidogen
5 colα2,3(VI), emilin
6 colα3(VI), TGFβ-IPig-h3, emilin, periostin, cystatinA, thrombospondin-2
7 colα3(VI), TGFβ-IPig-h3
8 SerpinH1 (Hsp47)
9 SerpinH1 (Hsp47), erlin-1, erlin-2

When matrices from vehicle-treated cells were compared, the OEihMSC-ECM and OEhMSC1-ECM had the strongest similarity in ECM composition (**Fig13b**) which was expected given that these cells have a greater and more comparable osteogenic potential as compared to BM-hMSC2. Proteins shared exclusively between OEihMSC-ECM and OEhMSC1-ECM were focused on as OEhMSC1-ECM has previously demonstrated potent osteoinductive efficacy *in vivo* [42,43]. Due to the normalizing effect of GW9662, there were no proteins identified in OEihMSC-ECM and OEhMSC1-ECM but not in OEhMSC2-ECM, if generated in the presence of GW9662 (**Table 3**). However, 8 proteins were identified from ECM generated with the vehicle control (**Table 2**). These included Integrin β1, collagen IV α1, collagen VI α1 & α2, and collagen XII α1. These collagens are all enriched in anabolic bone and collagen VI and XII-mediated secretion of BMP-2 from hMSCs has been proposed as a contributing mechanism of bone healing by OEhMSC-ECM [42]. Immunoblotting was performed to determine the relative levels of collagens VI and XII among the three hMSC preparations (**Fig13c**). As expected, the highest expression of both collagens VI and XII were found in the ihMSCs (**Fig13d**) with the lowest levels in BM-hMSC2. Interestingly, the expression of collagens VI and XII tracks with the osteogenic potential among the three hMSC preparations highlighting their importance to osteogenesis. A further, more thorough, proteomic analysis was performed on OEihMSC-ECM after digestion by SDS-PAGE. The ECM proteins were separated by electrophoresis, excised, and analyzed individually to provide a higher resolution of the protein composition. Collagens VI and XII were identified again, along with associated proteins periostin and

TGFβ-IPig-H3 (**Fig13e**). Quantitative RT-PCR showed that number of collagen transcripts, including collagens VI and XII, were upregulated in response to GW9662 exposure when compared to the vehicle control (**Fig13f**). This indicated that GW9662 may induce an ECM capable of providing a greater osteogenic stimulus than vehicle control-treated ECM. Previously data showed that GW9662- and vehicle- induced ECM from BM-hMSCs provided a comparable osteogenic stimulus in vitro [44]. To test this with OEihMSC- ECM, GW9662 or vehicle treated-ECM was deposited on tissue culture plastic, decellularized, and re-seeded ihMSCs in the presence of an osteogenic stimulus. GW9662-treated ECM stimulated greater ALP activity and OPG secretion (**Fig13g**) indicating, for the first time, that GW9962 can alter the efficacy of the ECM along with the yield.

Table 2: Proteins shared in matrix derived from osteogenically enhanced MSCs generated in absence of GW9662 treatment.

Present in all matrices.	
ID	**Protein name**
A0A087WTA8	Collagen alpha-2(I) chain
P08123	Collagen alpha-2(I) chain (Alpha-2 type I collagen)
P05997	Collagen alpha-2(V) chain
A0A087WWY3	Filamin-A
P21333	Filamin-A (FLN-A) (Actin-binding protein 280) (ABP-280) (Alpha-filamin) (Endothelial actin-binding protein) (Filamin-1) (Non-muscle filamin)
P02452	Collagen alpha-1(I) chain (Alpha-1 type I collagen)
P12111-4	Collagen alpha-3(VI) chain
E7ENL6	Collagen alpha-3(VI) chain
O43854-2	EGF-like repeat and discoidin I-like domain-containing protein 3 (Developmentally-regulated endothelial cell locus 1 protein) (Integrin-binding protein DEL1)
Q96B60	5'-nucleotidase (5'-nucleotidase, ecto (CD73), isoform CRA_c) (NT5E protein)
O43854	EGF-like repeat and discoidin I-like domain-containing protein 3 (Developmentally-regulated endothelial cell locus 1 protein) (Integrin-binding protein DEL1)
P12111	Collagen alpha-3(VI) chain
P12111-2	Collagen alpha-3(VI) chain
P21333-2	Filamin-A (FLN-A) (Actin-binding protein 280) (ABP-280) (Alpha-filamin) (Endothelial actin-binding protein) (Filamin-1) (Non-muscle filamin)
P21589	5'-nucleotidase (5'-NT) (EC 3.1.3.5) (Ecto-5'-nucleotidase) (CD antigen CD73)
P21589-2	5'-nucleotidase (5'-NT) (EC 3.1.3.5) (Ecto-5'-nucleotidase) (CD antigen CD73)

Present in OEhMSC1 and OEhMSC2	
ID	**Protein name**
P02751-9	Fibronectin (FN) (Cold-insoluble globulin) (CIG) [Cleaved into: Anastellin; Ugl-Y1; Ugl-Y2; Ugl-Y3]
P02751-14	Fibronectin (FN) (Cold-insoluble globulin) (CIG) [Cleaved into: Anastellin; Ugl-Y1; Ugl-Y2; Ugl-Y3]
P02751-4	Fibronectin (FN) (Cold-insoluble globulin) (CIG) [Cleaved into: Anastellin; Ugl-Y1; Ugl-Y2; Ugl-Y3]
P02751-10	Fibronectin (FN) (Cold-insoluble globulin) (CIG) [Cleaved into: Anastellin; Ugl-Y1; Ugl-Y2; Ugl-Y3]
P02751-13	Fibronectin (FN) (Cold-insoluble globulin) (CIG) [Cleaved into: Anastellin; Ugl-Y1; Ugl-Y2; Ugl-Y3]
P02751-8	Fibronectin (FN) (Cold-insoluble globulin) (CIG) [Cleaved into: Anastellin; Ugl-Y1; Ugl-Y2; Ugl-Y3]
P02751-3	Fibronectin (FN) (Cold-insoluble globulin) (CIG) [Cleaved into: Anastellin; Ugl-Y1; Ugl-Y2; Ugl-Y3]

Present in OEhMSC2 and OEihMSC	
ID	**Protein name**
G5E971	Matrix metallopeptidase 13 (Collagenase 3)
P45452	Collagenase 3 (EC 3.4.24.-) (Matrix metalloproteinase-13) (MMP-13)

Present in OEhMSC1 and OEihMSC	
ID	**Protein name**
P05556-3	Integrin beta-1 (Fibronectin receptor subunit beta) (Glycoprotein IIa) (GPIIA) (VLA-4 subunit beta) (CD antigen CD29)
P12110-2	Collagen alpha-2(VI) chain
A0A087X0S5	Collagen alpha-1(VI) chain
P05556-2	Integrin beta-1 (Fibronectin receptor subunit beta) (Glycoprotein IIa) (GPIIA) (VLA-4 subunit beta) (CD antigen CD29)
P05556-4	Integrin beta-1 (Fibronectin receptor subunit beta) (Glycoprotein IIa) (GPIIA) (VLA-4 subunit beta) (CD antigen CD29)
Q99715-2	Collagen alpha-1(XII) chain
P12109	Collagen alpha-1(VI) chain
P29400	Collagen alpha-5(IV) chain

Table 3: Proteins shared in matrix derived from osteogenically enhanced MSCs generated with GW9662 treatment.

Present in all matrices.	
ID	**Protein name**
A0A087WTA8	Collagen alpha-2(I) chain (Alpha-2 type I collagen)
P08123	Collagen alpha-2(I) chain (Alpha-2 type I collagen)
P02751-9	Fibronectin (FN) (Cold-insoluble globulin) (CIG) [Cleaved into: Anastellin; Ugl-Y1; Ugl-Y2; Ugl-Y3]
P05997	Collagen alpha-2(V) chain
P02458	Collagen alpha-1(II) chain (Alpha-1 type II collagen) [Cleaved into: Collagen alpha-1(II) chain; Chondrocalcin]
P02751-14	Fibronectin (FN) (Cold-insoluble globulin) (CIG) [Cleaved into: Anastellin; Ugl-Y1; Ugl-Y2; Ugl-Y3]
P02452	Collagen alpha-1(I) chain (Alpha-1 type I collagen)
P12111-4	Collagen alpha-3(VI) chain
E7ENL6	Collagen alpha-3(VI) chain
P05556-3	Integrin beta-1 (Fibronectin receptor subunit beta) (Glycoprotein IIa) (GPIIA) (VLA-4 subunit beta) (CD antigen CD29)
P02751-4	Fibronectin (FN) (Cold-insoluble globulin) (CIG) [Cleaved into: Anastellin; Ugl-Y1; Ugl-Y2; Ugl-Y3]
P12110-2	Collagen alpha-2(VI) chain
A0A087X0S5	Collagen alpha-1(VI) chain
P12111	Collagen alpha-3(VI) chain
P12111-2	Collagen alpha-3(VI) chain
P05556-2	Integrin beta-1 (Fibronectin receptor subunit beta) (Glycoprotein IIa) (GPIIA) (VLA-4 subunit beta) (CD antigen CD29)
P05556-4	Integrin beta-1 (Fibronectin receptor subunit beta) (Glycoprotein IIa) (GPIIA) (VLA-4 subunit beta) (CD antigen CD29)
P12109	Collagen alpha-1(VI) chain
P02751-10	Fibronectin (FN) (Cold-insoluble globulin) (CIG) [Cleaved into: Anastellin; Ugl-Y1; Ugl-Y2; Ugl-Y3]
P02751-13	Fibronectin (FN) (Cold-insoluble globulin) (CIG) [Cleaved into: Anastellin; Ugl-Y1; Ugl-Y2; Ugl-Y3]
P02751-8	Fibronectin (FN) (Cold-insoluble globulin) (CIG) [Cleaved into: Anastellin; Ugl-Y1; Ugl-Y2; Ugl-Y3]
P02751-3	Fibronectin (FN) (Cold-insoluble globulin) (CIG) [Cleaved into: Anastellin; Ugl-Y1; Ugl-Y2; Ugl-Y3]
P21589	5'-nucleotidase (5'-NT) (EC 3.1.3.5) (Ecto-5'-nucleotidase) (CD antigen CD73)
P21589-2	5'-nucleotidase (5'-NT) (EC 3.1.3.5) (Ecto-5'-nucleotidase) (CD antigen CD73)
P35555	Fibrillin-1 [Cleaved into: Asprosin]

Present in OEhMSC1 and OEhMSC2	
ID	**Protein name**
O43854-2	EGF-like repeat and discoidin I-like domain-containing protein 3 (Developmentally-regulated endothelial cell locus 1 protein) (Integrin-binding protein DEL1)
Q96B60	5'-nucleotidase (5'-nucleotidase, ecto (CD73), isoform CRA_c) (NT5E protein)
O43854	EGF-like repeat and discoidin I-like domain-containing protein 3 (Developmentally-regulated endothelial cell locus 1 protein) (Integrin-binding protein DEL1)

Osteoregenerative capacity of OEihMSC-ECM

It was previously demonstrated that OEhMSC-ECM improves osteoregeneration by both OEhMSCs and hBM [42-44]. To test whether OEihMSC-ECM possessed equivalent osteogenic properties, OEihMSCs or hBM were co-administered with OEihMSC-ECM in a calvarial defect model to assess osteoregenerative potential *in vivo*. OEihMSCs were also administered alone and on gelatin foam (GF, Gelfoam) and hBM was administered on GF. Negative controls received no treatment while a clinical dose (0.1mg/mL) of BMP-2 with GF served as the positive control [87]. BMP-2 with GF induced a modest amount of bone growth that was significantly higher than the negative controls (**Fig14, Fig16c, Table4**). Histology highlighted the presence of immature bone within the defect (**Fig 16b**). MicroCT indicated that OEihMSCs with GF exhibited a similar response to BMP-2 although histological analysis revealed that the OEihMSCs promoted a higher amount of immature bone (**Fig14, Fig15d, Table4**), although this was not detectable on the μCT. All groups receiving OEihMSC-ECM exhibited a remarkable level of bone growth. The healing index (HI) was greater than 1 in all but 2 cases (**Fig15d, Table4**). HI was calculated by expressing the volume of new bone within the defect after 4 weeks as a ratio of an equal volume of interest on the uninjured contralateral side of the calvaria. Surprisingly, OEihMSC-ECM without the addition of cells promoted the greatest degree of bone growth (HI 2-3) (**Fig15a-d**). Previously OEhMSC-ECM had not exhibited intrinsic osteogenic efficacy without the addition of osteoprogenitors [42-44].

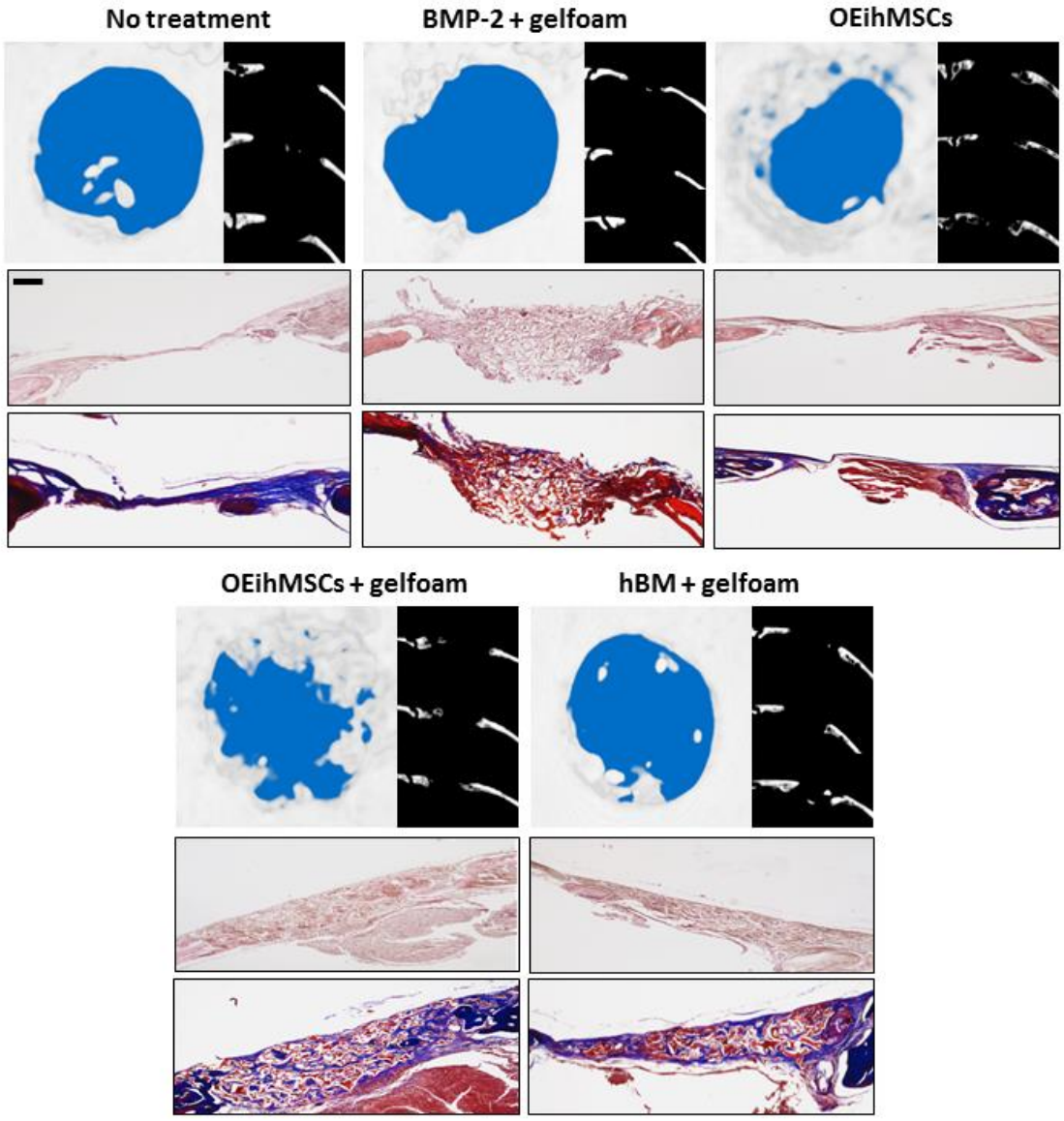

Figure 14: OEihMSCs possess a comparable osteoregenerative capacity to BMP-2.
Immune-compromised nude mice received a 3mm diameter, full thickness circular calvarial defect. Defects received no treatment, BMP-2+gelfoam, OEihMSCs, OEihMSCs+gelfoam, or hBM+gelfoam. Mice were euthanized after 4 weeks and calvarial ones were excised for analysis. µCT reconstructions (*upper, left*), axial cross-sections (*upper, right*), Hematoxylin and eosin stained sections (*middle, bar* = 250µm), and Masson's trichrome stained sections (*lower)*

Both H&E and Masson's trichrome staining confirmed that mature bone was present in the defects that received OEihMSC-ECM (**Fig15b,c**) and revealed that it exhibited a trabecular-like architecture, a feature previously unseen with bone healing by OEhMSC-ECM [44]. Bone formed in the presence of OEihMSC-ECM was more compact (**Fig15e, Table5**) but there was no difference in bone mineral density (**Fig15f**) between groups. Tartrate resistant acid phosphatase (TRAP) staining for osteoclast activity was carried out to determine a potential cause of the enhanced bone healing without the addition of osteoprogenitors. The level of osteoclast activity correlated with the degree of bone healing, with OEihMSC-ECM exhibiting the highest activity (**Fig16**). The results suggest that due to their high osteogenic potential, including with high expression of collagens VI and XII, ihMSCs secrete a highly osteogenic ECM, whose osteogenic properties can be further enhanced by GW9662 exposure. The increased osteogenic signal provided by this ECM is sufficient to promote bone healing *in vivo* without the need for exogenous osteoprogenitors.

Figure 15: OEihMSC-ECM exhibits enhanced osteoregenerative capacity in the presence or absence of exogenously added osteoprogenitor cells. Immune-compromised nude mice received a 3mm diameter, full thickness circular calvarial defect. Defects were treated with OEihMSC-ECM alone or in the presence of OEihMSCs or hBM. Mice were euthanized after 4 weeks and the calvarial bones were dissected out for analysis. **Panel a:** µCT reconstructions (*left*) and axial reconstructions (*right*). **Panel b:** Hematoxylin and eosin stained sections at low (*above, bar* = 250µm) and high (*below, bar* = 75µm) power. **Panel c:** Masson's trichrome stained sections of calvarial defects at low (*above, bar* = 250µm) and high (*below, bar* = 75µm). **Panel d:** Healing indices of calvarial defects. Statistical comparisons of OEihMSC-ECM groups compared to controls are annotated **a-e** and cross-comparisons between OEihMSC-ECM groups are denoted by lines and asterisks. **Panel e:** Surface to volume ratio. **Panel f:** Bone mineral density. **Statistics:** The data are presented as means with standard deviations and were compared using ANOVA with Tukey's post test. For all groups n = 5 except. ihM + hBM n = 4, ihM + OEihMSCs n=6, and BMP-2 n=10. * = $P<0.05$, ** = $P<0.01$, *** = $P<0.005$.

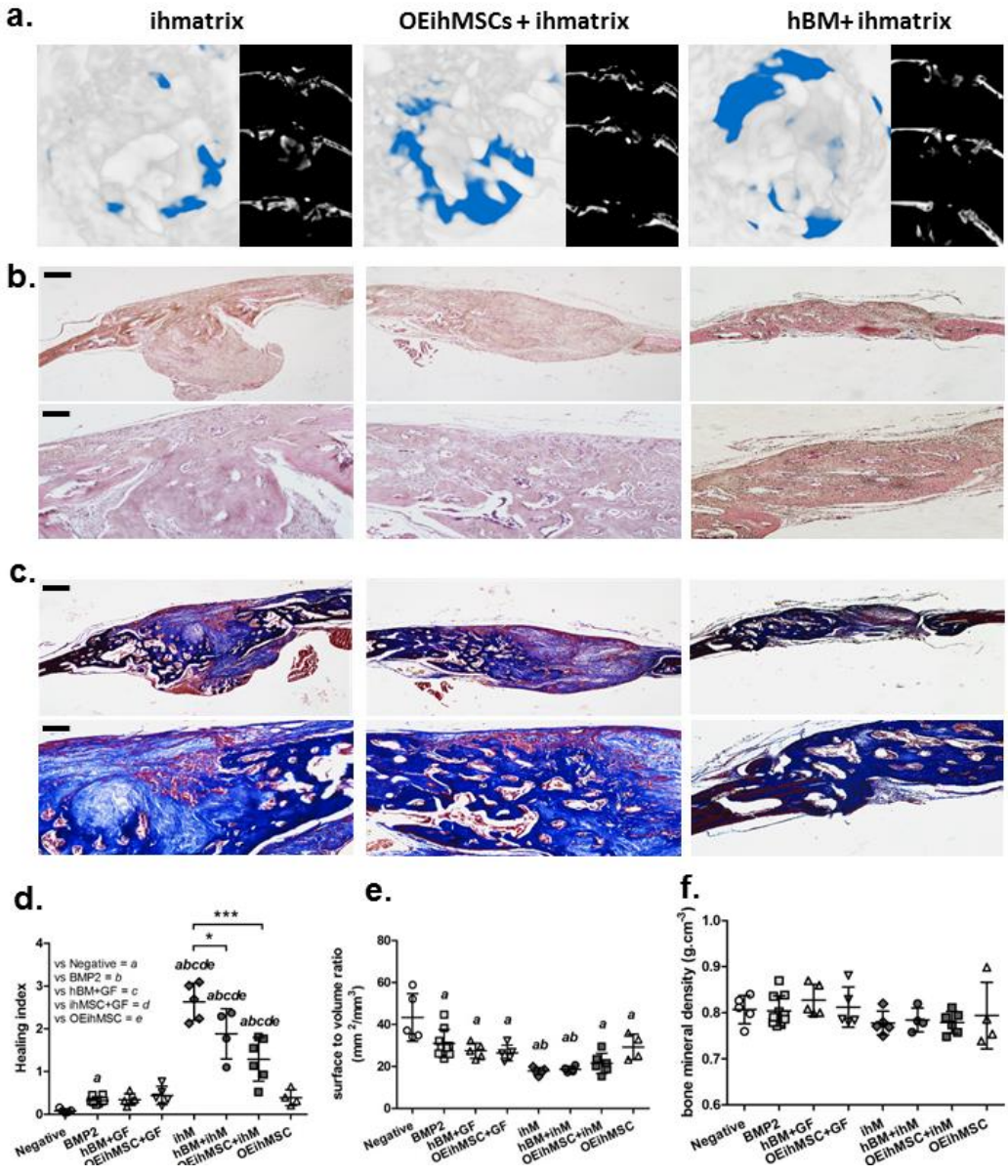
a.
ihmatrix
OEihMSCs + ihmatrix
hBM+ ihmatrix
b.
c.
d.
Healing index
vs Negative = a
vs BMP2 = b
vs hBM+GF = c
vs ihMSC+GF = d
vs OEihMSC = e
abcde
Negative
BMP2
hBM+GF
OEihMSC+GF
ihM
hBM+ihM
OEihMSC+ihM
OEihMSC
e.
surface to volume ratio
f.
bone mineral density (g.cm-3)

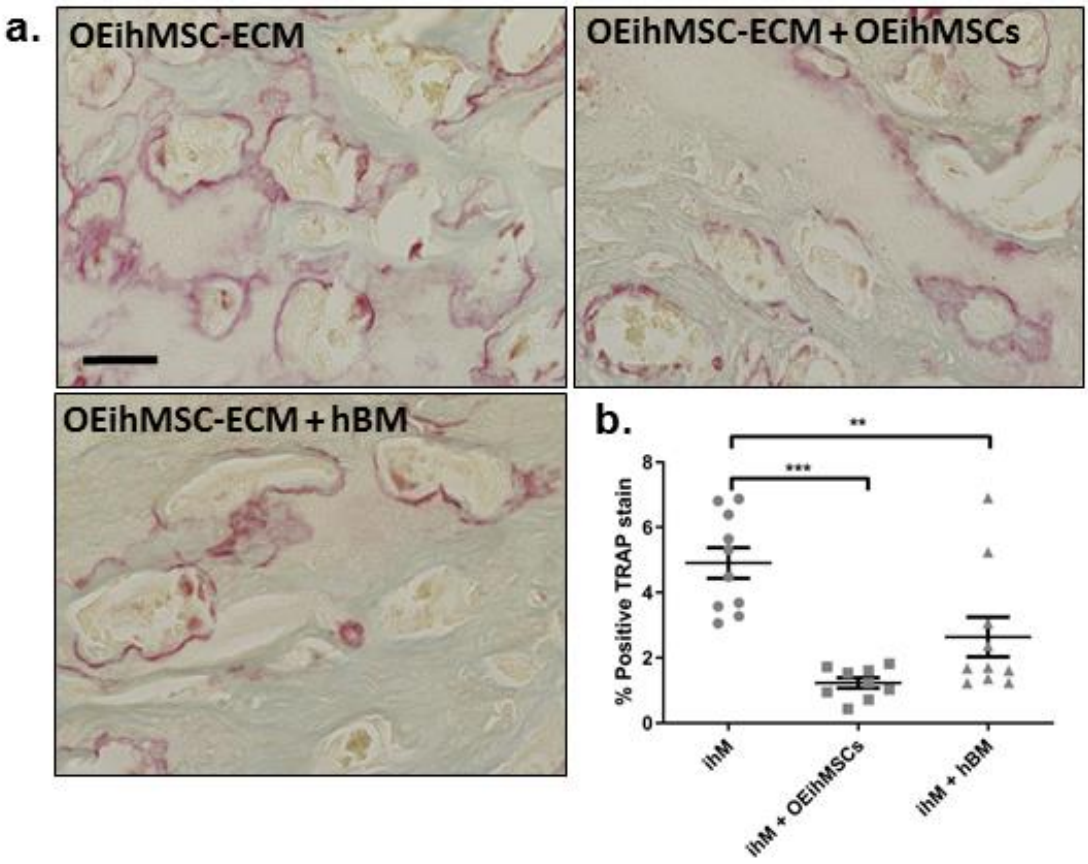

<u>Figure 16: OEihMSC-ECM alone exhibits the highest level of osteoclast activity.</u> Panel a: TRAP staining (*red*) for osteoclast activity within healed defects with OEihMSC-ECM (*bar* = 50μm). **Panel b:** Quantification of TRAP staining from randomly acquired images taken from the center of each defect (*ihM denotes OEihMSC-ECM).* **Statistics:** The data were compared using ANOVA with Tukey's post test, ** = P<0.01, *** = P<0.005.

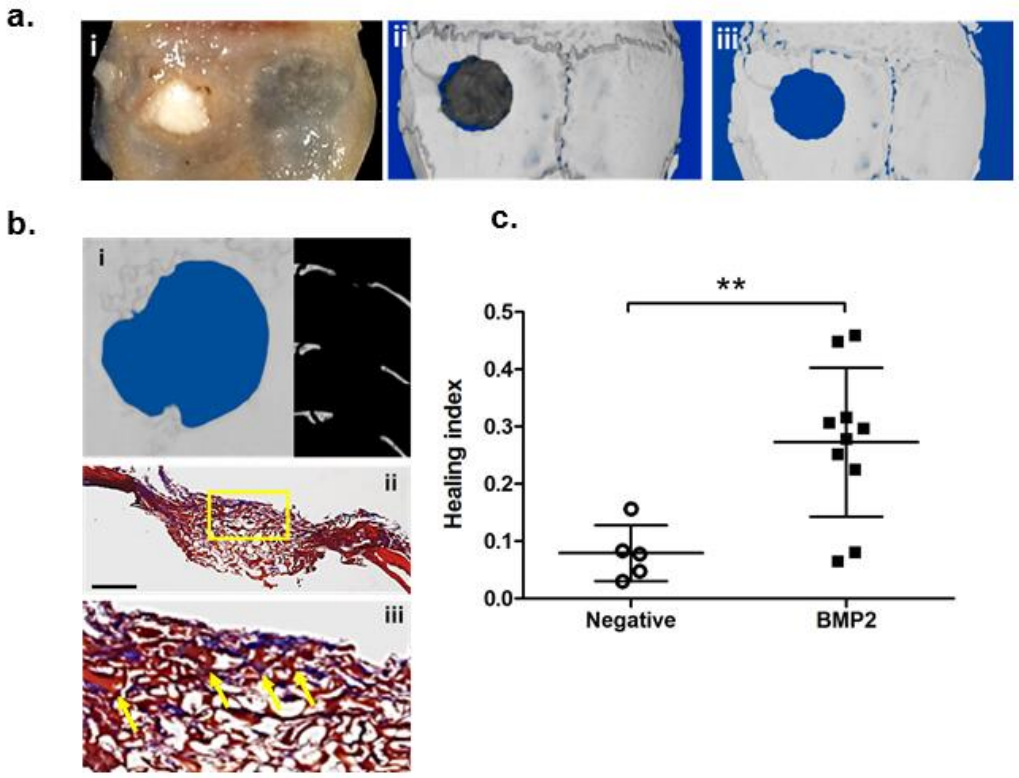

Figure 17 Controls for *in vivo* experiments presented in figures 14 & 15. Panel a: Photograph of OEihMSC within the calvarial defect after 4 weeks of healing (**i**). 3D rendering generated from µCT data showing OEihMSC-ECM (*grey*) at the defect site (**ii**). 3D rendering with threshold applied to remove OEihMSC-ECM and detect bone only (*white*) (**iii**). **Panel b:** Modified scan thresholding reveals BMP2 mediated deposition of immature bone tissue. (i) □CT reconstruction (*above left*), axial cross-sections (*above right*), (ii) Masson's trichrome stained sections after 4 weeks of healing (bar = 250 □m), (iii) magnified image of region in ii (*yellow box*) revealing diffuse areas of bone deposition (*arrowed*). **Panel c:** Healing indices calculated with modified thresholding to detect primitive osteoid demonstrate presence in some of the specimens treated with BMP2. The data were compared using one-tailed Student's t-test. * = $P<0.05$.

Table 4: P-values and confidence intervals for calvarial defect HI measurements. *P<0.05, ** P<0.01, ***P<0.005, ns not significant (P>0.05).

Tukey's Multiple Comparison Test	P < 0.05?	Summary	95% CI of diff
Negative vs BMP-2	Yes	*	-0.8362 to 0.3482
Negative vs hBM+GF	No	ns	-0.9208 to 0.3933
Negative vs OEihMSC+GF	No	ns	-1.019 to 0.2954
Negative vs ihM	Yes	***	-3.206 to -1.892
Negative vs hBM+ihM	Yes	***	-2.498 to -1.104
Negative vs OEihMSC+ihM	Yes	***	-1.834 to -0.5755
Negative vs OEihMSC	No	ns	-1.006 to 0.3873
BMP-2 vs hBM+GF	No	ns	-0.6120 to 0.5725
BMP-2 vs OEihMSC+GF	No	ns	-0.7099 to 0.4746
BMP-2 vs ihM	Yes	***	-2.897 to -1.713
BMP-2 vs hBM+ihM	Yes	***	-2.193 to -0.9210
BMP-2 vs OEihMSC+ihM	Yes	***	-1.522 to -0.3995
BMP-2 vs OEihMSC	No	ns	-0.7018 to 0.5706
hBM+GF vs OEihMSC+GF	No	ns	-0.7549 to 0.5591
hBM+GF vs ihM	Yes	***	-2.942 to -1.628
hBM+GF vs hBM+ihM	Yes	***	-2.234 to -0.8406
hBM+GF vs OEihMSC+ihM	Yes	***	-1.570 to -0.3118
hBM+GF vs OEihMSC	No	ns	-0.7427 to 0.6510
OEihMSC+GF vs ihM	Yes	***	-2.844 to -1.530
OEihMSC+GF vs hBM+ihM	Yes	***	-2.136 to -0.7427
OEihMSC+GF vs OEihMSC+ihM	Yes	**	-1.472 to -0.2139
OEihMSC+GF vs OEihMSC	No	ns	-0.6448 to 0.7489
ihM vs hBM+ihM	Yes	*	0.05095 to 1.445
ihM vs OEihMSC+ihM	Yes	***	0.7154 to 1.974
ihM vs OEihMSC	Yes	***	1.543 to 2.936
hBM+ihM vs OEihMSC+ihM	No	ns	-0.07391 to 1.267
hBM+ihM vs OEihMSC	Yes	***	0.7570 to 2.226
OEihMSC+ihM vs OEihMSC	Yes	**	0.2244 to 1.566

Table 5: P-values and confidence intervals for calvarial defect surface to volume ratios. *P<0.05, ** P<0.01, ***P<0.005, ns not significant (P>0.05).

Tukey's Multiple Comparison Test	P < 0.05?	Summary	95% CI of diff
Negative vs BMP-2	Yes	*	1.785 to 23.05
Negative vs hBM+GF	Yes	**	3.843 to 27.96
Negative vs OEihMSC+GF	Yes	**	4.910 to 29.02
Negative vs ihM	Yes	***	13.53 to 37.64
Negative vs hBM+ihM	Yes	***	11.97 to 37.54
Negative vs OEihMSC+ihM	Yes	***	10.37 to 33.46
Negative vs OEihMSC	Yes	*	1.352 to 26.93
BMP-2 vs hBM+GF	No	ns	-7.151 to 14.11
BMP-2 vs OEihMSC+GF	No	ns	-6.083 to 15.18
BMP-2 vs ihM	Yes	**	2.533 to 23.80
BMP-2 vs hBM+ihM	Yes	*	0.8826 to 23.79
BMP-2 vs OEihMSC+ihM	No	ns	-0.5488 to 19.54
BMP-2 vs OEihMSC	No	ns	-9.733 to 13.18
hBM+GF vs OEihMSC+GF	No	ns	-10.99 to 13.12
hBM+GF vs ihM	No	ns	-2.372 to 21.74
hBM+GF vs hBM+ihM	No	ns	-3.932 to 21.64
hBM+GF vs OEihMSC+ihM	No	ns	-5.527 to 17.56
hBM+GF vs OEihMSC	No	ns	-14.55 to 11.03
OEihMSC+GF vs ihM	No	ns	-3.440 to 20.67
OEihMSC+GF vs hBM+ihM	No	ns	-4.999 to 20.58
OEihMSC+GF vs OEihMSC+ihM	No	ns	-6.594 to 16.49
OEihMSC+GF vs OEihMSC	No	ns	-15.61 to 9.960
ihM vs hBM+ihM	No	ns	-13.62 to 11.96
ihM vs OEihMSC+ihM	No	ns	-15.21 to 7.875
ihM vs OEihMSC	No	ns	-24.23 to 1.344
hBM+ihM vs OEihMSC+ihM	No	ns	-15.14 to 9.465
hBM+ihM vs OEihMSC	No	ns	-24.09 to 2.863
OEihMSC+ihM vs OEihMSC	No	ns	-20.08 to 4.529

Discussion

Current therapeutic approaches for bone repair have significant disadvantages. Demineralized bone (DBM) and allografts suffer from batch variation and the risk of pathogen transmission [95,96]. Synthetic products, such as tricalcium phosphate, are cost-effective but suffer from poor biocompatibility and cytotoxicity issues [97]. BMP-2 is highly osteoinductive, but when used incorrectly can result in potentially life-threatening side effects such as ectopic bone formation, radiculopathy, and inflammation [98]. An autologous bone graft remains the gold standard approach, but suffers from limited availability and donor site morbidity [95,99].

The potent osteogenic capacity of hMSCs make them a promising candidate to provide an alternative therapeutic approach to autologous bone graft. However, as with DBM, donor-derived materials suffer from batch variation and the potential for pathogen transfer [95,96]. The use of iPSCs as a donor-free, theoretically infinite source of hMSCs could circumvent these issues by providing a genetically identical source of cells [81].

Unlike iPSCs, the ihMSCs exhibited proliferative senescence (**Fig4b-e**), and possess a morphology and immunophenotype similar to hMSCs (**Fig5a, Fig5b**) [25]. Trilineage differentiation potential was confirmed, albeit with low adipogenic capacity (**Fig6**). The ihMSCs demonstrated an increased capacity for osteogenic differentiation, and were capable of mineralizing in conditions that lacked dexamethasone, which is required for BM-hMSCs (**Fig6c**) [73]. The phenotype of ihMSCs differs greatly in the literature with retention of proliferative immortality, a lack of expression of BM-hMSC markers, and variable multipotency reported [100-103]. This is likely due to the variation of

donor tissue and reprogramming and differentiation protocols. Interestingly, a high osteogenic potential coupled with low adipogenic has been reported in multiple studies, similar to the observations in this study, although the reason for this phenomenon is unclear [81,103,104].

In BM-hMSCs, homeostasis between the adipogenic and osteogenic axes is regulated by the inhibitory relationship driven by PPARγ-mediated degradation of β-catenin and the cWnt-mediated inhibition of PPARγ expression [105]. As with BM-hMSCs, ihMSCs upregulate cWnt signaling in response to an osteogenic stimulus, resulting in inhibition of the adipogenic axis and the stimulation of osteogenic biomarkers (**Fig9, Fig10**). Like BM-hMSCs, ihMSCs can be osteogenically enhanced by inhibiting PPARγ with GW9662, resulting in further upregulation of cWnt signaling and concomitant osteogenesis (**Fig9c,d & Fig10**) [35,44]. Combined with the observation that β-catenin inhibition upregulates adipogenic differentiation in ihMSCs (**Fig6d**), the homeostatic relationship between the osteogenic and adipogenic axes driven by cWnt and PPARγ is present in ihMSCs.

GW9662 exposure under osteogenic conditions induces an OEihMSC phenotype accompanied by the secretion of a dense ECM, which stimulated osteogenesis of attached ihMSCs (**Fig11a,g**). The secreted ECM is rich in calcified nodules and the osteogenic collagens VI and XII. Both collagens VI and XII are enriched in embryonic osteoid[106,107] and regulate morphology and polarity of osteoblasts in developing mice [69,70]. Immune-blockade of collagens VI and XII resulted in a reduction of BMP-2 and

OPG secretion from attached hMSCs, indicating that both collagens are capable of providing an osteogenic signal [42].

Previously we have shown that ECM secreted by OEhMSCs promotes osteogenesis of attached OEhMSCs by supporting cell attachment, survival, and the secretion of osteogenic factors [42,44,108]. A remarkable level of healing was observed after 4 weeks when OEihMSC was co-adminstered with OEihMSCs or hBM (**Fig15, Table4**). The level of healing was significantly higher than in the BMP-2 group. Surprisingly, the greatest level of healing was observed with OEihMSC-ECM in the absence of OEihMSCs or hBM. In previous studies, OEhMSC-ECM exhibited limited intrinsic efficacy without co-adminstered progenitor cells [42,44].

Despite being administered at an active dose, BMP-2 promoted a modest, variable response [87]. This may have been due to the short duration of the assay (**Fig14, Fig15a, Fig17b,c, Table4**). Most calvarial defects are performed for a longer duration, with BMP-2 stimulating robust bone formation [109]. Immature osteoid is difficult to detect radiologically, which may account for these observations [110]. Histological analysis confirmed the presence of diffuse clusters of immature bone in the BMP-2 defects. (**Fig17b**).

Co-administering OEihMSC-ECM with OEihMSCs or hBM reduced the degree of bone healing (**Fig15**). While the cause of this observation is unclear, TRAP staining highlighted that osteoclast activity correlated with the level of bone healing (**Fig16**), with the highest osteoclast activity observed with OEihMSC-ECM alone. It is possible that the addition vast numbers of osteoblast progenitors could disrupt bone

homeostasis[111]. As mentioned in Chapter I (**Fig1**), upregulation of OPG secretion by osteoblasts signals the end of the resorption phase of bone remodeling, by shifting the ratio of OPG to RANKL in favor of osteoclast inhibition [15]. OEihMSCs are highly osteogenic, and present in higher numbers than osteoprogenitors in the hBM, and are therefore likely to secrete high levels of OPG into the defect. While higher levels of osteoclast activity may seem counter intuitive to bone healing, bone resorption is required to promote bone formation and maintain homeostasis[13]. It has also been reported that co-cultures of osteoblasts and osteoclasts produced higher amounts of bone-like tissue than osteoblasts alone *in vitro* [111], suggesting that adequate osteoclast activity is required to promote bone healing. The results suggest that OEihMSC-ECM alone may more accurately recapitulate the osteogenic microenvironment than OEhMSC-ECM used in previous studies [44], capable of inducing rapid bone healing in the absence of exogenous osteoprogenitors.

The data demonstrate that OEihMSC-ECM exhibits a level of efficacy that challenges current bone repair therapies. OEihMSC-ECM is unlikely to migrate from the site of administration (1/15) and does not appear to stimulate the release of supraphysiological levels of bioactive factors leading to the formation of ectopic bone. Furthermore OEihMSC-ECM does not contain cells, pathogens, antigens, or nucleic acids. It is a malleable, putty-like material that could be fitted into defects of various shapes or sizes. These data suggest that OEihMSC-ECM could provide a safe, translatable alternative to current approaches for bone repair. OEihMSC-ECM could be used as a scaffold to replace the need for autologous bone graft or donor cells.

CHAPTER III

THREE-DIMENSIONAL *IN VITRO* MODELING OF MALIGNANT BONE DISEASE RECAPITULATES EXPERIMENTALLY ACCESSIBLE MECHANISMS OF OSTEOINHIBITION*

Introduction

A diagnoses of malignant bone disease (MBD) usually signifies a terminal cancer [112]. It is characterized by the formation of osteolytic lesions (OLs), tumor-filled cavities resulting from disrupted bone homeostasis [49]. OLs cause pain, increased risk of fractures, and most importantly, the ideal microenvironment for tumor growth [50]. OLs increase the probability of a tumor resisting chemotherapy, ultimately reducing the likelihood of survival. As almost 40% of new cancer diagnoses in the US each year will involve bone, treating MBD is vital [113].

Current treatments are directed at eliminating tumors and preventing relapse [50,114]. Unfortunately, relapse and the development of drug resistant tumors are common due to the chemotherapy-resistant microenvironment provided by the OLs. Future treatments need to incorporate OL repair to prevent tumor recurrence. Therefore, a deeper understanding of MBD progression and the formation of OLs is required. The cWnt signaling pathway drives osteogenesis by hMSCs and osteolytic tumors can inhibit

* Reprinted with permission from "Three-dimensional in vitro modeling of malignant bone disease recapitulates experimentally accessible mechanisms of osteoinhibition" by McNeill *et al*, 2018. Cell Death and Disease, Volume 9 Issue 12, Copyright [2018] by The Authors.

cWnt signaling by secreting a number of Wnt inhibitors [115]. Dkk-1 is the most common of these Wnt inhibitors and has been linked to myeloma, osteosarcoma, and breast/prostate metastases [116-118]. Dkk-1 can bind to LRP5 and LRP6 in the presence of Kremen forming a complex that internalizes LRP5/6 [119] , preventing the formation of the Wnt, FZD, LRP5/6 complex and its' downstream signaling [120]. The inhibition if cWnt signaling in hMSCs prevents their differentiation to osteoblasts, resulting in disrupted homeostasis in favor of catabolism. In turn, poorly differentiated MSCs secrete survival factors for tumors and activation factors for osteoclasts [121,122].

Although this mechanism of osteoinhibition is well established, a therapeutic approach that re-initiates OL repair has not been developed. Current tools to study bone-tumor interactions are limited to tissue culture and animal models. Tissue culture is generally carried out on monolayers, which does not accurately represent the complex three dimensional (3D) relationship between tumors and patient tissues. As a result, assays performed on monolayers often overestimate drug responses [123,124]. Animal models provide ethical concerns, can be difficult to perform and difficult to reproduce. A 3D cell culture system that mimics the bone-tumor microenvironment could provide an alternative platform to study bone-tumor interactions [123].

Rotating wall vessel (RWV) bioreactors were used to develop this platform as they facilitate superior 3D growth of tissue-like structures as compared to conventional bioreactors [125,126]. Conventional bioreactors limit 3D constructs to approximately 1mm in diameter while constructs of greater that 3 mm in diameter have been observed in RWV bioreactors [127]. These larger constructs are facilitated by the improved fluid and

gas exchange coupled with negligible shear stress in the RWV bioreactor [128]. BM-hMSC1 (from Chapter II) was chosen to generate OEhMSCs and ECM to represent bone in this platform by mimic the osteogenic microenvironment. ECM was coated onto spherical microcarriers for use in the RWV bioreactor. A murine osteosarcoma (OS) cell line that expresses human Dkk-1 (MOSJ-Dkk1) was chosen to represent MBD. Co-culture of OEhMSCs with MOSJ-Dkk1 on ECM-coated microcarriers allowed for the detection of two distinct mechanisms of osteoinhibition; reduced cWnt signaling via the secretion of Dkk-1 from OS cells and migration of OS cells to OEhMSCs, resulting in OEhMSC displacement from the bone-tumor microenvironment. By focusing on an established mechanism of osteoinhibition, the validity of using this platform to study other aspects of MBD that are not readily measured with monolayer culture or animal models.

Materials and Methods

Monolayer tissue culture

The hMSCs were acquired from the Texas A & M Health Science Center Institute for Regenerative Medicine Mesenchymal Stem Cell distribution facility in accordance with institutionally approved protocols. The hMSCs were cultured in complete culture medium (CCM) which consisted of α-MEM (Life Technologies, Carlsbad, CA), 20% (v/v) FBS (Atlanta Biologicals, Norcross, GA), 2 mM L-glutamine (Life Technologies, Carlsbad, CA), 100 U/mL penicillin, and 100 µg/mL streptomycin (Life Technologies, Carlsbad, CA). Medium was changed every 2 days. For expansion and storage, hMSCs were recovered using trypsin-EDTA (Life Technologies, Carlsbad, CA) when density had reached about 70%-80%. After detachment, hMSCs were either reseeded at 100 cells per cm^2 or cryopreserved in α-MEM supplemented with 50% (v/v) FBS (Atlanta biologicals, Norcross, GA) and 5% (v/v) DMSO (Hybrimax, Sigma-Aldrich, St. Louis, MO) in the vapor phase of liquid nitrogen. The hMSCs were labeled with enhanced green fluorescent protein (eGFP) by lentiviral transduction with the construct that drives GFP cDNA under the constitutive chicken actin promoter pWPT-GFP (Trono Laboratory). A MoFlo XDP fluorescence activated cell sorter (Beckman Coulter, Brea, CA) was used to generate a cell bank with >99% purity. Green fluorescent protein (GFP)-positive hMSCs at passage 5 were used for the experiments. MOSJ cells were modified with constructs encoding Dkk-1 and dsRed2 fluorescent protein as previously described [129]. Control MOSJ cells were also generated that were dsRed2

labeled, but harbored only the vector backbone (MOSJ-pLenti). Phase contrast and fluorescence microscopy of live cell cultures was carried out using an inverted microscope (Nikon Eclipse TE200) fitted with a Nikon DXM1200F digital camera. : A Live/Dead Cell Imaging Kit (Life Technologies, Carlsbad, CA) was employed to assess the viability of both the hMSCs and MOSJ cells on the microcarriers. The assay was carried out according to the manufacturer's instructions with the exception of the use of Hoescht dye (Sigma-Aldrich, St. Louis, MO) to visualize dead MOSJ cells as it was not possible to distinguish between the propidium iodide stain and the dsRed2 already expressed by the cells. Live staining was carried out on hMSCs not expressing GFP to allow visualization of the calcein AM dye that indicates live cells.

Osteogenic, adipogenic, and chondrogenic potential of the GFP-labeled hMSCs were confirmed as described in Chapter II.

3D tissue culture

Prior to loading in the RWV bioreactors, the cells were expanded by conventional low-density monolayer cell culture to obtain the required numbers. To load the microcarriers, collagen I- or ECM-coated microcarriers with a combined growth area of 50 cm^2 and $2x10^6$ GFP-labeled hMSCs were incubated in a square, 100 cm^2 low-adherent polystyrene plate at 37ºC for 2 hours in 10 mL CCM with orbital shaking at 30 rpm. The microcarriers were recovered by centrifugation at 50 x g for 30 seconds then washed twice with PBS to remove unattached cells. The loaded microcarriers were then suspended in 10 mL of CCM and transferred into the RWV culture system. For this purpose, a Synthecon RCCS-8DQ bioreactor (Synthecon) fitted with 8 disposable 10 mL

high aspect ratio vessels (HARVs) was employed. Rotation was initially set to 12 rpm and monitored closely so as to ensure freefall and minimize contact with the walls of the vessel. After 48 hours of equilibration, the CCM was removed and replaced with OBM supplemented with 10μM GW9662 to generate OEhMSCs throughout the course of the experiment. For co-culture experiments, dsRed-labeled MOSJ cells were loaded onto microcarriers using the same method as the hMSCs but in this case, 400,000 MOSJ-cells were loaded onto a total combined growth area of 10 cm^2. The MOS-J laden microcarriers were added to the HARVs 24 hours after the hMSCs, halfway through the equilibration period, 24 hours before addition of OBM. 80% of the OBM media was replenished every 2 days. Entire cultures were harvested at day 0 (at the time of OBM addition) and at day 4 and 8 post addition of OBM. For this purpose, 5 mL media was cleared by centrifugation and retained for ELISA. The cell laden microcarriers were then recovered by centrifugation, washed in PBS and gently dissociated by trituration. 20% of the microcarriers were subjected to ALP kinetic assay, 75% were cryopreserved in liquid nitrogen for RNA extraction and approximately 5% was visualized by microscopy. Monolayer controls were performed in 50 cm^2 plates or 12-well plates (Corning, Corning, NY) in exactly the same way, but MOSJ cells were added directly and cells were recovered by trypsinization.

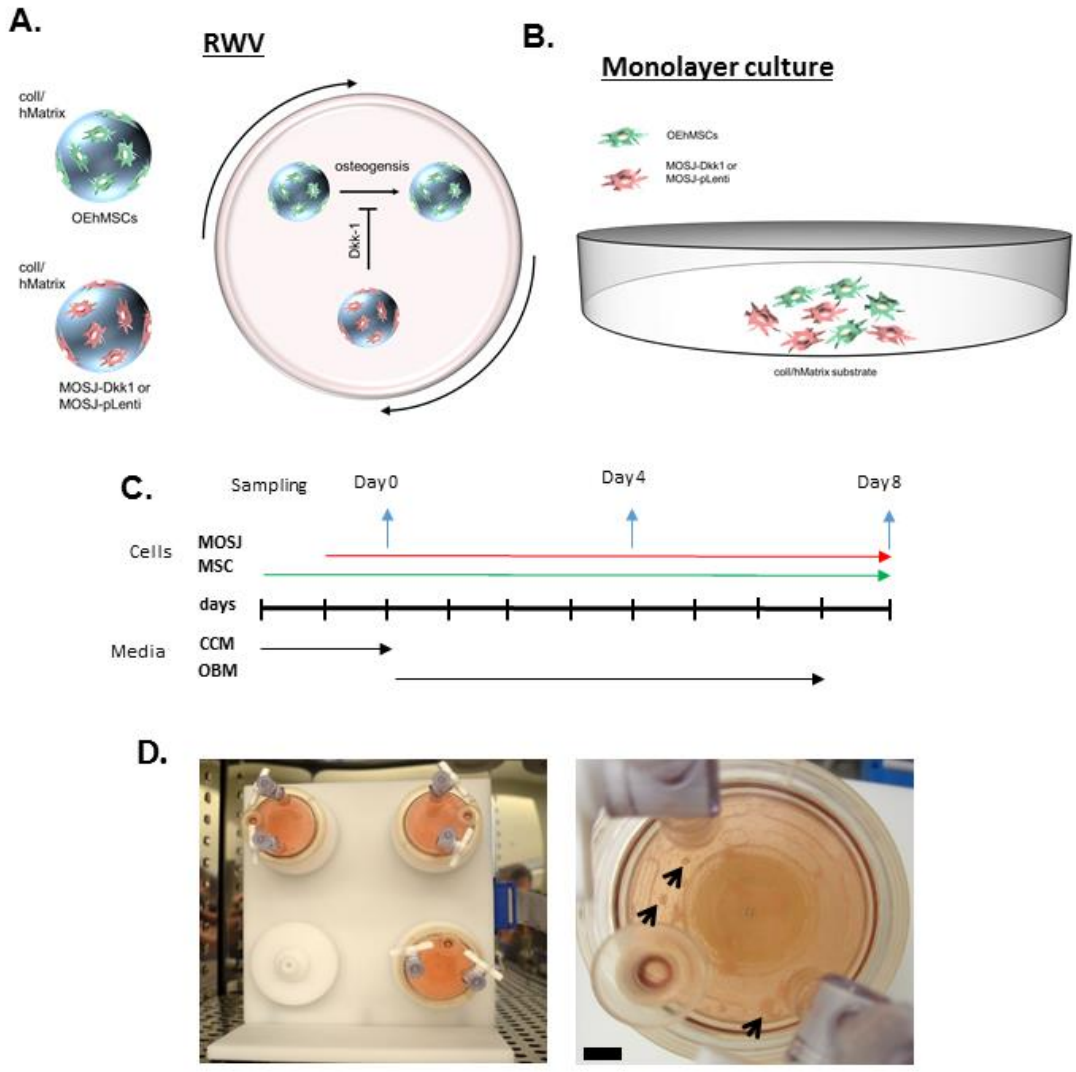

Figure 18: Experimental setup of RWV and monolayer co-cultures.Panel A-B: GFP-labeled MSCs and dsRed labeled MOSJ OS cells (MOSJ-Dkk1 or MOSJ-pLenti controls) were loaded onto collagen I or ECM coated polystyrene microcarriers and co-cultured for up to 8 days under osteogenic conditions in a Synthecon RWV system. Equivalent control assays are performed using monolayer cultures. **Panel C:** Time course for media changes and sampling. Cell numbers and osteogenic assays are performed at day 0, day 4 and day 8 post osteogenic induction. CCM: complete culture media. OBM: osteogenic base media. **Panel D:** RWV set up with 3 x 10 mL cultures (*left*) and close-up view (*right*) after 8 days of RWV showing loosely aggregated cell-laden microcarriers containing OEhMSCs and MOSJ-Dkk1 cells (*arrowed*) (bar = 10 mm).

Flow cytometry

The hMSCs were recovered by briefly incubating with trypsin-EDTA (Life Technologies, Carlsbad, CA). A single-cell suspension was then incubated on ice for 30 minutes in PBS containing 2% (v/v) FBS with fluorophore-tagged antibodies or their isotype controls (Becton Dickinson or Beckman Coulter). Antibodies against CD11b (clone BEAR1), CD14 (RMO52), CD19 (J3-119), CD34 (581), CD45 (J.33), CD73 (AD2), CD79a (HM47), CD90 (Thy-1/310), CD105 (IG2), and HLA-DP, DQ, DR (Tu39) were used. A Cytomics FC500 flow cytometer (Beckman Coulter) was used to analyze the cells (minimum of 20,000) and the data was processed using the manufacturer's software (CXP).

Extracellular matrix (ECM) production

ECM was generated from OEhMSCs as described in Chapter II. For solubilization, ECM pellets were suspended and dispersed in 0.1 M ice cold acetic acid (0.6% v/v) with least 10 mg ECM per mL of acetic acid. Suspensions were sonicated in a cold water bath sonicator (Bransonic) with 6 x 5 second bursts over 60 seconds initially, then at 15 hours, and finally at 30 hr. During the 30 hr period, the solutions were stored at 4ºC with rapid stirring. On average, solutions of 3-5 mg/mLcould be attained.

Preparation of extracellular matrix (ECM)-coated microcarriers

Reagents were sourced from Fisher Scientific unless otherwise stated. Enhanced Attachment Microcarriers (Corning) were used for ECM attachment with a size range of 125-212 μm, density of 1.026 g per cm^3, and 360 cm^2 growth area per gram. Prior to

use, the microcarriers were washed thoroughly with sterile deionized water and suspended to a final concentration of 200 mg/mL. Ten mg of N-(3-Dimethylaminopropyl)-N′-ethylcarbodiimide hydrochloride (EDAC) and 10 mg of N-Hydroxysuccinimide (NHS) were dissolved in 10 mL of 0.1 MES buffer containing 0.9% (w/v) sodium chloride (pH 4.7) and filter sterilized. The EDAC/NHS/MES solution was added to the microcarriers and the reaction was allowed to proceed for 15 minutes with shaking at room temperature. The microcarriers were then recovered by centrifugation, washed with sterile PBS, and then reconstituted in PBS containing ECM at a concentration of 1 mg/mL. ECM was allowed to react with the microcarriers for 2 hours on a shaker, in the dark at room temperature. The microcarrier solution was centrifuged, washed with PBS, and finally reconstituted in sterile PBS for storage at 4°C until use. Equivalent collagen I coated control microcarriers were also acquired from Corning. ECM-coated microcarriers were generated by Abishek Tondon and Robert Reese in the Texas A&M University Department of Biomedical Engineering.

Preparation of coated tissue culture plates

A solution of 25 µg/mL collagen I (from rat tail, Sigma) or ECM from OEhMSCs was prepared in dH_2O. Five hundred µL of the solution was dispensed into each well of a 12-well plate. The plates were left at 4ºC for at least 24 hours. The plates were washed with PBS prior to cell seeding.

Electron microscopy

SEM of purified ECM preparations was outsourced to RealView Analytical Laboratory (Roslindale, MA). Samples were washed through an escalating series of

ethanol concentrations (50%-100% (v/v)) and air dried. A thin layer of carbon (~ 10 nm) was then coated onto samples by a Denton Thermo vacuum evaporator and the samples were observed under an FEI/Philips XL30 FEG scanning electron microscope. Coated microcarriers were fixed in 4% (v/v) glutaraldehyde and prepared for SEM by ethanol dehydration and coating with gold-palladium alloy. Microcarriers were visualized using a FEI Quanta 600 scanning electron microscope.

Enzyme-linked immunosorbent assays (ELISA)

A human OPG antibody duo-kit was obtained from (R&D Systems) and the assay was carried out according to the manufacturer's instructions on media diluted 1:5 with PBS containing 5% BSA and 1% (v/v) Tween 20 (Sigma-Aldrich, St. Louis, MO). A human Dkk-1 duo-kit was obtained from (R&D Systems, Minneapolis, MN) and the assay was carried out according to the manufacturer's instructions on undiluted media conditioned for 2-3 days.

Alkaline phosphatase (ALP) assays

For monolayer culture, OEhMSCs were cultured in the presence or absence of MOSJ-Dkk1 or MOSJ-pLenti cells for up to 8 days in 12-well plates. On days 0, 4 or 8 the monolayers were washed twice with PBS, then once with ALP reaction buffer (100 mM Tris-HCl, pH 9, 100 mM KCl and 1 mM MgCl2). 500µl of ALP buffer was then added, immediately followed by 500µl of PNPP (Life Technologies, Carlsbad, CA) A FluoStar plate reader (BMG Biotech) was used to record the absorbance at 405nm every 30 seconds for 10 minutes. For normalization of the measurements, the cells were recovered by trypsinization and enumerated by the fluorescence signal generated by the

dsRed2 (558/583) or eGFP (488/510) labeled MOSJ cells or hMSCs respectively using the plate reader.

For RWV culture, 20% of the microcarriers were washed twice with PBS and once with ALP buffer. 1 mL of ALP buffer was then added to the sample with 1 mLPNPP. 100 µl of the sample was transferred to a microcentrifuge tube containing 100µL 1N NaOH stop solution every minute for 10 min. The samples were then centrifuged through a polyethersulfone spin filter (0.45µm) and transferred to a 96-well plate (Corning, Corning, NY). A FluoStar plate reader (BMG Biotech) was then used to read the absorbance at 405nm. The results were normalized using the cell enumeration obtained by qRT-PCR for GAPDH transcription.

Transcriptome profiling

Two million GFP-labeled hMSCs were attached to collagen I- or ECM-coated microcarriers with a combined growth area of 50 cm^2. The loaded microcarriers were then suspended in 10 mL of CCM and transferred into the RWV culture system. After 48 hours of equilibration, the CCM was removed and replaced with OBM supplemented with 10µM GW9662 so as to generate OEhMSCs. The cultures were incubated for 8 days with changes of media every 2 days. After 8 days, the cell-laden microcarriers were recovered by brief centrifugation, washed in PBS and subjected to total RNA purification. Resultant total RNA yields ranged from 4.5-13.5 µg at a concentration of 150-450 µg/mL with OD260/280 ratios ranging from between 1.85-2.0. Thereafter, sample preparation and data acquisition was performed by the UT Southwestern Genomics and Microarray Core Facility. RNA integrity was confirmed by analysis using

an Agilent 2100 bioanalyzer (Agilent Technologies) and RNA integrity scores were 10 in each case. Biotin-UTP labeled antisense copy RNA (cRNA) was generated from 200 ng of total RNA using a commercially available kit (Illumina TotalPrep RNA Amplification Kit, Life Technologies, Carlsbad, CA). Labeled cRNA was hybridized to a HumanHT-v4.0 Expression BeadChip (Illumina) and visualized with biotin-Cy3 (Amersham). Chips were read on an Illumina Hiscan scanner and analyzed according to standard manufacturer's protocols using GenomeStudio version 3 (Illumina). Background correction, quality control, and quantile normalization were performed in accordance with Illumina standard operating procedures. Mean normalized fluorescent intensities and standard deviations were calculated for each transcript using biological triplicates for each condition. Data for a given transcript were excluded if the standard deviations exceeded 0.25 of the mean. Linear fold changes were calculated between type I collagen and ECM coatings using mean intensity values and lists were compiled of those genes that were upregulated by 2 fold or higher. Gene ontology clustering, tissue expression profiling and pathway analysis was performed using the Database for Annotation, Visualization and Integrated Discovery (DAVID) package version 6.8.

Quantitative real time polymerase chain reaction (qRT-PCR)

Total RNA was extracted from cells using a High Pure RNA isolation kit (Roche Diagnostics, Basel Switzerland). A Superscript III kit (Life Technologies, Carlsbad, CA) was used according to the manufacturer's protocol to synthesize cDNA. The use of a random hexamer/oligo-dT combination was the only deviation from this protocol. For qRT-PCR amplification, 0.5 µg of cDNA was amplified in a 25 µl reaction containing

SYBR Green PCR master mix (Fast SYBR Green, Applied Biosystems) on a C1000 thermocycler fitted with a real time module (CFX96, Bio-Rad laboratories, Hercules, CA). Species-specific primers were used according to the conditions described in Table 6. GAPDH cycle thresholds were used to enumerate cells by plotting 1/logCt by cell number on standard curves. The relative expression of the osteogenic and Wnt-responsive transcripts were calculated using the $2^{-\Delta\Delta CT}$ method [74]. For heat map generation, the data were log transformed and z-normalized to the same scale, then plotted using Rstudio (v1.1.435), ggplot (3.0.0), dplyr (0.7.6) and reshape (1.4.3) programs.

Statistical analysis

GraphPad Prism version 5.00 for windows was used to plot the data and carry out statistical analysis. Normality of distribution and equivalence in variability was calculated by GraphPad software. One-way analysis of variance (ANOVA) was used to analyze multiple tests of means within data sets with Tukey post testing where necessary. t-tests were used to compare single means. Experiments were performed twice and in some cases in different laboratories. N=6 unless otherwise stated, group sizes were determined by power analyses and guided by results of previous studies. Regression analysis was performed by Pearson's correlation. Data were considered significant if the P values were less than 0.05.

Table 6: Primers and PCR conditions utilized in Chapter III.

TARGET	SEQUENCE	CONDITIONS	NOTES
Human GAPDH	FOR ctctctgctcctcctgttcgac REV tgagcgatgtggctcggct	SYBR-green 60°C	Same as Chapter II
Murine GAPDH	FOR catggccttccgtgttccta REV gcggcacgtcagatcca	SYBR-green 60°C	RTPrimerDB ID_473*
Human collagen I	FOR gaacgcgtgtcatcccttgt REV gaacgaggtagtctttcagcaaca	SYBR-green 60°C	Same as Chapter II
Human Runx2	FOR gcaaggttcaacgatctgaga REV tccccgaggtccatctactg	SYBR-green 60°C	Same as Chapter II
Human Osx1	FOR gtgggcagctagaagggagt REV aattagggcagtcgcagga	SYBR-green 60°C	[80]
Human axin	FOR caggacactgctctctcagattca REV tcacaacagcctttgcaggg	SYBR-green 60°C	[130]
Human BMP-2	FOR cccagcgtgaaaagagag REV gagaccgcagtccgtcta	SYBR-green 50°C	Designed in this study

*Sourced from the RTPrimerDB database: http://wwww.medgen.ugent.be/rtprimerb [131]

Results

Co-culture of OEhMSCs and MOSJ cells in the RWV on collagen I-coated microcarriers

As mentioned in Chapter I, collagen I is the main component of ECM and the main protein present in bone. GW9962 exposure induces the secretion of an ECM rich in factors present in anabolic bone such as collagens VI and XII, along with collagen I [44]. Collagen I was chosen as a control substrate that would represent homeostatic bone, rather an anabolic bone. OEhMSCs (generated from BM-hMSC1 in Chapter II) were selected to mimic the osteoprogenitor component of the osteogenic niche as the cells are highly osteogenic and capable of stimulating bone healing *in vivo* [35,42-44]. GFP-hMSCs were characterized according to the parameters described in Chapter II **(Fig4-6)** [25]. Fibroblast-like morphology and GFP-labeling were confirmed by phase contrast microscopy and fluorescence microscopy respectively (**Fig19a**). Multipotency was confirmed be positive staining for mineralization, lipid vacuoles, and sulfated proteoglycans in response to osteogenic, adipogenic or chondrogenic stimuli respectively (**Fig19b**). As in Chapter II (**Fig6**), this hMSC preparation exhibited multipotent potential characteristic of hMSCs. As expected, the hMSCs also expressed the correct pattern if surface antigens required to define a hMSC (**Fig19c**) [25]. These data confirmed that the ihMSCs fundamental characteristics were not altered by GFP labeling. RFP-labeled OS cells expressing Dkk-1 (MOSJ-Dkk1) or control OS cells (MOSJ-pLenti) were employed to mimic osteolytic and osteogenic MBD respectively [129]. The MOSJ cell line was developed from a spontaneous C57BL/6J mouse

osteosarcoma [132]. OEhMSCs and MOSJ cells were first attached to collagen I coated polystyrene microcarriers by incubation with orbital shaking (**Fig 20**).

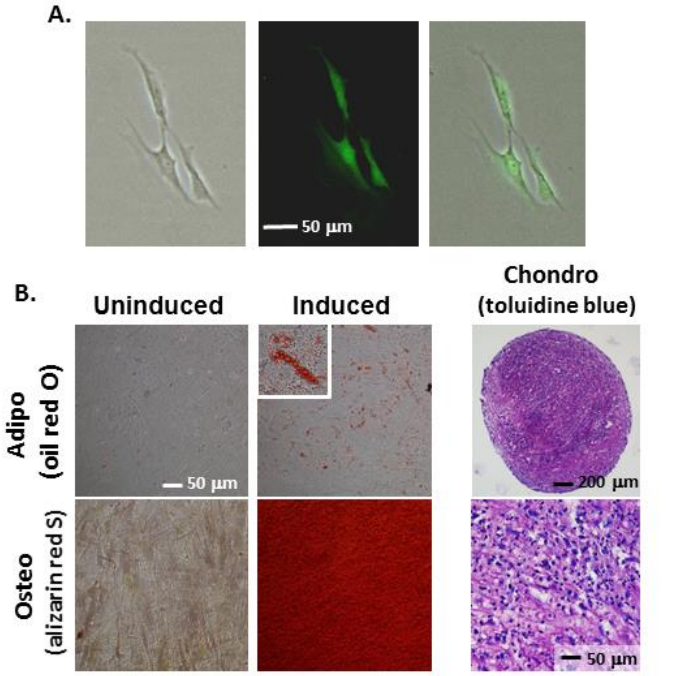

Marker	CD45	CD34	CD14	CD11b	CD79a	CD19	HLA-DR	CD105	CD73	CD90
Positive (%)	1.16	0.82	0.12	0.69	0.87	0.11	0.87	99.83	99.95	99.97

Figure 19: Characterization of GFP-labeled human mesenchymal stem cells used in the study. Panel A: Phase, GFP and merged image of GFP-hMSCs used in the study. **Panel B:** Adipogenic monolayer with lipid vacuoles (magnified in *inset*) stained with oil red O (*above center*). Osteogenic monolayer with mineralized matrix stained with alizarin red S (*below center*). Chondrogenic micromass with articular cartilage stained purple using toluidine blue (*far right*). **Panel C:** Flow cytometry confirmed that the hMSCs express the correct immunophenotype as defined by Dominici *et al.* 2006 [25].

Figure 20: Microcarrier-culture of OEhMSCs and MOSJ cells in a RWV. Panel A: Cells attached to collagen I coated microcarriers before co-culture in the RWV. Micrographs **i-iv** illustrate microcarriers loaded with OEhMSCs, micrographs **v-viii** illustrate microcarriers loaded with MOSJ-Dkk1 cells. Phase (**i, v**), GFP (**ii**), calcein AM staining for non-GFP labeled OEhMSC live cells (**iii**), and staining of dead cell nuclei (**iv**). Phase (**v**), RFP (**vi**), calcein AM staining for live MOSJ cells (**vii**) and Hoescht staining of dead MOSJ nuclei (**iv**). **Panel B-D:** Co-cultures of OEhMSCs and MOSJ-Dkk1 cells on collagen I coated microcarriers. Low- (**panel B**), mid- (**panel C**) and high-power (**panel D**) images indicating presence of RFP-labeled MOSJ-Dkk1 (*right*) and GFP-labeled OEhMSCs (*center*), with both merged with phase images (*left*). High power micrograph in **panel C**, indicates (*arrowed*) OEhMSC-laden sphere with an OEhMSC forming a bridge with a MOSJ-Dkk1 laden sphere.

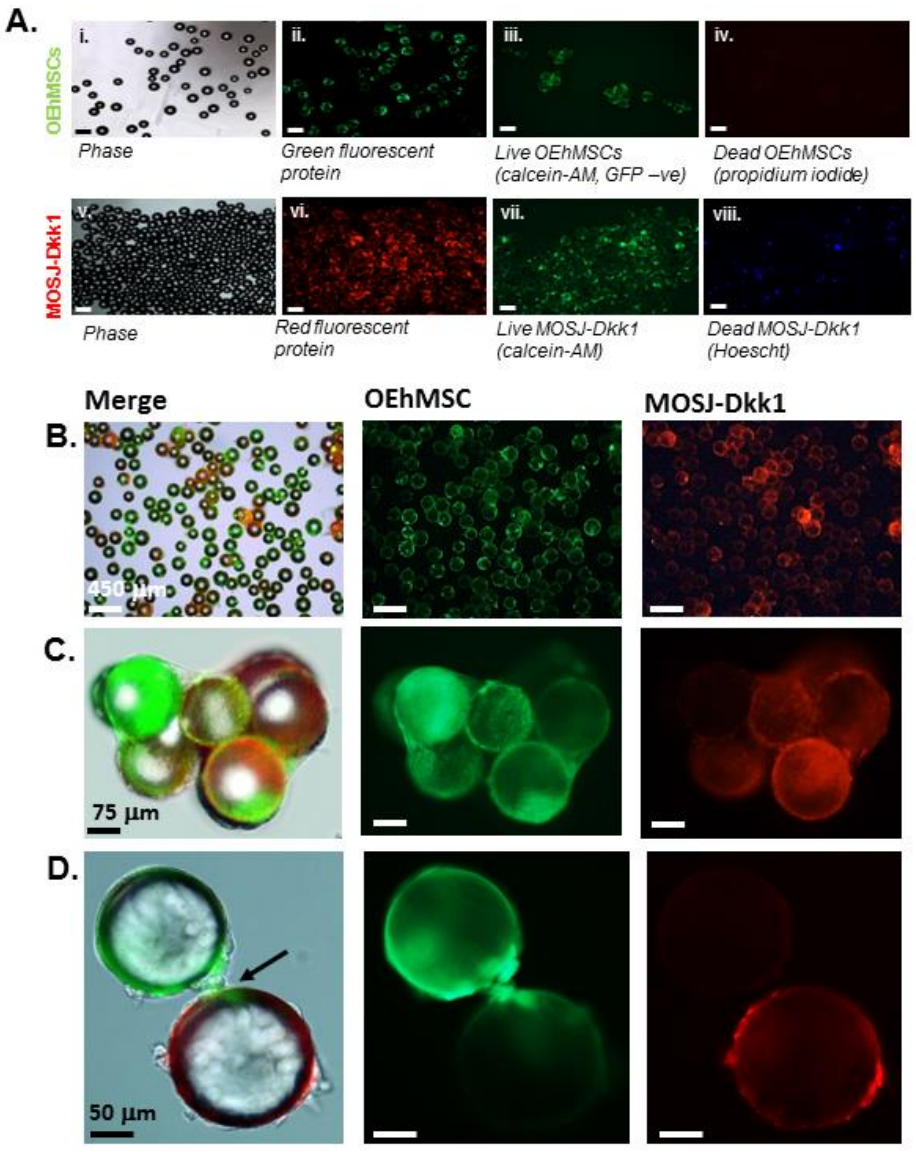

Calcein-AM and propidium iodide or Hoescht staining (live/dead staining) confirmed that the majority the cells attached to the microcarriers were alive (**Fig20a**).

The experimental setup is provided in **Fig18**. The hMSC-laden microcarriers were added first, and allowed to acclimatize for 24 hours before the addition of MOSJ-laden microcarriers. A further 24 hour acclimatization was carried out before the addition of OBM (defined in Chapter II) supplemented with GW9662 to induce the

OEhMSC phenotype. Initially, the microcarriers were homogeneously distributed within the culture vessels. Aggregates of both OEhMSC and MOSJ-laden microcarriers were observed after 3 days of co-culture. Clusters of microcarriers up to 4 mm in diameter (**Fig20c**) were visible after 8 days in co-culture. During early stages of co-culture, OEhMSCs and MOSJ cells remained on their respective microcarriers (**Fig20b**), but transfer of cells between microcarriers was observed in the aggregates (**Fig20c**). The directionality of the transfer was unclear, however, OEhMSCs appeared to migrate by establishing attachment points bridging microcarriers **(Fig20D)**.

While this phenomenon was not observed with MOSJ cells, their presence on the majority of microcarriers with OEhMSCs, suggested that they were also capable of transferring microcarriers.

Osteogenic activity of OEhMSCs in co-cultures with MOSJ cells on collagen I coatings

Unlike their parental line, MOSJ-Dkk1 cells exhibit potent osteoinhibitory and osteolytic properties [129]. It was expected that the osteoinhibitory mechanisms of Dkk-1 could be recapitulated through co-culture with OEhMSCs.

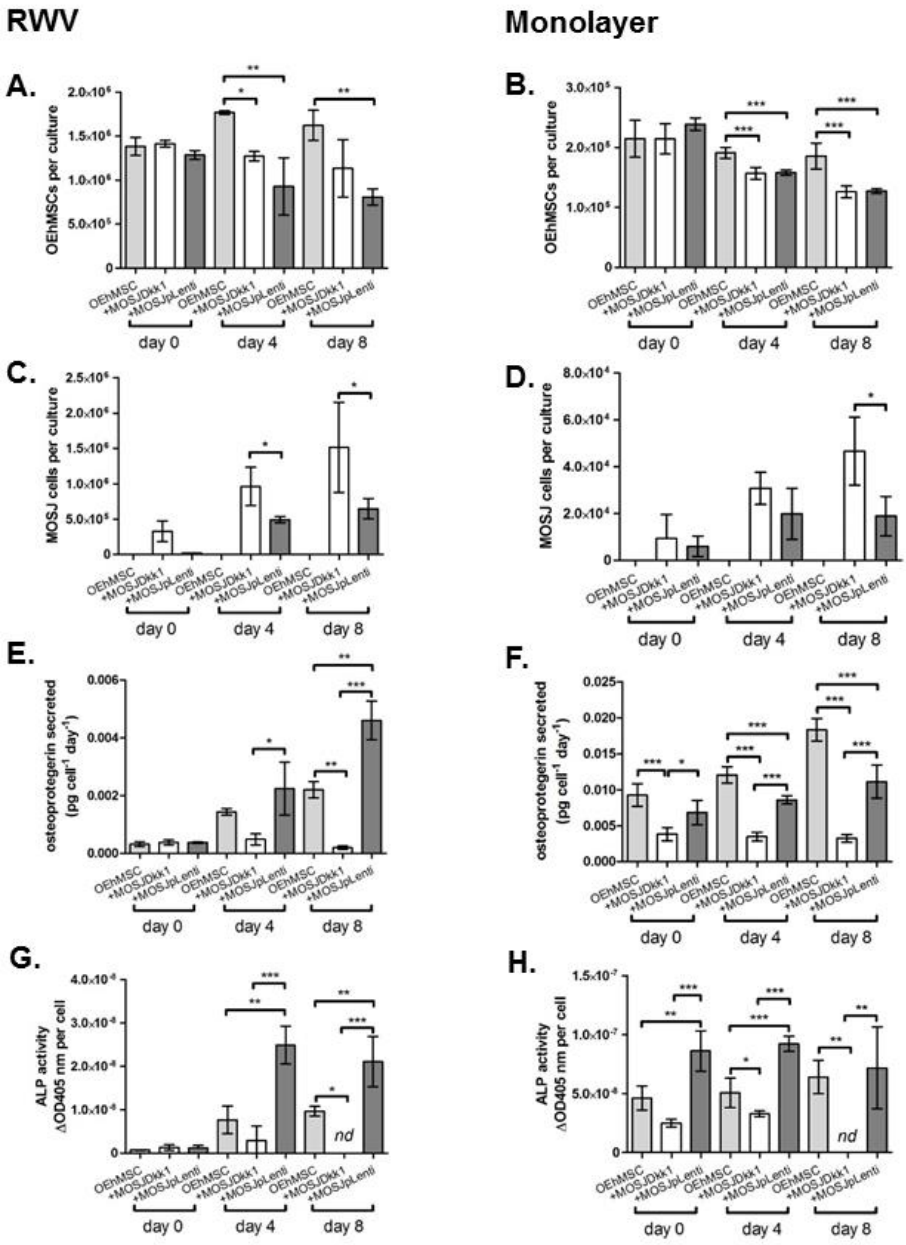

Figure 21: Osteogenic activity of OEhMSCs cultured in the presence and absence of MOSJ-Dkk1 or MOSJ-pLenti cells on collagen I. **Panels A, C, E, G:** RWV co-cultures. **Panels B, D, F, H:** monolayer co-cultures. **Panels A, B:** Enumeration of OEhMSCs (refers to 50 cm^2 growth area). **Panels C, D:** Enumeration of MOSJ cells (refers to 50 cm^2 growth area). **Panels E, F:** Secretion of OPG as measured by ELISA. **Panel G, H:** ALP activity by OEhMSCs cultured for up to 8 days in the presence or absence of MOSJ cells. The label "*OEhMSC*" refers to OEhMSC monoculture and "*+MOSJ…*" refers to co-culture of MOSJ and OEhMSC cells. **Statistics:** Data presented with means and standard deviations. Comparisons were ANOVA with Tukey's post test. P<0.05*, <0.01**, <0.005***.

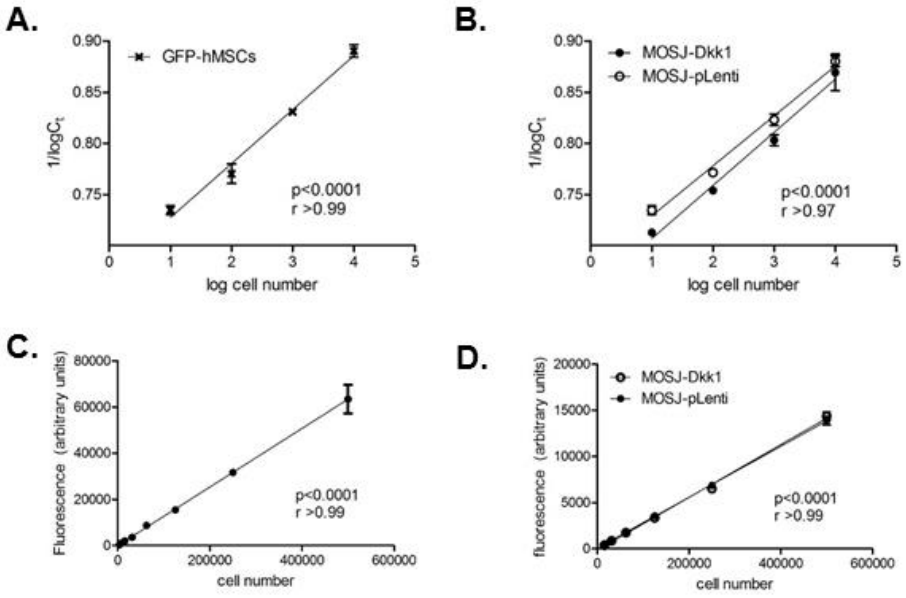

Figure 22: Use of qRT-PCR and fluorescence readings to enumerate GFP-labeled OEhMSCs and RFP-labeled MOSJ cells.Panels A, B: Use of qRT-PCR for enumeration of OEhMSCs and MOSJ cells with species-specific primers for GAPDH (Ct refers to cycle threshold). **Panels C, D:** Use of fluorescence from GFP or RFP to enumerate OEhMSCs and MOSJ cells respectively. In all cases, cell standards were enumerated by hemocytometer before measurements were taken. PCR measurements were employed to count cells in RWV cultures and fluorescence for monolayer cultures. Absolute cell numbers for experimental cultures determined by the plots above. **Statistics:** n=3 with means and standard deviations. Regression analysis performed by Pearson's correlation.

There is conflict in the literature regarding the effect of simulated microgravity on osteogenesis with studies reporting both inhibition and facilitation of osteogenesis [133-135]. As such, initial experiments were performed to confirm that OEhMSCs underwent osteogenesis in the RWV. OEhMSC cell recoveries were significantly higher from RWVs than from monolayers **(Fig21a&b, Fig2a&b)**. OPG secretion increased over time in both RWVs and monolayers, suggesting that osteogenesis was progressing. The final levels of secreted OPG were lower in RWVs than in monolayers (**Fig21e&f**).

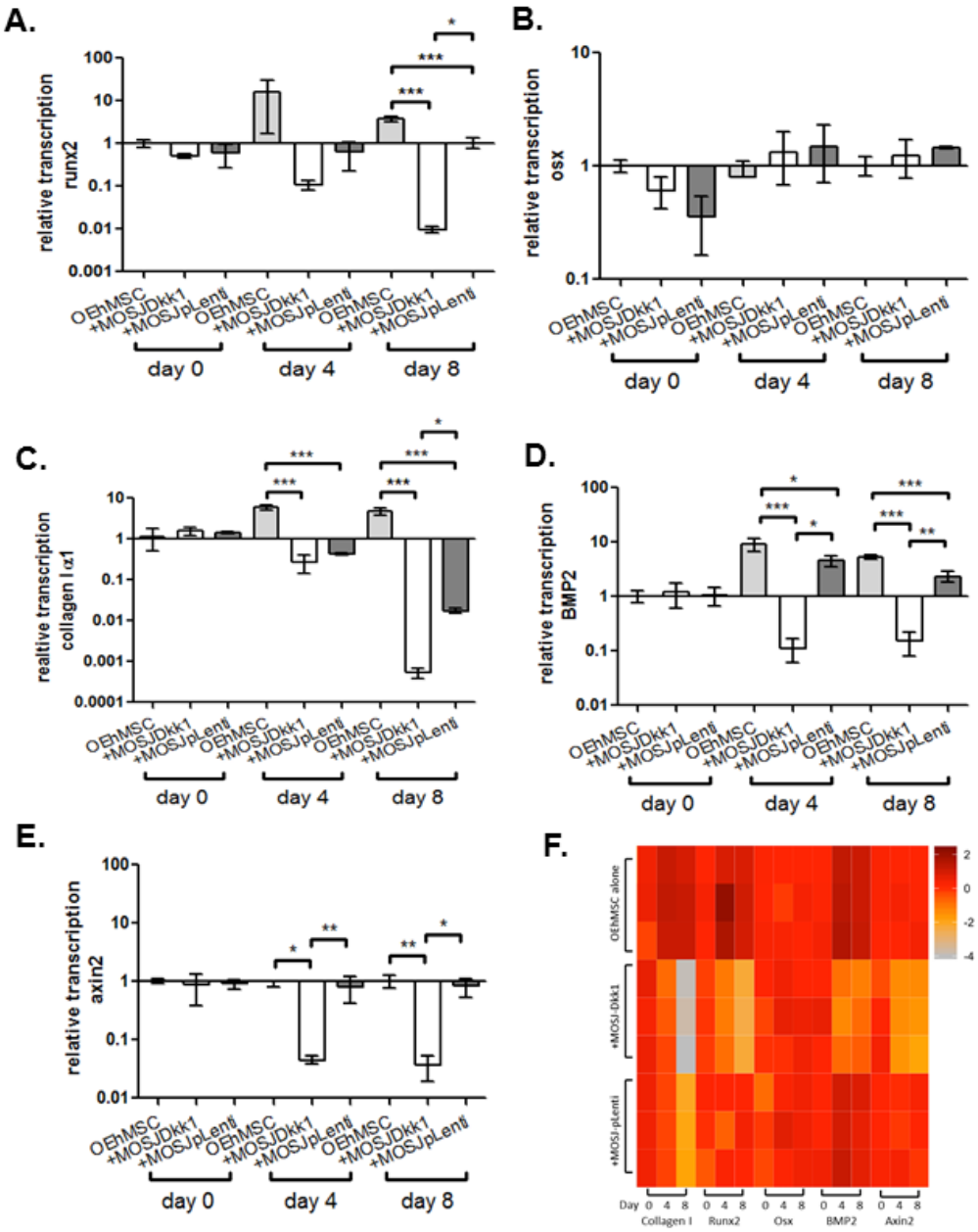

Figure 23: qRT-PCR assays of osteogenic and Wnt-responsive transcripts in RWV co-cultures with collagen I coated microcarriers. Human-specific qRT-PCR was performed for osteogenic transcripts runx2 (**panel A**), osterix (**panel B**), collagen Iα1 (**panel C**) BMP-2 (**panel D**) and Wnt-responsive transcript axin2 (**panel E**). Values are presented as transcription relative to OEhMSC-only control cultures where the expression level is set to 1. **Panel F:** Heat map comparison of data in **panels A-E** with individual measurements indicated. **Statistics:** Statistical treatment as in **Fig 21**.

ALP activity was also higher in monolayer cultures than RWV cultures by day 8 (**Fig21g&h**). Despite the lower levels of osteogenic markers in the RWV cultures as compared to the monolayers, the transition from hMSC to OEhMSC was more apparent in RWVs. The observation of significantly lower baseline OPG and ALP levels, suggested that RWV culture does not facilitate premature osteogenic differentiation of hMSCs, which is commonly seen in monolayers as a response to the stiff surface provided by tissue culture plastic. Osteogenic differentiation by OEhMSCs in RWVs was further supported by increased transcription of the master regulator of osteogenesis, Runx2 (**Fig23a)**, collagen I (**Fig23b)** and BMP-2 (**Fig23d)**. Transcription of the osteogenic transcription factor osterix (OSX) was unaffected (**Fig23b**).

MOSJ-Dkk1 cells proliferated rapidly in both RWV and monolayer cultures. This observation was coupled with a reduction OEhMSC numbers, presumably due to competition for nutrients and attachment (**Fig21a&b, Fig24c&d, Fig25a&b**). As expected, the secretion of Dkk-1 by MOSJ-Dkk1 cells caused a significant inhibition of osteogenesis by OEhMSCs. OPG secretion and ALP activity were reduced in both culture systems, but the monolayer cultures exhibited a greater degree of resistance to the osteoinhibitory stimuli (**Fig21e-h**). Transcription of Runx2, collagen I, and BMP-2 were also reduced as compared to OEhMSCs cultured alone (**Fig22a, c&d**). Axin2, a reporter for the cWnt pathway, was significantly downregulated by co-culture with MOSJ-Dkk1 **(Fig22e)**. This was expected as Dkk-1 is known to exert its' osteoinhibitory by inhibiting cWnt signaling [136].

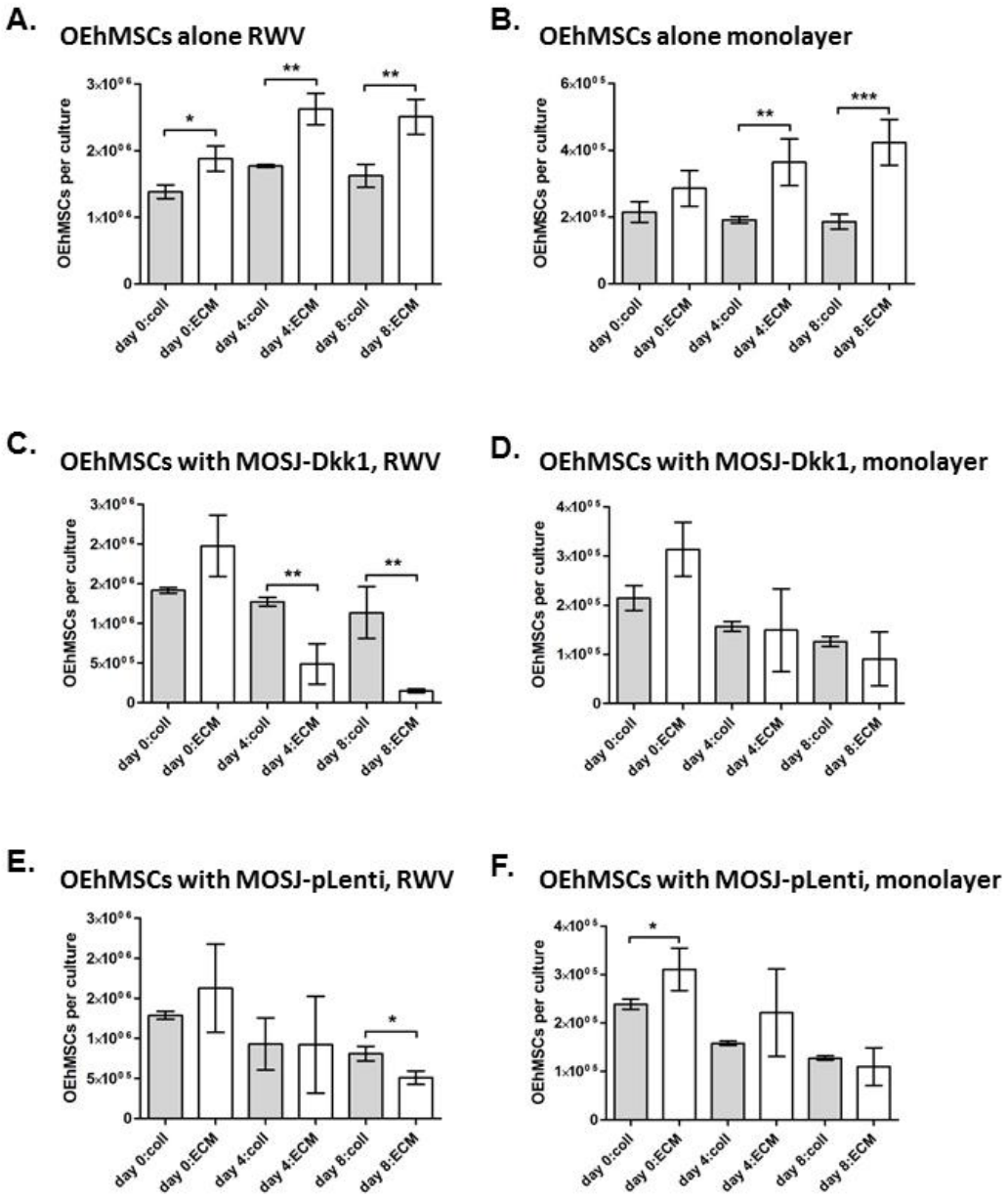

Figure 24: OEhMSC recoveries after culture on OEhMSC derived ECM as compared to collagen I. **Panel A:** OEhMSC recoveries after culture in the RWV. **Panel B:** OEhMSC recoveries after monolayer culture. **Panel C:** OEhMSC recoveries after culture in the RWV with MOSJ-Dkk1 cells**. Panel D:** OEhMSC recoveries after monolayer culture with MOSJ-Dkk1 cells. **Panel E:** OEhMSC recoveries after culture in the RWV with MOSJ-pLenti cells**. Panel F:** OEhMSC recoveries after monolayer culture with MOSJ-pLenti cells. **Statistics:** n=3 for **a,c** and **e**, and n=4 with **b, d** and **f**. Plotted with means and standard deviations, statistical analysis ANOVA with Bonferroni selected pairs analysis, $p<0.05$ *, $p<0.01$ **, $p<0.005$ ***. All values refer to 50 cm^2 growth area.

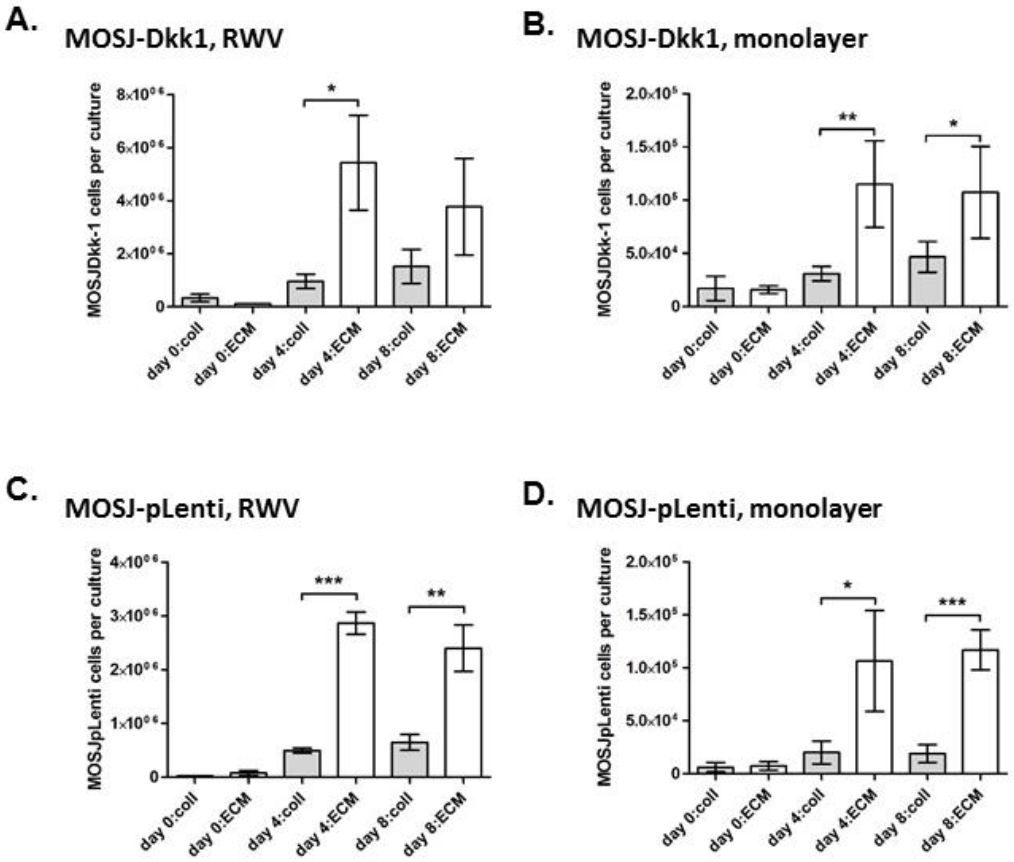

Figure 25: MOSJ recoveries after culture on OEhMSC derived ECM as compared to collagen I. Panel a: MOSJ-Dkk1 recoveries after culture in the RWV. **Panel b:** MOSJ-Dkk1 recoveries after monolayer culture. **Panel c:** MOSJ-pLenti recoveries after culture in the RWV. **Panel d:** MOSJ-pLenti recoveries after monolayer culture. **Statistics:** n=3 for **a** and **c**, and n=4 with **b** and **d**. Plotted with means and standard deviations, statistical analysis ANOVA with Bonferroni selected pairs analysis, $p<0.05$ *, $p<0.01$ **, $p<0.005$ ***. All values refer to 50 cm^2 growth area.

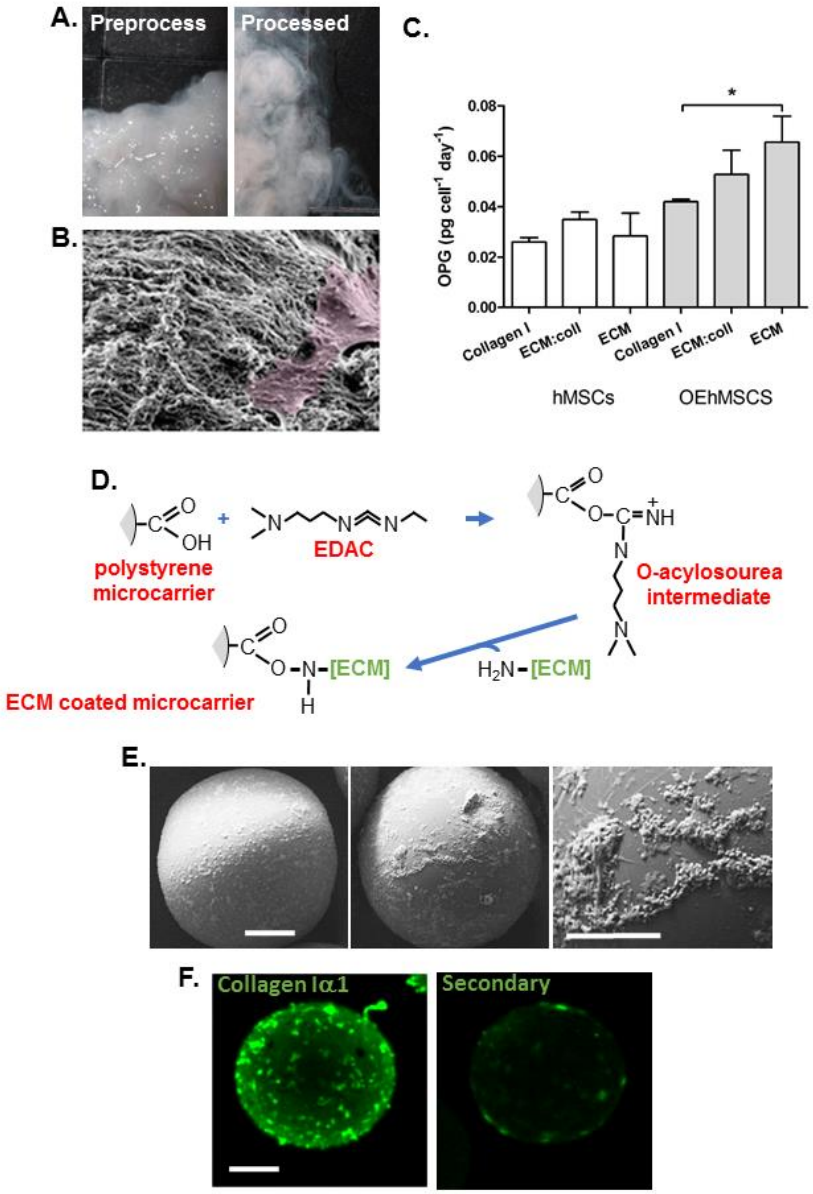

Figure 26: Generation of ECM and ECM-coated microcarriers.Panel A: Appearance of recovered cell monolayers before (*Preprocess*) and after decellularization and processing (*Processed*). **Panel B:** Scanning electron micrograph of hMSC (*pink pseudocolor*) attached to processed ECM. **Panel C:** Normalized secretion of OPG from hMSCs and OEhMSCs attached to tissue culture plastic, rat tail collagen I, ECM, or a 1:1 mixture of collagen I and ECM (statistics: ANOVA with Tukey post test, *=$p<0.05$, n=4). **Panel D:** Reaction scheme employed to covalently attach ECM peptides to polystyrene microcarriers. **Panel E:** *Left to right:* Electron micrograph of polystyrene microcarriers that are uncoated (*bar* = 50 μm), coated with ECM, and coated with ECM at high power (*bar* = 20 μm). **Panel f**: Immunofluorescent staining for human type I collagen, a major constituent of the ECM. "*Secondary*" refers to a control that omits the primary antibody (*bar* = 75 μm).

The control cells for MOSJ-Dkk1 (MOSJ-pLenti) are relatively osteogenic in comparison to the Dkk1-expressing line [129]. Like MOSJ-Dkk1 cells, MOSJ-pLenti cells proliferated in response to co-culture with OEhMSCs, but to a lesser degree. Co-culture of MOSJ-pLenti with OEhMSCs also resulted in a reduction in OEhMSC numbers (**Fig21a-d, Fig24e&f, Fig25c&d**). Inhibition of osteogenesis was not observed in response to co-culture of MOSJ-pLenti with OEhMSCs in either culture system (**Fig21e-h**, **Fig22**). Unlike with MOSJ-Dkk1 co-culture, Axin2 levels remained unchanged **(Fig22e)**, this indicated that the cWnt signaling pathway had not been interrupted by co-culture with MOSJ-pLenti cells. These data demonstrate that RWV culture can facilitate hMSCs differentiation to OEhMSCs. Furthermore, osteogenesis can be inhibited by co-culture with MOSJ-Dkk1 cells via the secretion of Dkk-1, as osteoinhibition was not observed upon co-culture with the control MOSJ-pLenti cells not expressing human Dkk-1.

Processing of ECM and generation of ECM-coated microcarriers

OEhMSC-ECM (hereafter ECM) was generated from OEhMSCs as described in Chapter II [42,44]. The ECM-coated microcarriers were generated by Abishek Tondon and Robert Reese at the Texas A&M University Department of Biomedical Engineering. As described in Chapter II, OEhMSCs generate ECM that contains factors present in anabolic bone tissue [42,44] that support the growth of bone [42,43], likely by recapitulating the osteogenic microenvironment. By coating microcarriers with OEhMSC-ECM and seeding with OEhMSCs the osteogenic niche can be mimicked *in vitro*. The ECM was

acellular and fibrous after processing (**Fig26a&b)** and supported the attachment of hMSCs (**Fig26b)**.

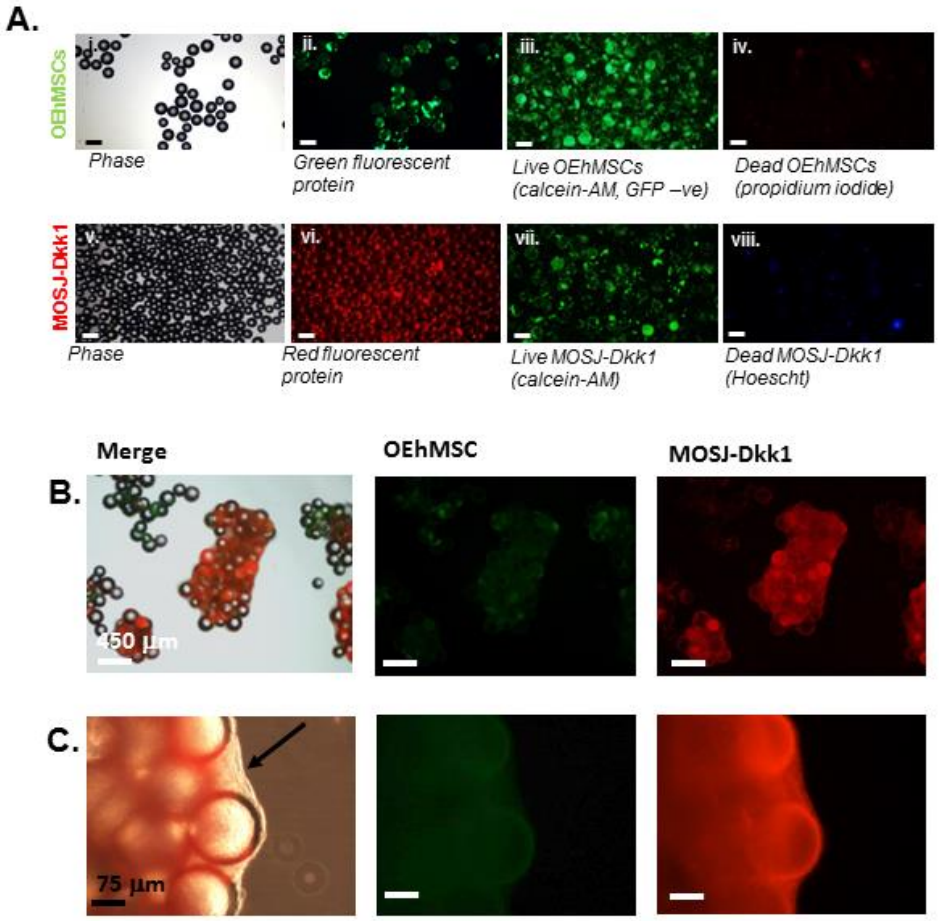

Figure 27: Attachment and co-culture of OEhMSCs and MOSJ cells on OEhMSC-derived ECM coated microcarriers. Panel A: Cells attached to ECM coated-microcarriers before co-culture in the RWV. Micrographs **i-iv** illustrate microcarriers loaded with OEhMSCs, micrographs **v-viii** illustrate microcarriers loaded with MOSJ-Dkk1 cells. Phase (**i**), GFP (**ii**), calcein AM imaging of non-GFP labeled live OEhMSCs (**iii**) and propidium iodide staining of dead cell nuclei (**iv**). Phase (**v**), RFP (**vi**), calcein AM staining for live cells (**vii**) and Hoescht staining of dead cell nuclei (**viii**). **Panel B and C:** Co-cultures of OEhMSCs and MOSJ-Dkk1 cells on ECM coated microcarriers. Low- (**panel B**), and high-power (**panel C**) images indicating abundance of RFP-labeled MOSJ-Dkk1 (*right*) and sparse levels of GFP-labeled OEhMSCs (*center*) with both merged with phase image (*left*). **Panel C** illustrates presence of densely packed clusters of MOSJ-Dkk1 cells held together by ECM (*arrowed*).

OEhMSCs, cultured on ECM-coated monolayers in the presence of an osteogenic stimulus secreted greater amounts of OPG as compared to a mixture of ECM:collagen I and collagen I alone **(Fig26c)**. ECM was covalently attached to microcarriers using EDAC-mediated coupling **(Fig26d)**. Aggregates of ECM on the surface of the microcarriers were visualized by SEM (**Fig26e**). Immunostaining for collagen I, the most abundant protein in the ECM, confirmed that the microcarriers were coated (**Fig26f**).

Osteogenic enhancement of OEhMSCs when attached to ECM-coated microcarriers

The hMSCs were cultured in OBM on ECM-coated microcarriers and collagen I coated microcarriers to investigate if the ECM could enhance osteogenesis. Transcriptome profiling was performed after 8 days in culture and identified 631 transcripts that were upregulated by culture on ECM by more than two-fold. Genes involved with cell attachment and adhesion were highlighted by gene ontology clustering suggesting that ECM provided signals for these functions **(Table7A)**. Bone and bone marrow exhibited the highest enrichment scores when the list was compared with known tissue expression signatures (**Table7B, 8, 9**). This suggests that the genes upregulated by ECM more closely resembled bone and bone marrow that any other tissue types in the database.

Osteogenic activity of OEhMSCs in co-cultures with MOSJ cells on ECM

As with collagen I coatings, the attachment of OEhMSCs and MOSJ cells on ECM-coated microcarriers was confirmed by microscopy (**Fig27a)**. The cultures also generated aggregates and OEhMSC yields were increased as compared to collagen I coated microcarriers in both RWV and monolayer cultures (**Fig24a&b, Fig28a&b**).

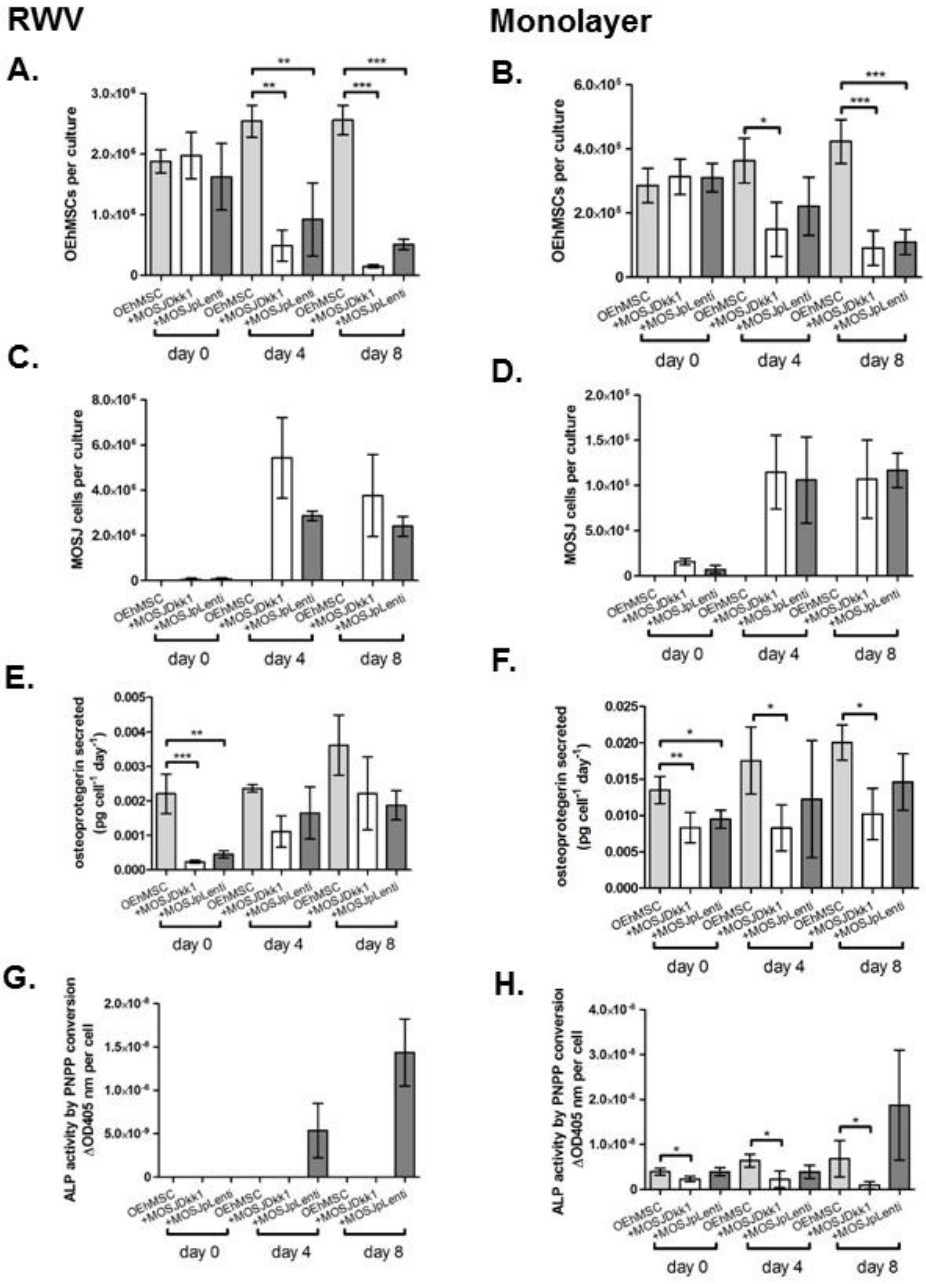

Figure 28: Osteogenic activity of OEhMSCs cultured in the presence and absence of MOSJ-Dkk1 or MOSJ-pLenti cells on ECM: **Panels A, C, E, G:** RWV co-cultures. **Panels B, D, F, H:** monolayer co-cultures. **Panels A, B:** Enumeration of OEhMSCs (refers to 50 cm^2 growth area). **Panels C, D:** Enumeration of MOSJ cells (refers to 50 cm^2 growth area). **Panels E, F:** Secretion of OPG as measured by ELISA. **Panel G, H:** ALP activity by OEhMSCs cultured for up to 8 days in the presence or absence of MOSJ cells. The label "*OEhMSC*" refers to OEhMSC monoculture and "*+MOSJ…*" refers to co-culture with MOSJ and OEhMSC cells. Statistical treatment as in **Fig 21**.

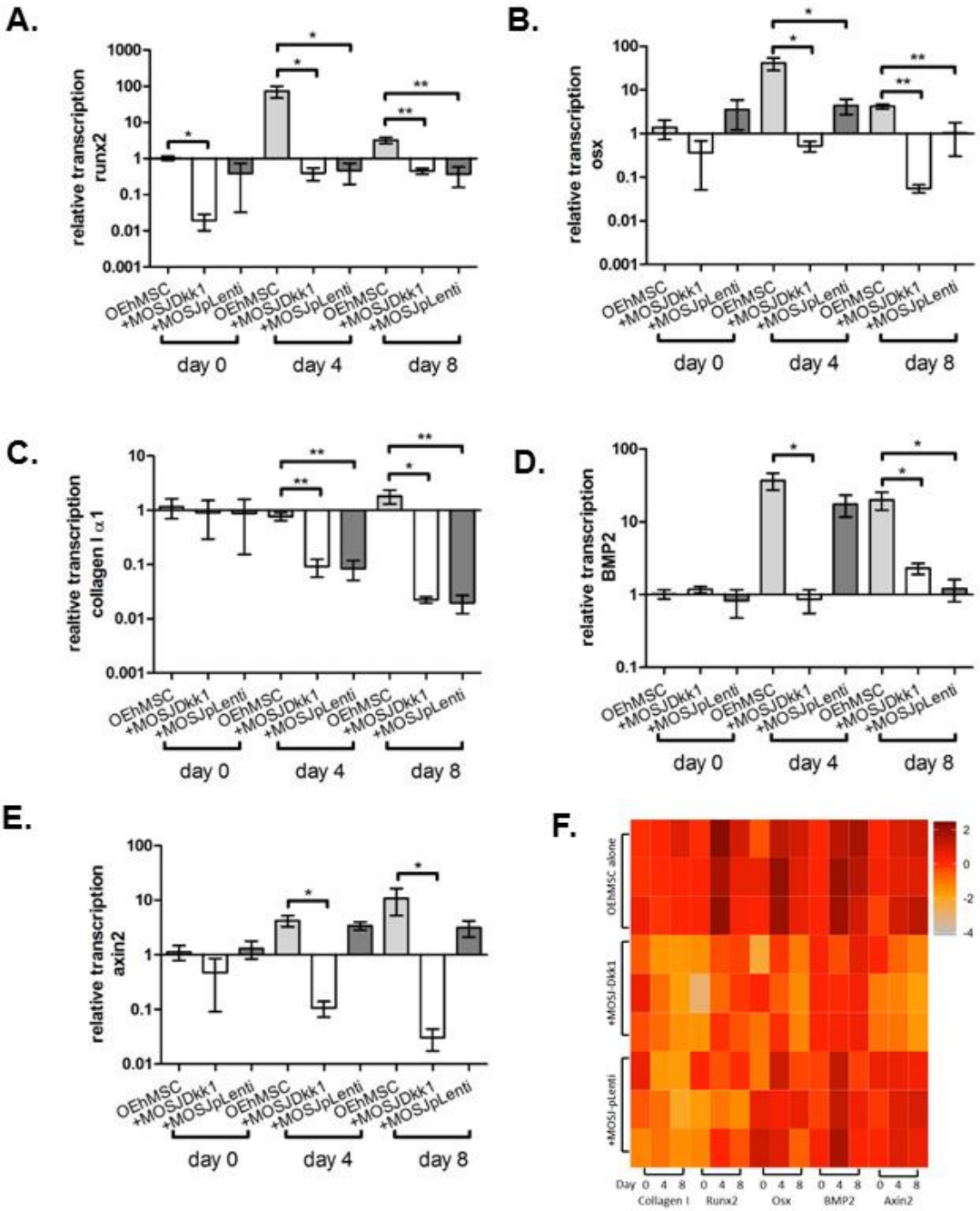

Figure 29: qRT-PCR assays of osteogenic and Wnt-responsive transcripts in RWV co-cultures with ECM coated microcarriers. Human-specific qRT-PCR was performed for osteogenic transcripts runx2 (**panel A**), osterix (**panel B**), collagen Iα1 (**panel C**) BMP-2 (**panel D**) and Wnt-responsive transcript axin2 (**panel E**). Values are presented as transcription relative to OEhMSC-only control cultures where the expression level is set to 1. **Panel F:** Heat map comparison of data in **panels A-E** with individual measurements indicated. Statistics: Statistical treatment as in **Fig 21**.

MOSJ cells rapidly proliferated when co-cultures with OEhMSCs and generated aggregates that appeared to be held together by a dense matrix (**Fig27b&c**). After day 4, OEhMSC yields were reduced by co-culture with either both MOSJ-Dkk1 and MOSJ-pLenti on ECM-coated microcarriers in both culture systems (**Fig28a&b, Fig24c-f**). In RWV cultures, the negative effect of MOSJ cells on OEhMSC recoveries was ECM-dependent since it was not observed with collagen I **(Fig24c)**. The data indicate that ECM promotes a significant increase in MOSJ proliferation. This results in the displacement of OEhMSCs from the ECM.

OPG secretion by OEhMSCs was reduced when co-cultured with both MOSJ subtypes, especially at the early time point. Surprisingly, at day 4 and 8, MOSJ-Dkk1 co-cultures exhibited a comparable amount of OPG as compared to OEhMSCs alone and MOSJ-pLenti co-cultures (**Fig28e,f**) which indicates that attachment to ECM could be rescuing the OPG secretion by OEhMSCs to some degree. On monolayers ALP activity, with ECM coatings were similar to collagen I coatings (**Fig28h**). However, ALP could only be detected in RWV co-cultures containing MOSJ-pLenti cells. This suggests that the ECM may favor early stage osteogenesis and inhibit late stage markers such as ALP (**Fig28g**).

Both Runx2 and OSX, early osteogenic transcription factors, were upregulated in OEhMSCs alone (**Fig29a, b**) by about 100-fold and 50-fold respectively as compared to approximately 10-fold and 1-fold respectively on collagen I. ECM attachment also upregulated BMP-2 by approximately 50-fold at day 4 and day 8 as compared to 8-10 fold on collagen I (**Fig29d**). These data support the hypothesis that ECM upregulates the

early markers of osteogenesis. Co-culture with either MOSJ-Dkk1 or MOSJ-pLenti cells resulted in a reduction of Runx2, OSX, collagen I and BMP-2 transcription (**Fig29a-d**) as compared to controls. As with collagen I coated microcarriers, Axin2 expression was downregulated in OEhMSCs cultured in the presence of MOSJ-Dkk1 cells, again confirming that MOSJ-Dkk1 cells were exerting their osteoinhibitory effects by inhibiting cWnt signaling (**Fig29e**).

Table 7: Analyses of genome profiles generated by OEhMSCs cultured in the RWV on microcarriers coated with OEhMSC-derived ECM as compared to collagen I. A list of transcripts with 2-fold greater transcription when hMSCs differentiated to OEhMSCs on ECM as compared to on collagen I was subjected to analysis using the DAVID database. **Panel A:** Gene ontology clustering. **Panel B:** Association with known tissue expression signatures. The definition of P-values and Enrichment Scores are provided in Huang da *et al* [137,138].

A.

GENE ONTOLOGY		
TERM	**P-value**	**Enrichment**
response to mechanical stimulus	1.90E-06	7.4
integrin binding	2.90E-04	4.2
cellular response to hypoxia	7.00E-04	4.1
positive regulation of cell migration	2.40E-04	3.2
positive regulation of gene expression	1.10E-05	3.2
ECM organization	4.60E-04	3
proteinaceous ECM	3.80E-05	3
aging	3.10E-03	2.9
cell-cell adhesion	1.90E-04	2.8
cadherin binding involved in cell-cell adhesion	1.30E-04	2.8
heparin binding	6.90E-03	2.8
ECM	1.40E-04	2.7
mitochondrial outer membrane	1.10E-02	2.7
angiogenesis	1.60E-03	2.7
focal adhesion	4.10E-05	2.6

B.

TISSUE EXPRESSION		
TERM	**P-value**	**Enrichment**
bone [a]	1.40E-08	4
bone marrow [b]	8.40E-11	3.9
ovary	3.30E-10	3.7
eye	2.10E-08	3.7
brain	1.80E-09	3.7
lung	9.40E-08	3.4
eye	4.70E-10	3.3
vascular	1.90E-05	2.5
thyroid	2.10E-04	2.3
[a,b] refer to Table 8 and 9 respectively		

Table 8: Osteogenic genes upregulated by osteogenically enhanced hMSCs in response to ECM attachment. ENTREZ refers to the Entrez gene ID accession number.

GENE NAME	ENTREZ
Homo sapiens bone morphogenetic protein 2 (BMP-2), mRNA.	650
periostin(POSTN)	10631
decorin(DCN)	1634
glycoprotein nmb(GPNMB)	10457
superoxide dismutase 2, mitochondrial(SOD2)	6648
RAS like proto-oncogene A(RALA)	5898
Ras related GTP binding C(RRAGC)	64121
SMG1, nonsense mediated mRNA decay associated PI3K related kinase(SMG1)	23049
Homo sapiens tumor necrosis factor receptor superfamily, member 11b (TNFRSF11B), mRNA. *Osteoprotegerin.*	4982
2-aminoethanethiol dioxygenase(ADO)	84890
connective tissue growth factor(CTGF)	1490
phosphatidylinositol binding clathrin assembly protein(PICALM)	8301
LRR binding FLII interacting protein 1(LRRFIP1)	9208
transmembrane 9 superfamily member 3(TM9SF3)	56889
leucine rich repeat containing 58(LRRC58)	116064
Homo sapiens bone morphogenetic protein receptor, type II (serine/threonine kinase) (BMPR2), mRNA.	659
coiled-coil serine rich protein 2(CCSER2)	54462
N-acetylglucosamine-1-phosphate transferase alpha and beta subunits(GNPTAB)	79158
plastin 3(PLS3)	5358
heat shock protein family A (Hsp70) member 9(HSPA9)	3313
protein tyrosine phosphatase type IVA, member 1(PTP4A1)	7803
ribosomal L24 domain containing 1(RSL24D1)	51187
TSC22 domain family member 1(TSC22D1)	8848
fibronectin 1(FN1)	2335
lumican(LUM)	4060
ATPase phospholipid transporting 11B (putative)(ATP11B)	23200

Table 9: Bone marrow genes upregulated by osteogenically enhanced hMSCs in response to MSC extracellular matrix attachment.

GENE NAME	ENTREZ
2-aminoethanethiol (cysteamine) dioxygenase	84890
ATPase, class VI, type 11B	23200
COP9 constitutive photomorphogenic homolog subunit 8 (Arabidopsis)	10920
KIAA1128	54462
N-acetylglucosamine-1-phosphate transferase, alpha and beta subunits	79158
Ras-related GTP binding C	64121
SMG1 homolog, phosphatidylinositol 3-kinase-related kinase (C. elegans)	23049
SMT3 suppressor of mif two 3 homolog 1 (S. cerevisiae); SUMO1 pseudogene 3	474338
TSC22 domain family, member 1	8848
adenosylhomocysteinase-like 1	10768
asparaginyl-tRNA synthetase	4677
basic leucine zipper and W2 domains 1 pseudogene 1; basic leucine zipper and W2 domains 1 like 1; basic leucine zipper and W2 domains 1	151579
calmodulin 3 (phosphorylase kinase, delta); calmodulin 2 (phosphorylase kinase, delta); calmodulin 1 (phosphorylase kinase, delta)	805
connective tissue growth factor	1490
cornichon homolog (Drosophila)	10175
cystatin C	1471
decorin	1634
fibronectin 1	2335
gap junction protein, alpha 1, 43kDa	2697
glycoprotein (transmembrane) nmb	10457
heat shock 70kDa protein 9 (mortalin)	3313
isoleucyl-tRNA synthetase	3376
kinase D-interacting substrate, 220kDa	57498
leucine rich repeat (in FLII) interacting protein 1	9208
leucine rich repeat containing 58	116064
lumican	4060
matrin 3	9782
periostin, osteoblast specific factor	10631
phosphatidylinositol binding clathrin assembly protein	8301
plastin 3 (T isoform)	5358
pleckstrin and Sec7 domain containing 3	23362
praja ring finger 2	9867
protein tyrosine phosphatase type IVA, member 1	7803
protein tyrosine phosphatase, non-receptor type 12	5782
ribosomal L24 domain containing 1; similar to ribosomal protein L24-like	51187
ribosomal protein S7; ribosomal protein S7 pseudogene 11; ribosomal protein S7 pseudogene 4; ribosomal protein S7 pseudogene 10	100128060
similar to transmembrane protein 167A; transmembrane protein 167A	100129118
spastic paraplegia 21 (autosomal recessive, Mast syndrome)	51324
superoxide dismutase 2, mitochondrial	6648
tRNA nucleotidyl transferase, CCA-adding, 1	51095
transmembrane 9 superfamily member 3	56889
v-ral simian leukemia viral oncogene homolog A (ras related)	5898

Discussion

Osteoprogenitors, an appropriate attachment substrate, and a 3D environment are required to recapitulate the osteogenic niche. RWV bioreactors provide a suitable 3D environment to develop this system as they have the potential to support large 3D structures [127,139]. OEhMSCs and their ECM have been shown to regenerate bone *in vivo* [35,42] and as such were chosen to represent the osteoprogenitors and substrate. Microcarriers are commercially available and have predictable characteristics in the RWV bioreactors. Aggregation of microcarriers also mimics the trabecular architecture of bone tissue [140-142]. MBD was represented in the system by an OS cell line engineered to express Dkk-1 (MOSJ-Dkk1). Dkk-1 has been identified as a potent contributing factor in several forms of lytic MBD [117]. MOSJ-Dkk1 cells can generate larger tumors with strong lytic activity *in vivo* as compared to the parental MOSJ cell line that does not express high levels of Dkk-1 [129].

Co-cultures were initially performed on a commercial collagen I coated microcarrier. Over 8-days, OEhMSC yield from RWVs was significantly greater than from monolayer cultures. RWV culture also supported the growth of 3D aggregates, which is not possible with monolayer culture [143]. Reduced osteogenesis in the simulated microgravity of RWV bioreactors [144-146] and microgravity itself [147-149] has been reported in the literature. This study also confirmed that osteogenic differentiation in the RWV was reduced as compared to monolayer culture. Although, while the magnitude of measurements for the osteogenic assays were lower for RWV cultures as compared to

monolayer cultures, the progression of differentiation was more apparent in the RWVs due to the lower level of basal activity.

RWV culture provides an opportunity to study transfer of cells from one attachment site to another that is not available with monolayer cultures. OEhMSCs and MOSJ cells were seeded on two separate populations of microcarriers, but as the cultures progressed, the distribution of cells became homogeneous, suggesting bidirectional transfer. While the mechanism transfer is unclear, hMSCs were observed to be attached to 2 microcarriers simultaneously, suggesting that the migration was due to cell motility. Transfer between microcarriers through detachment and reattachment is also possible [150], although this phenomenon was not observed in the co-cultures. Tumor cells have an aptitude for extended survival without attachment, so this method of transfer would be more likely to pertain to tumor cell transfer. The data suggest that the RWV co-culture system could be utilized for the study of tumor cell engraftment.

OEhMSC-ECM enhances osteogenesis [35,42-44]. ECM accelerated osteogenesis by hMSCs in the RWV system under an osteogenic stimulus. However, the data also indicated that ECM upregulates the expression of early markers of osteogenesis such as OPG, Runx2 and BMP-2 and inhibits later stage markers such as ALP. OSX works downstream of Runx2 during osteogenesis [151] and was upregulated over time on the ECM-coated microcarriers. This was not observed with the collagen I coated microcarriers suggesting that the ECM may provide an increased osteogenic stimulus. However, Col1a1 expression by OEhMSCS was lower on the ECM-coated microcarriers. As ECM provides a more complete microenvironment for the cells, the

secretion of collagen I and other matrix proteins is likely downregulated. Whereas on collagen I coated microcarriers, the cells need to condition their microenvironment by secreting ECM proteins, including collagen I. Inhibition of ALP activity on ECM in the RWV bioreactors was not expected. ALP activity is known to be involved in mineralization [152], which occurs in later stages of osteogenesis. OEhMSCs were previously shown to enhance bone healing during the intramembranous ossification phase of bone healing in the murine defect model used in Chapter II. ECM was shown to extend the activity of the OEhMSCs into the remodeling phase of bone healing [44]. This could suggest that ECM secreted by OEhMSCs maintains the OEhMSCs in an earlier stage of osteogenesis without terminally differentiating to mature osteoblasts. The correlation between increased bone healing and increased osteoclast activity observed in Chapter II provides support for this hypothesis. Increased osteoclast activity and therefore increased remodeling of the ECM could alter the composition of the ECM to favor the mineralization stage of bone healing. Inhibition of osteoclast activity by the addition supraphysiological numbers of osteoprogenitors could appeared to reduce bone healing, possible by preserving the ECM in a state that favors the early stages of osteogenesis. When MOSJ cells were co-cultured with OEhMSCs on ECM, there was an unexpected rapid proliferation of MOSJ cells that resulted in OEhMSCs displacement. This rapid proliferation of MOSJ cells was coupled with the secretion of a dense matrix surrounding the aggregates, could serve as an alternative mechanism of osteoinhibition, rather than the secretion of Dkk-1 as is seen on collagen I coated microcarriers. While the composition of this matrix was not evaluated, it likely supports imbalanced bone

homeostasis skewed in favour of bone catabolism. Dkk-1 – mediated inhibition of osteogenesis was captured on the collagen I coatings without the excessive tumor growth observed on ECM. There collagen I may provide a better substrate to evaluate subtle mechanisms while ECM may be better suited to studies that require the aggressive formation of 3D tumor-like tissues.

Inihibiton of cWnt by Dkk-1 and resultant osteoinhibition has been demonstrated by a number of *in vitro* studies, [115,117,118,153]. These studies have identified Dkk-1 as a promising target for treatment of OLs. However, very few co-cultures focusing on the interaction of Dkk-1 expressing tumors and osteoprogenitors have been performed despite reports that the presence of stroma can profoundly affect proliferation and viability of tumor cells [115,154]. In this study, OEhMSCs co-cultured with OS cells demonstrate that although Dkk-1 expression has an inhibitory effect on osteogenesis, competition for attachment sites as a result of rapid OS cell proliferation is likely to contribute to the pathology of MBD.

The use of the RWV bioreactor to model bone-tumor interactions provided several advantages over standard monolayer culture, including increased cell yields, a more accurate mimic of the topology of bone tissue, and lower baseline osteogenic signals. RWV cultures also provide the ability to study transfer of cells from one attachment site to another and introduced a feasible approach for the comparison of different attachment substrates.

CHAPTER IV

CONCLUSION

Following decades of extensive research, the development of a cell-based therapy involving MSCs or their secreted factors appears to be imminent. Numerous clinical trials have demonstrated that MSCs themselves and some secreted factors are well tolerated for a variety of conditions, however, their limited availability coupled with the need for vast amounts of cells for a clinical dose present a major roadblock [155]. Furthermore, their value to provide tools for research has also been demonstrated. MSC-secreted ECM is already commercially available as a tissue culture substrate to preserve *in vivo* characteristics that are altered by tissue culture plastic [47,156]. As mentioned in Chapter I, the ECM provides a dynamic microenvironment that provides tissue-specific signals. This is highlighted by the enhanced support provided to MSCs by tissue-matched ECM [156]. ECM-derived from BM-hMSCs favored osteogenic differentiation while ECM-derived from adipose-derived MSCs (AD-hMSCs) favored adipogenic differentiation by mimicking their respective microenvironments [156]. These reports support the hypothesis that OEhMSC/OEihMSC-ECM would mimic an anabolic bone microenvironment, due the upregulation of factors present in anabolic bone in response to GW9662 exposure [42,44].

The use of iPSCs as a source of MSCs can provide an infinite source of material, overcoming the issues regarding their limited availability, and loss of efficacy with extensive culture. The data demonstrate that ihMSCs are highly osteogenic, capable of

mineralizing with simple osteogenic stimuli that lacks dexamethasone. Furthermore, a significant additional osteogenic stimulus provided by inhibiting PPARγ signaling, thereby upregulating cWnt signaling, promotes a highly osteogenic phenotype in the ihMSCs. OEihMSCs secrete large amounts of ECM rich in collagens VI and XII, two major components of the osteogenic microenvironment and anabolic bone [44]. This is critical as the majority of bone graft materials are biologically inert, or derived from homeostatic cadaveric bone [53], and therefore do not transduce a sufficient osteogenic signal. This is evident by their poor osteogenic properties as compared to autologous bone grafts [53,61]. Autologous bone grafts promote bone growth by three mechanisms of action, osteoconduction, osteoinduction, and osteogenesis, while alternative treatments only promote bone growth by one or two of these mechanisms, making the therapy less efficacious. OEihMSC-ECM induces remarkable levels of bone healing without the need for exogenously added cells and therefore likely promotes bone growth by osteoconduction, osteoinduction, and osteogenesis like autologous bone grafts. OEihMSC-ECM promoted approximately 4-6 fold more bone healing that the BMP-2 positive control. Unlike other alternatives to autologous bone graft, BMP-2 is considered highly osteoinductive, although it has been linked to potential severe adverse effects when used incorrectly [61]. The addition of exogenous osteoprogenitors resulted in decreased bone healing. This was coupled with a reduction in osteoclast activity, suggesting that sufficient remodeling in the defect site is required to promote high levels of bone healing. The observation in Chapter III that ALP activity was reduced in

OEhMSCs cultured on OEhMSC-ECM as compared to collagen I supports this hypothesis. It suggests that the OEhMSC-ECM favors early stage osteogenesis, with remodeling likely required by the cells to facilitate late stage osteogenesis, and mineralization. The reduction in healing caused by the addition of exogenous cells was greater with OEihMSCs. As shown in Chapter II, these cells are highly osteogenic and exhibit increased OPG secretion in response to OEihMSC-ECM attachment. OPG inhibits the activation of osteoclasts be binding to RANKL [15], which is likely responsible for the reduction in bone formation in the OEihMSC-ECM + OEihMSC group. A slight increase in bone formation and osteoclast activity in the OEihMSC-ECM + hBM group supports this hypothesis, as hBM contains far fewer hMSCs. This hypothesis is further supported by the observation that a homeostatic ratio of hMSCs to other bone marrow-derived cells is required, with a lower ratio of hMSCs to other bone-marrow-derived cells serving as a predictor for osteogenesis during anterior cervical discectomy and fusion (ACDF) [157]. The observations from Chapter II add to a growing body of evidence that challenge the hypothesis that more hMSCs equates to more efficacious bone healing. The data show that when implanted into a sufficiently perfused site *in vivo*, the OEihMSC-ECM has the capacity to recapitulate the osteogenic microenvironment, facilitating cell infiltration, which results in accelerated bone repair.

A cell-free osteoinductive pluripotent cell-derived biologic would not be subject to the caveats associated with current strategies to promote bone healing, such as donor site morbidity, cytotoxicity, pathogen transfer, or severe inflammatory response.

However, scalability presents a potential issue. While OEihMSCs secrete significantly more ECM than OEhMSCs, ~85µg/cm^2 is not sustainable with monolayer tissue culture techniques. The platform developed in Chapter III confirms that OEhMSCs secrete ECM when cultured on microcarriers in RWV bioreactors [108]. This suggests that large scale bioreactors [158] may provide a viable alternative to monolayer culture to generate clinically relevant amounts of OEihMSC-ECM. Future work for this project should aim to generate and characterize OEihMSC-ECM in a scalable microcarrier culture system. Although a reduced ECM yield per cm^2 would be expected due to the lower baseline osteogenic levels of OEhMSCs in RWV bioreactors observed in Chapter III.

Another solution to this scalability could be to reduce the amount of OEihMSC-ECM needed for a scaffold. In Chapter II, pure OEihMSC was administered to the defects, however, it was previously shown that OEhMSC-ECM can be coated onto a material, such as Gelfoam, and administered to a defect [42,43]. In a rodent posterolateral fusion model, OEhMSC-coated gelfoam co-administed with OEhMSCs or hBM induced a comparable level of bone formation as a syngeneic bone graft. Furthermore, a slight decrease in bone formation was observed with the addition of OEhMSCs as compared to hBM [43]. This echoes the observations from Chapter II, although not as pronounced, which could be explained by the higher osteogenic potential, and therefore OPG secretion exhibited by the OEihMSCs.

Conventional monolayer tissue culture and animal models are not sufficient to study the complex bone-tumor interactions present in MBD and the formation of OLs.

This is evidenced by the lack of therapeutic options that sufficiently address the need to repair OLs to prevent relapse and the generation of chemotherapy-resistant tumors. The osteogenic microenvironment can be recapitulated *in vitro* by culturing osteoprogenitor cells on microcarriers coated with OEhMSC-derived ECM in a 3D culture system [108]. This provides an experimentally accessible platform to study bone-tumor interactions. As the role of Dkk-1 in MBD is well established, the use of this platform was validated by capturing osteoinhibition by Dkk-1 secreted from osteolytic OS cells. As RWV bioreactors facilitate the growth of large tissue-constructs, this system could be applied to patient-derived tumors, to develop patient-specific treatment protocols. Unlike monolayer culture, transfer of cells between attachment sites was observable in the 3D system. This highlights the utility of this system in metastasis or engraftment studies. The rapid proliferation of MOSJ-Dkk1 on ECM-coated microcarriers, resulting in displacement of OEhMSCs observed in Chapter III indicates that competition for attachment sites is at least partially responsible for osteoinhibition in MBD. The secretion of Dkk-1 by OS cells downregulates osteogenesis by inhibiting the cWnt signaling pathway, reducing osteogenesis [129]. A reduction in osteoprogenitor numbers would also have a profound effect on bone remodeling, favoring bone catabolism and the formation of OLs. Finally, a dense ECM was observed around the aggregates formed by MOSJ-Dkk1 cells when cultured on OEhMSC-ECM. As the OEhMSC numbers had been significantly reduced, it is likely that this ECM was secreted by the OS cells.

Characterization of this tumor-derived ECM could provide insights into the tumor microenvironment that promotes survival and resistance to chemotherapy.

The studies herein present a novel source for osteoinductive scaffolds and a platform with the capacity to provide new insights into the pathological mechanisms of MBD. The studies are linked by the recapitulation of the osteogenic microenvironment with OEihMSC/OEhMSC-ECM. While applied to two distinct models, both indicated the importance of ECM remodeling in the osteogenic microenvironment. In Chapter II, osteoclast inhibition by the addition of supraphysiological amounts of osteoprogenitors resulted in reduced bone formation, while in Chapter III, OEhMSCs cultured on OEhMSC-ECM displayed upregulated early osteogenic markers and a decrease in late stage markers, suggesting that remodeling was required to facilitate the expression of late stage markers. When introduced to the osteogenic microenvironment presented in Chapter III, the OS cells proliferated rapidly. This suggests that future work for this platform could involve elucidating the mechanisms of tumor metastasis to bone. These studies highlight that accurate recapitulation of the osteogenic microenvironment is required for the development of new scaffolds to promote bone repair, and for research into the complex interactions present in bone tissue.

REFERENCES

1 Jarvelainen, H., Sainio, A., Koulu, M., Wight, T. N. & Penttinen, R. Extracellular matrix molecules: potential targets in pharmacotherapy. *Pharmacological Reviews* **61**, 198-223, doi:10.1124/pr.109.001289 (2009).

2 Daley, W. P., Peters, S. B. & Larsen, M. Extracellular matrix dynamics in development and regenerative medicine. *Journal of Cell Science* **121**, 255-264, doi:10.1242/jcs.006064 (2008).

3 Gattazzo, F., Urciuolo, A. & Bonaldo, P. Extracellular matrix: a dynamic microenvironment for stem cell niche. *Biochimica et Biophysica Acta* **1840**, 2506-2519, doi:10.1016/j.bbagen.2014.01.010 (2014).

4 Rauch, F. & Glorieux, F. H. Osteogenesis imperfecta. *Lancet (London, England)* **363**, 1377-1385, doi:10.1016/s0140-6736(04)16051-0 (2004).

5 Byers, P. H. Osteogenesis imperfecta: perspectives and opportunities. *Current Opinion in Pediatrics* **12**, 603-609 (2000).

6 Fedarko, N. S., Robey, P. G. & Vetter, U. K. Extracellular matrix stoichiometry in osteoblasts from patients with osteogenesis imperfecta. *J Bone Miner Res* **10**, 1122-1129, doi:10.1002/jbmr.5650100718 (1995).

7 Viguet-Carrin, S., Garnero, P. & Delmas, P. D. The role of collagen in bone strength. *Osteoporosis International : a journal established as result of cooperation between the European Foundation for Osteoporosis and the National Osteoporosis Foundation of the USA* **17**, 319-336, doi:10.1007/s00198-005-2035-9 (2006).

8 Canalis, E. Effect of cortisol on periosteal and nonperiosteal collagen and DNA synthesis in cultured rat calvariae. *Calcified Tissue International* **36**, 158-166 (1984).

9 Canalis, E. Effect of glucocorticoids on type I collagen synthesis, alkaline phosphatase activity, and deoxyribonucleic acid content in cultured rat calvariae. *Endocrinology* **112**, 931-939, doi:10.1210/endo-112-3-931 (1983).

10 Rodriguez, J. P., Montecinos, L., Rios, S., Reyes, P. & Martinez, J. Mesenchymal stem cells from osteoporotic patients produce a type I collagen-deficient extracellular matrix favoring adipogenic differentiation. *J Cell Biochem* **79**, 557-565 (2000).

11 Ohnaka, K., Tanabe, M., Kawate, H., Nawata, H. & Takayanagi, R. Glucocorticoid suppresses the canonical Wnt signal in cultured human osteoblasts. *Biochemical and Biophysical Research Communications* **329**, 177-181, doi:10.1016/j.bbrc.2005.01.117 (2005).

12 Canalis, E., Mazziotti, G., Giustina, A. & Bilezikian, J. P. Glucocorticoid-induced osteoporosis: pathophysiology and therapy. *Osteoporosis International : a journal established as result of cooperation between the European Foundation for Osteoporosis and the National Osteoporosis Foundation of the USA* **18**, 1319-1328, doi:10.1007/s00198-007-0394-0 (2007).

13 Raggatt, L. J. & Partridge, N. C. Cellular and Molecular Mechanisms of Bone Remodeling. *Journal of Biological Chemistry* **285**, 25103-25108, doi:10.1074/jbc.R109.041087 (2010).

14 Teitelbaum, S. L. Bone resorption by osteoclasts. *Science* **289**, 1504-1508, doi:10.1126/science.289.5484.1504 (2000).

15 Burgess, T. L. *et al.* The ligand for osteoprotegerin (OPGL) directly activates mature osteoclasts. *The Journal of Cell Biology* **145**, 527-538, doi:10.1083/jcb.145.3.527 (1999).

16 Hayman, A. R. *et al.* Mice lacking tartrate-resistant acid phosphatase (Acp 5) have disrupted endochondral ossification and mild osteopetrosis. *Development (Cambridge, England)* **122**, 3151 (1996).

17 Kular, J., Tickner, J., Chim, S. M. & Xu, J. An overview of the regulation of bone remodelling at the cellular level. *Clinical Biochemistry* **45**, 863-873, doi:https://doi.org/10.1016/j.clinbiochem.2012.03.021 (2012).

18 Lin, G. L. & Hankenson, K. D. Integration of BMP, Wnt, and notch signaling pathways in osteoblast differentiation. *Journal of Cellular Biochemistry* **112**, 3491-3501, doi:10.1002/jcb.23287 (2011).

19 Parameswaran, N. & Patial, S. Tumor necrosis factor-α signaling in macrophages. *Crit Rev Eukaryot Gene Expr* **20**, 87-103 (2010).

20 Ma, Y. L. *et al.* Catabolic effects of continuous human PTH (1--38) in vivo is associated with sustained stimulation of RANKL and inhibition of osteoprotegerin and gene-associated bone formation. *Endocrinology* **142**, 4047-4054, doi:10.1210/endo.142.9.8356 (2001).

21 Alford, A. I., Kozloff, K. M. & Hankenson, K. D. Extracellular matrix networks in bone remodeling. *The International Journal of Biochemistry & Cell Biology* **65**, 20-31, doi:https://doi.org/10.1016/j.biocel.2015.05.008 (2015).

22 Ye, H. *et al.* Enhanced osteogenesis and angiogenesis by PCL/chitosan/Sr-doped calcium phosphate electrospun nanocomposite membrane for guided bone regeneration. *Journal of Biomaterials Science. Polymer edition*, 1-20, doi:10.1080/09205063.2019.1646628 (2019).

23 Shahrousvand, M., Ghollasi, M., Zarchi, A. A. K. & Salimi, A. Osteogenic differentiation of hMSCs on semi-interpenetrating polymer networks of polyurethane/poly(2hydroxyethyl methacrylate)/cellulose nanowhisker scaffolds. *International Journal of Biological Macromolecules* **138**, 262-271, doi:10.1016/j.ijbiomac.2019.07.080 (2019).

24 Niemeyer, P. *et al.* Evaluation of Mineralized Collagen and α-Tricalcium Phosphate as Scaffolds for Tissue Engineering of Bone Using Human Mesenchymal Stem Cells. *Cells Tissues Organs* **177**, 68-78, doi:10.1159/000079182 (2004).

25 Dominici, M. *et al.* Minimal criteria for defining multipotent mesenchymal stromal cells. The International Society for Cellular Therapy position statement. *Cytotherapy* **8**, doi:10.1080/14653240600855905 (2006).

26 Parekkadan, B. & Milwid, J. M. Mesenchymal stem cells as therapeutics. *Annual Review of Biomedical Engineering* **12**, 87-117, doi:10.1146/annurev-bioeng-070909-105309 (2010).

27 Squillaro, T., Peluso, G. & Galderisi, U. Clinical Trials With Mesenchymal Stem Cells: An Update. *Cell Transplantation* **25**, 829-848, doi:10.3727/096368915x689622 (2016).

28 Chen, W. *et al.* Immunomodulatory effects of mesenchymal stromal cells-derived exosome. *Immunologic Research* **64**, 831-840, doi:10.1007/s12026-016-8798-6 (2016).

29 Friedenstein, A. J., Petrakova, K. V., Kurolesova, A. I. & Frolova, G. P. Heterotopic of bone marrow. Analysis of precursor cells for osteogenic and hematopoietic tissues. *Transplantation* **6**, 230-247 (1968).

30 Friedenstein, A. J., Piatetzky, S., II & Petrakova, K. V. Osteogenesis in transplants of bone marrow cells. *Journal of Embryology and Experimental Morphology* **16**, 381-390 (1966).

31 Friedenstein, A. J., Chailakhjan, R. K. & Lalykina, K. S. The development of fibroblast colonies in monolayer cultures of guinea-pig bone marrow and spleen cells. *Cell and Tissue Kinetics* **3**, 393-403 (1970).

32 Friedenstein, A. J., Chailakhyan, R. K. & Gerasimov, U. V. Bone marrow osteogenic stem cells: in vitro cultivation and transplantation in diffusion chambers. *Cell and Tissue Kinetics* **20**, 263-272 (1987).

33 Caplan, A. I. Mesenchymal stem cells. *Journal of Orthopaedic Research* **9**, 641-650, doi:10.1002/jor.1100090504 (1991).

34 Yao, F. *et al.* Trophic Effects of Mesenchymal Stem Cells in Tissue Regeneration. *Tissue Engineering Part B: Reviews* **23**, 515-528, doi:10.1089/ten.teb.2016.0365 (2017).

35 Krause, U. *et al.* Pharmaceutical modulation of canonical Wnt signaling in multipotent stromal cells for improved osteoinductive therapy. *Proc Natl Acad Sci U S A* **107**, 4147-4152, doi:10.1073/pnas.0914360107 (2010).

36 Gordon, M. D. & Nusse, R. Wnt signaling: multiple pathways, multiple receptors, and multiple transcription factors. *The Journal of Biological Chemistry* **281**, 22429-22433, doi:10.1074/jbc.R600015200 (2006).

37 He, X., Semenov, M., Tamai, K. & Zeng, X. LDL receptor-related proteins 5 and 6 in Wnt/beta-catenin signaling: arrows point the way. *Development (Cambridge, England)* **131**, 1663-1677, doi:10.1242/dev.01117 (2004).

38 Farmer, S. R. Regulation of PPARgamma activity during adipogenesis. *International Journal of Obesity (2005)* **29 Suppl 1**, S13-16, doi:10.1038/sj.ijo.0802907 (2005).

39 Zeng, X. *et al.* Initiation of Wnt signaling: control of Wnt coreceptor Lrp6 phosphorylation/activation via frizzled, dishevelled and axin functions. *Development (Cambridge, England)* **135**, 367-375, doi:10.1242/dev.013540 (2008).

40 Hatsell, S., Rowlands, T., Hiremath, M. & Cowin, P. Beta-catenin and Tcfs in mammary development and cancer. *Journal of Mammary Gland Biology and Neoplasia* **8**, 145-158 (2003).

41 Reya, T. & Clevers, H. Wnt signalling in stem cells and cancer. *Nature* **434**, 843-850, doi:10.1038/nature03319 (2005).

42 Clough, B. H. *et al.* Bone regeneration with osteogenically enhanced mesenchymal stem cells and their extracellular matrix proteins. *J Bone Miner Res* **30**, 83-94, doi:10.1002/jbmr.2320 (2015).

43 Clough, B. H. *et al.* An allograft generated from adult stem cells and their secreted products efficiently fuses vertebrae in immunocompromised athymic rats and inhibits local immune responses. *The Spine Journal : Official Journal of the North American Spine Society* **17**, 418-430, doi:10.1016/j.spinee.2016.10.009 (2017).

44 Zeitouni, S. *et al.* Human mesenchymal stem cell-derived matrices for enhanced osteoregeneration. *Science Translational Medicine* **4**, 132ra155, doi:10.1126/scitranslmed.3003396 (2012).

45 Myeroff, C. & Archdeacon, M. Autogenous bone graft: donor sites and techniques. *The Journal of Bone and Joint Surgery. American volume* **93**, 2227-2236, doi:10.2106/jbjs.j.01513 (2011).

46 Katsara, O. *et al.* Effects of donor age, gender, and in vitro cellular aging on the phenotypic, functional, and molecular characteristics of mouse bone marrow-derived mesenchymal stem cells. *Stem Cells and Development* **20**, 1549-1561, doi:10.1089/scd.2010.0280 (2011).

47 Ragelle, H. *et al.* Comprehensive proteomic characterization of stem cell-derived extracellular matrices. *Biomaterials* **128**, 147-159, doi:10.1016/j.biomaterials.2017.03.008 (2017).

48 Kapałczyńska, M. *et al.* 2D and 3D cell cultures - a comparison of different types of cancer cell cultures. *Arch Med Sci* **14**, 910-919, doi:10.5114/aoms.2016.63743 (2018).

49 Barghash, R. F. & Abdou, W. M. Pathophysiology of Metastatic Bone Disease and the Role of the Second Generation of Bisphosphonates: From Basic Science to Medicine. *Current Pharmaceutical Design* **22**, 1546-1557 (2016).

50 Saad, F. *et al.* Pathologic fractures correlate with reduced survival in patients with malignant bone disease. *Cancer* **110**, 1860-1867, doi:10.1002/cncr.22991 (2007).

51 Morshed, S. Current Options for Determining Fracture Union. *Advances in Medicine* **2014**, 708574, doi:10.1155/2014/708574 (2014).

52 Yelin, E., Weinstein, S. & King, T. The burden of musculoskeletal diseases in the United States. *Seminars in Arthritis and Rheumatism* **46**, 259-260, doi:10.1016/j.semarthrit.2016.07.013 (2016).

53 Boden, S. D. Biology of lumbar spine fusion and use of bone graft substitutes: present, future, and next generation. *Tissue Engineering* **6**, 383-399, doi:10.1089/107632700418092 (2000).

54 Watkins, R. t., Watkins, R., 3rd & Hanna, R. Non-union rate with stand-alone lateral lumbar interbody fusion. *Medicine* **93**, e275, doi:10.1097/md.0000000000000275 (2014).

55 Castillo, R. C., Bosse, M. J., MacKenzie, E. J. & Patterson, B. M. Impact of smoking on fracture healing and risk of complications in limb-threatening open tibia fractures. *Journal of Orthopaedic Trauma* **19**, 151-157 (2005).

56 Bishop, J. A., Palanca, A. A., Bellino, M. J. & Lowenberg, D. W. Assessment of compromised fracture healing. *The Journal of the American Academy of Orthopaedic Surgeons* **20**, 273-282, doi:10.5435/jaaos-20-05-273 (2012).

57 Rihn, J. A., Kirkpatrick, K. & Albert, T. J. Graft options in posterolateral and posterior interbody lumbar fusion. *Spine (Phila Pa 1976)* **35**, 1629-1639, doi:10.1097/BRS.0b013e3181d25803 (2010).

58 Carragee, E. J., Hurwitz, E. L. & Weiner, B. K. A critical review of recombinant human bone morphogenetic protein-2 trials in spinal surgery: emerging safety concerns and lessons learned. *The Spine Journal : Official Journal of the North American Spine Society* **11**, 471-491, doi:10.1016/j.spinee.2011.04.023 (2011).

59 Zadegan, S. A. *et al.* Bone Morphogenetic Proteins in Anterior Cervical Fusion: A Systematic Review and Meta-Analysis. *World Neurosurgery* **104**, 752-787, doi:10.1016/j.wneu.2017.02.098 (2017).

60 Kaiser, M. G. *et al.* Guideline update for the performance of fusion procedures for degenerative disease of the lumbar spine. Part 16: bone graft extenders and substitutes as an adjunct for lumbar fusion. *Journal of Neurosurgery. Spine* **21**, 106-132, doi:10.3171/2014.4.spine14325 (2014).

61 Agarwal, R., Williams, K., Umscheid, C. A. & Welch, W. C. Osteoinductive bone graft substitutes for lumbar fusion: a systematic review. *Journal of Neurosurgery. Spine* **11**, 729-740, doi:10.3171/2009.6.spine08669 (2009).

62 Skovrlj, B. *et al.* Cellular bone matrices: viable stem cell-containing bone graft substitutes. *The Spine Journal : Official Journal of the North American Spine Society* **14**, 2763-2772, doi:10.1016/j.spinee.2014.05.024 (2014).

63 Lichte, P., Pape, H. C., Pufe, T., Kobbe, P. & Fischer, H. Scaffolds for bone healing: concepts, materials and evidence. *Injury* **42**, 569-573, doi:10.1016/j.injury.2011.03.033 (2011).

64 Kovach, T. K., Dighe, A. S., Lobo, P. I. & Cui, Q. Interactions between MSCs and immune cells: implications for bone healing. *J Immunol Res* **2015**, 752510, doi:10.1155/2015/752510 (2015).

65 Caplan, A. I. Why are MSCs therapeutic? New data: new insight. *J Pathol* **217**, 318-324, doi:10.1002/path.2469 (2009).

66 Andrzejewska, A., Lukomska, B. & Janowski, M. Concise Review: Mesenchymal Stem Cells: From Roots to Boost. *Stem Cells* **37**, 855-864, doi:10.1002/stem.3016 (2019).

67 Ohnishi, H. *et al.* A comparative study of induced pluripotent stem cells generated from frozen, stocked bone marrow- and adipose tissue-derived mesenchymal stem cells. *Journal of Tissue Engineering and Regenerative Medicine* **6**, 261-271, doi:10.1002/term.428 (2012).

68 Takahashi, K. *et al.* Induction of Pluripotent Stem Cells from Adult Human Fibroblasts by Defined Factors. *Cell* **131**, 861-872, doi:https://doi.org/10.1016/j.cell.2007.11.019 (2007).

69 Izu, Y. *et al.* Type VI collagen deficiency induces osteopenia with distortion of osteoblastic cell morphology. *Tissue and Cell* **44**, 1-6, doi:https://doi.org/10.1016/j.tice.2011.08.002 (2012).

70 Izu, Y. *et al.* Type XII collagen regulates osteoblast polarity and communication during bone formation. *The Journal of Cell Biology* **193**, 1115-1130, doi:10.1083/jcb.201010010 (2011).

71 Izu, Y., Ezura, Y., Koch, M., Birk, D. E. & Noda, M. Collagens VI and XII form complexes mediating osteoblast interactions during osteogenesis. *Cell Tissue Res* **364**, 623-635, doi:10.1007/s00441-015-2345-y (2016).

72 Zhou, H. *et al.* Generation of induced pluripotent stem cells using recombinant proteins. *Cell Stem Cell* **4**, doi:10.1016/j.stem.2009.04.005 (2009).

73 Gregory, C. A., Gunn, W. G., Peister, A. & Prockop, D. J. An Alizarin red-based assay of mineralization by adherent cells in culture: comparison with cetylpyridinium chloride extraction. *Analytical Biochemistry* **329**, 77-84, doi:10.1016/j.ab.2004.02.002 (2004).

74 Livak, K. J. & Schmittgen, T. D. Analysis of relative gene expression data using real-time quantitative PCR and the 2(-Delta Delta C(T)) Method. *Methods (San Diego, Calif.)* **25**, 402-408, doi:10.1006/meth.2001.1262 (2001).

75 Carraro, G., Albertin, G., Forneris, M. & Nussdorfer, G. G. Similar sequence-free amplification of human glyceraldehyde-3-phosphate dehydrogenase for real time RT-PCR applications. *Molecular and Cellular Probes* **19**, 181-186, doi:10.1016/j.mcp.2004.11.004 (2005).

76 Alaseem, A. M. *et al.* Naproxen induces type X collagen expression in human bone-marrow-derived mesenchymal stem cells through the upregulation of 5-lipoxygenase. *Tissue Eng Part A* **21**, 234-245, doi:10.1089/ten.TEA.2014.0148 (2015).

77 Nemoto, T., Kajiya, H., Tsuzuki, T., Takahashi, Y. & Okabe, K. Differential induction of collagens by mechanical stress in human periodontal ligament cells. *Archives of Oral Biology* **55**, 981-987, doi:10.1016/j.archoralbio.2010.08.004 (2010).

78 Lisignoli, G. *et al.* Gene array profile identifies collagen type XV as a novel human osteoblast-secreted matrix protein. *Journal of Cellular Physiology* **220**, 401-409, doi:10.1002/jcp.21779 (2009).

79 Schmidt, A., Lorkowski, S., Seidler, D., Breithardt, G. & Buddecke, E. TGF-beta1 generates a specific multicomponent extracellular matrix in human coronary SMC. *European Journal of Cclinical Investigation* **36**, 473-482, doi:10.1111/j.1365-2362.2006.01658.x (2006).

80 Schaap-Oziemlak, A. M. *et al.* MicroRNA hsa-miR-135b regulates mineralization in osteogenic differentiation of human unrestricted somatic stem cells. *Stem Cells and Development* **19**, 877-885, doi:10.1089/scd.2009.0112 (2010).

81 Zhao, Q. *et al.* MSCs derived from iPSCs with a modified protocol are tumor-tropic but have much less potential to promote tumors than bone marrow MSCs. *Proc Natl Acad Sci U S A* **112**, 530-535, doi:10.1073/pnas.1423008112 (2015).

82 Salem, O. *et al.* Naproxen affects osteogenesis of human mesenchymal stem cells via regulation of Indian hedgehog signaling molecules. *Arthritis Research & Therapy* **16**, R152, doi:10.1186/ar4614 (2014).

83 Gafni, Y. *et al.* Gene therapy platform for bone regeneration using an exogenously regulated, AAV-2-based gene expression system. *Mol Ther* **9**, 587-595, doi:10.1016/j.ymthe.2003.12.009 (2004).

84 Chen, X. *et al.* Chondrogenic differentiation of umbilical cord-derived mesenchymal stem cells in type I collagen-hydrogel for cartilage engineering. *Injury* **44**, 540-549, doi:10.1016/j.injury.2012.09.024 (2013).

85 Gregory, C. A. *et al.* Dkk-1-derived synthetic peptides and lithium chloride for the control and recovery of adult stem cells from bone marrow. *The Journal of Biological Chemistry* **280**, 2309-2323, doi:10.1074/jbc.M406275200 (2005).

86 Krause, U., Seckinger, A. & Gregory, C. A. Assays of osteogenic differentiation by cultured human mesenchymal stem cells. *Methods in Molecular Biology (Clifton, N.J.)* **698**, 215-230, doi:10.1007/978-1-60761-999-4_17 (2011).

87 Bae, H. W. *et al.* Bone marrow enhances the performance of rhBMP-2 in spinal fusion: a rodent model. *The Journal of Bone and Joint Surgery. American volume* **95**, 338-347, doi:10.2106/jbjs.k.01118 (2013).

88 Bruder, S. P., Jaiswal, N. & Haynesworth, S. E. Growth kinetics, self-renewal, and the osteogenic potential of purified human mesenchymal stem cells during extensive subcultivation and following cryopreservation. *J Cell Biochem* **64**, 278-294 (1997).

89 Wang, M., Yuan, Q. & Xie, L. Mesenchymal Stem Cell-Based Immunomodulation: Properties and Clinical Application. *Stem Cells Int* **2018**, 3057624, doi:10.1155/2018/3057624 (2018).

90 Klyushnenkova, E. *et al.* T cell responses to allogeneic human mesenchymal stem cells: immunogenicity, tolerance, and suppression. *Journal of Biomedical Science* **12**, 47-57, doi:10.1007/s11373-004-8183-7 (2005).

91 Zhang, L. *et al.* Chondrogenic differentiation of human mesenchymal stem cells: a comparison between micromass and pellet culture systems. *Biotechnology Letters* **32**, 1339-1346, doi:10.1007/s10529-010-0293-x (2010).

92 Song, I. H., Caplan, A. I. & Dennis, J. E. In vitro dexamethasone pretreatment enhances bone formation of human mesenchymal stem cells in vivo. *Journal of Orthopaedic Research : Official Publication of the Orthopaedic Research Society* **27**, 916-921, doi:10.1002/jor.20838 (2009).

93 Langenbach, F. & Handschel, J. Effects of dexamethasone, ascorbic acid and β-glycerophosphate on the osteogenic differentiation of stem cells in vitro. *Stem Cell Research & Therapy* **4**, 117-117, doi:10.1186/scrt328 (2013).

94 Kundu, A. K., Khatiwala, C. B. & Putnam, A. J. Extracellular matrix remodeling, integrin expression, and downstream signaling pathways influence the osteogenic differentiation of mesenchymal stem cells on poly(lactide-co-glycolide) substrates. *Tissue Engineering. Part A* **15**, 273-283, doi:10.1089/ten.tea.2008.0055 (2009).

95 Lobb, D. C., DeGeorge, B. R., Jr. & Chhabra, A. B. Bone Graft Substitutes: Current Concepts and Future Expectations. *The Journal of Hand Surgery* **44**, 497-505.e492, doi:10.1016/j.jhsa.2018.10.032 (2019).

96 Ibrahim, T., Stafford, H., Esler, C. N. & Power, R. A. Cadaveric allograft microbiology. *International Orthopaedics* **28**, 315-318, doi:10.1007/s00264-004-0579-5 (2004).

97 Murphy, M. B., Suzuki, R. K., Sand, T. T., Chaput, C. D. & Gregory, C. A. Short Term Culture of Human Mesenchymal Stem Cells with Commercial Osteoconductive Carriers Provides Unique Insights into Biocompatibility. *J Clin Med* **2**, 49-66, doi:10.3390/jcm2030049 (2013).

98 Epstein, N. E. Pros, cons, and costs of INFUSE in spinal surgery. *Surgical Neurology International* **2**, 10, doi:10.4103/2152-7806.76147 (2011).

99 Fernandez de Grado, G. *et al.* Bone substitutes: a review of their characteristics, clinical use, and perspectives for large bone defects management. *Journal of Tissue Engineering* **9**, 2041731418776819, doi:10.1177/2041731418776819 (2018).

100 Villa-Diaz, L. G. *et al.* Derivation of mesenchymal stem cells from human induced pluripotent stem cells cultured on synthetic substrates. *Stem Cells (Dayton, Ohio)* **30**, 1174-1181, doi:10.1002/stem.1084 (2012).

101 Liu, J., Chen, W., Zhao, Z. & Xu, H. H. K. Reprogramming of mesenchymal stem cells derived from iPSCs seeded on biofunctionalized calcium phosphate scaffold for bone engineering. *Biomaterials* **34**, 7862-7872, doi:10.1016/j.biomaterials.2013.07.029 (2013).

102 de Peppo, G. M. *et al.* Engineering bone tissue substitutes from human induced pluripotent stem cells. *Proceedings of the National Academy of Sciences of the United States of America* **110**, 8680-8685, doi:10.1073/pnas.1301190110 (2013).

103 Xu, M., Shaw, G., Murphy, M. & Barry, F. Induced Pluripotent Stem Cell-Derived Mesenchymal Stromal Cells Are Functionally and Genetically Different From Bone Marrow-Derived Mesenchymal Stromal Cells. *Stem Cells* **37**, 754-765, doi:10.1002/stem.2993 (2019).

104 Diederichs, S. & Tuan, R. S. Functional comparison of human-induced pluripotent stem cell-derived mesenchymal cells and bone marrow-derived mesenchymal stromal cells from the same donor. *Stem Cells and Development* **23**, 1594-1610, doi:10.1089/scd.2013.0477 (2014).

105 Liu, J. & Farmer, S. R. Regulating the balance between peroxisome proliferator-activated receptor gamma and beta-catenin signaling during adipogenesis. A glycogen synthase kinase 3beta phosphorylation-defective mutant of beta-catenin inhibits expression of a subset of adipogenic genes. *The Journal of Biological Chemistry* **279**, 45020-45027, doi:10.1074/jbc.M407050200 (2004).

106 Marvulli, D., Volpin, D. & Bressan, G. M. Spatial and temporal changes of type VI collagen expression during mouse development. *Developmental Dynamics : an Official Publication of the American Association of Anatomists* **206**, 447-454, doi:10.1002/(sici)1097-0177(199608)206:4<447::aid-aja10>3.0.co;2-u (1996).

107 Sugrue, S. P. *et al.* Immunoidentification of type XII collagen in embryonic tissues. *The Journal of Cell Biology* **109**, 939-945, doi:10.1083/jcb.109.2.939 (1989).

108 McNeill, E. P. *et al.* Three-dimensional in vitro modeling of malignant bone disease recapitulates experimentally accessible mechanisms of osteoinhibition. *Cell Death & Disease* **9**, 1161, doi:10.1038/s41419-018-1203-8 (2018).

109 Murphy, M. P., Quarto, N., Longaker, M. T. & Wan, D. C. (*) Calvarial Defects: Cell-Based Reconstructive Strategies in the Murine Model. *Tissue Engineering. Part C, Methods* **23**, 971-981, doi:10.1089/ten.TEC.2017.0230 (2017).

110 Zara, J. N. *et al.* High doses of bone morphogenetic protein 2 induce structurally abnormal bone and inflammation in vivo. *Tissue Eng Part A* **17**, 1389-1399, doi:10.1089/ten.TEA.2010.0555 (2011).

111 Jeon, O. H. *et al.* Human iPSC-derived osteoblasts and osteoclasts together promote bone regeneration in 3D biomaterials. *Scientific Reports* **6**, 26761, doi:10.1038/srep26761 (2016).

112 Macedo, F. *et al.* Bone Metastases: An Overview. *Oncol Rev* **11**, 321-321, doi:10.4081/oncol.2017.321 (2017).

113 Roodman, G. D. Mechanisms of bone metastasis. *The New England Journal of Medicine* **350**, 1655-1664, doi:10.1056/NEJMra030831 (2004).

114 Lipton, A. *et al.* Skeletal-related events and clinical outcomes in patients with bone metastases and normal levels of osteolysis: exploratory analyses. *Clinical Oncology (Royal College of Radiologists (Great Britain))* **25**, 217-226, doi:10.1016/j.clon.2012.11.004 (2013).

115 Gunn, W. G. *et al.* A crosstalk between myeloma cells and marrow stromal cells stimulates production of DKK1 and interleukin-6: a potential role in the development of lytic bone disease and tumor progression in multiple myeloma. *Stem Cells* **24**, 986-991, doi:10.1634/stemcells.2005-0220 (2006).

116 Voorzanger-Rousselot, N. *et al.* Increased Dickkopf-1 expression in breast cancer bone metastases. *British Journal of Cancer* **97**, 964-970, doi:10.1038/sj.bjc.6603959 (2007).

117 Tian, E. *et al.* The role of the Wnt-signaling antagonist DKK1 in the development of osteolytic lesions in multiple myeloma. *The New England Journal of Medicine* **349**, 2483-2494, doi:10.1056/NEJMoa030847 (2003).

118 Lee, N. *et al.* A potential role for Dkk-1 in the pathogenesis of osteosarcoma predicts novel diagnostic and treatment strategies. *British Journal of Cancer* **97**, 1552-1559, doi:10.1038/sj.bjc.6604069 (2007).

119 Mao, B. *et al.* Kremen proteins are Dickkopf receptors that regulate Wnt/β-catenin signalling. *Nature* **417**, 664-667, doi:10.1038/nature756 (2002).

120 Baron, R. & Kneissel, M. WNT signaling in bone homeostasis and disease: from human mutations to treatments. *Nature Medicine* **19**, 179-192, doi:10.1038/nm.3074 (2013).

121 Gregory, C. A. More progress defining the crosstalk between multiple myeloma and mesenchymal stem cells of the bone marrow. *Leukemia & Lymphoma* **48**, 1896-1897, doi:10.1080/10428190701625115 (2007).

122 Gregory, C. Advances in myeloma therapy: breaking the cycle. *Blood* **109**, 1798-1798, doi:10.1182/blood-2006-12-062067 (2007).

123 Hoffman, R. M. The three-dimensional question: can clinically relevant tumor drug resistance be measured in vitro? *Cancer Metastasis Reviews* **13**, 169-173 (1994).

124 Kunz-Schughart, L. A., Kreutz, M. & Knuechel, R. Multicellular spheroids: a three-dimensional in vitro culture system to study tumour biology. *International Journal of Experimental Pathology* **79**, 1-23, doi:10.1046/j.1365-2613.1998.00051.x (1998).

125 Becker, J. L. & Souza, G. R. Using space-based investigations to inform cancer research on Earth. *Nature Reviews. Cancer* **13**, 315-327, doi:10.1038/nrc3507 (2013).

126 Margolis, L. *et al.* Long term organ culture of human prostate tissue in a NASA-designed rotating wall bioreactor. *The Journal of Urology* **161**, 290-297 (1999).

127 Barzegari, A. & Saei, A. A. An update to space biomedical research: tissue engineering in microgravity bioreactors. *Bioimpacts* **2**, 23-32, doi:10.5681/bi.2012.003 (2012).

128 Hammond, T. G. & Hammond, J. M. Optimized suspension culture: the rotating-wall vessel. *American Journal of Physiology. Renal Physiology* **281**, F12-25, doi:10.1152/ajprenal.2001.281.1.F12 (2001).

129 Krause, U., Ryan, D. M., Clough, B. H. & Gregory, C. A. An unexpected role for a Wnt-inhibitor: Dickkopf-1 triggers a novel cancer survival mechanism through modulation of aldehyde-dehydrogenase-1 activity. *Cell Death & Disease* **5**, e1093, doi:10.1038/cddis.2014.67 (2014).

130 Bilir, B., Kucuk, O. & Moreno, C. S. Wnt signaling blockage inhibits cell proliferation and migration, and induces apoptosis in triple-negative breast cancer cells. *Journal of Translational Medicine* **11**, 280, doi:10.1186/1479-5876-11-280 (2013).

131 Pattyn, F., Speleman, F., De Paepe, A. & Vandesompele, J. RTPrimerDB: the real-time PCR primer and probe database. *Nucleic Acids Research* **31**, 122-123, doi:10.1093/nar/gkg011 (2003).

132 Joliat, M. J., Umeda, S., Lyons, B. L., Lynes, M. A. & Shultz, L. D. Establishment and characterization of a new osteogenic cell line (MOS-J) from a spontaneous C57BL/6J mouse osteosarcoma. *In vivo (Athens, Greece)* **16**, 223-228 (2002).

133 Ontiveros, C. & McCabe, L. R. Simulated microgravity suppresses osteoblast phenotype, Runx2 levels and AP-1 transactivation. *J Cell Biochem* **88**, 427-437, doi:10.1002/jcb.10410 (2003).

134 Botchwey, E. A., Pollack, S. R., Levine, E. M. & Laurencin, C. T. Bone tissue engineering in a rotating bioreactor using a microcarrier matrix system. *J Biomed Mater Res* **55**, 242-253 (2001).

135 Granet, C., Laroche, N., Vico, L., Alexandre, C. & Lafage-Proust, M. H. Rotating-wall vessels, promising bioreactors for osteoblastic cell culture: comparison with other 3D conditions. *Medical & Biological Engineering & Computing* **36**, 513-519 (1998).

136 Jho, E. H. *et al.* Wnt/beta-catenin/Tcf signaling induces the transcription of Axin2, a negative regulator of the signaling pathway. *Molecular and Cellular Biology* **22**, 1172-1183, doi:10.1128/mcb.22.4.1172-1183.2002 (2002).

137 Huang da, W., Sherman, B. T. & Lempicki, R. A. Bioinformatics enrichment tools: paths toward the comprehensive functional analysis of large gene lists. *Nucleic Acids Research* **37**, 1-13, doi:10.1093/nar/gkn923 (2009).

138 Huang da, W., Sherman, B. T. & Lempicki, R. A. Systematic and integrative analysis of large gene lists using DAVID bioinformatics resources. *Nat Protoc* **4**, 44-57, doi:10.1038/nprot.2008.211 (2009).

139 Unsworth, B. R. & Lelkes, P. I. Growing tissues in microgravity. *Nature Medicine* **4**, 901-907 (1998).

140 Borden, M., Attawia, M., Khan, Y. & Laurencin, C. T. Tissue engineered microsphere-based matrices for bone repair: design and evaluation. *Biomaterials* **23**, 551-559 (2002).

141 Wang, H., Leeuwenburgh, S. C., Li, Y. & Jansen, J. A. The use of micro- and nanospheres as functional components for bone tissue regeneration. *Tissue Engineering. Part B, Reviews* **18**, 24-39, doi:10.1089/ten.TEB.2011.0184 (2012).

142 Lal, P. & Sun, W. Computer modeling approach for microsphere-packed bone scaffold. *Computer-Aided Design* **36**, 487-497, doi:https://doi.org/10.1016/S0010-4485(03)00134-9 (2004).

143 Gregory, C. A. and Prockop, D. J. (2007). Fundamentals of Culture and Characterization of Mesenchymal Stem/Progenitor Cells (MSCs) from Bone Marrow Stroma. In Culture of Human Stem Cells (eds R. I. Freshney, G. N. Stacey and J. M. Auerbach). doi:10.1002/9780470167526.ch9

144 Sheyn, D., Pelled, G., Netanely, D., Domany, E. & Gazit, D. The effect of simulated microgravity on human mesenchymal stem cells cultured in an osteogenic differentiation system: a bioinformatics study. *Tissue Eng Part A* **16**, 3403-3412, doi:10.1089/ten.tea.2009.0834 (2010).

145 Frith, J. E., Thomson, B. & Genever, P. G. Dynamic three-dimensional culture methods enhance mesenchymal stem cell properties and increase therapeutic potential. *Tissue Engineering. Part C, Methods* **16**, 735-749, doi:10.1089/ten.TEC.2009.0432 (2010).

146 Zayzafoon, M., Gathings, W. E. & McDonald, J. M. Modeled microgravity inhibits osteogenic differentiation of human mesenchymal stem cells and increases adipogenesis. *Endocrinology* **145**, 2421-2432, doi:10.1210/en.2003-1156 (2004).

147 Carmeliet, G. & Bouillon, R. The effect of microgravity on morphology and gene expression of osteoblasts in vitro. *FASEB Journal : Official Publication of the Federation of American Societies for Experimental Biology* **13 Suppl**, S129-134, doi:10.1096/fasebj.13.9001.s129 (1999).

148 Carmeliet, G., Nys, G. & Bouillon, R. Microgravity reduces the differentiation of human osteoblastic MG-63 cells. *J Bone Miner Res* **12**, 786-794, doi:10.1359/jbmr.1997.12.5.786 (1997).

149 Carmeliet, G., Nys, G., Stockmans, I. & Bouillon, R. Gene expression related to the differentiation of osteoblastic cells is altered by microgravity. *Bone* **22**, 139s-143s (1998).

150 Leber, J. *et al.* Microcarrier choice and bead-to-bead transfer for human mesenchymal stem cells in serum-containing and chemically defined media. *Process Biochemistry* **59**, 255-265, doi:https://doi.org/10.1016/j.procbio.2017.03.017 (2017).

151 Nakashima, K. *et al.* The novel zinc finger-containing transcription factor osterix is required for osteoblast differentiation and bone formation. *Cell* **108**, 17-29 (2002).

152 Marom, R., Shur, I., Solomon, R. & Benayahu, D. Characterization of adhesion and differentiation markers of osteogenic marrow stromal cells. *Journal of Cellular Physiology* **202**, 41-48, doi:10.1002/jcp.20109 (2005).

153 Fulciniti, M. *et al.* Anti-DKK1 mAb (BHQ880) as a potential therapeutic agent for multiple myeloma. *Blood* **114**, 371-379, doi:10.1182/blood-2008-11-191577 (2009).

154 Gunn, W. G., Krause, U., Lee, N. & Gregory, C. A. Pharmaceutical inhibition of glycogen synthetase kinase-3beta reduces multiple myeloma-induced bone disease in a novel murine plasmacytoma xenograft model. *Blood* **117**, 1641-1651, doi:10.1182/blood-2010-09-308171 (2011).

155 Prockop, D. J. & Olson, S. D. Clinical trials with adult stem/progenitor cells for tissue repair: let's not overlook some essential precautions. *Blood* **109**, 3147-3151, doi:10.1182/blood-2006-03-013433 (2007).

156 Marinkovic, M. *et al.* One size does not fit all: developing a cell-specific niche for in vitro study of cell behavior. *Matrix Biology : Journal of the International Society for Matrix Biology* **52-54**, 426-441, doi:10.1016/j.matbio.2016.01.004 (2016).

157 Chaput, C. D. *et al.* How stem cell composition in bone marrow aspirate relates to clinical outcomes when used for cervical spine fusion. *PLoS One* **13**, e0203714, doi:10.1371/journal.pone.0203714 (2018).

158 Chen, X., Xu, H., Wan, C., McCaigue, M. & Li, G. Bioreactor Expansion of Human Adult Bone Marrow-Derived Mesenchymal Stem Cells. *Stem Cells* **24**, 2052-2059, doi:10.1634/stemcells.2005-0591 (2006).